

NASA CONTRACTOR REPORT 172276

NASA-CR-172276
19840009979

LUNEBURG LENS AND OPTICAL
MATRIX ALGEBRA RESEARCH

V. E. WOOD, J. R. BUSCH, C. M. VERBER
AND H. J. CAULFIELD

BATTELLE COLUMBUS LABORATORIES
COLUMBUS, OH 43201

CONTRACT NAS 1-16652

FEBRUARY 10, 1984

LIBRARY COPY

FEB 23 1984

LANGLEY RESEARCH CENTER
LIBRARY, NASA
HAMPTON, VIRGINIA



National Aeronautics and
Space Administration

Langley Research Center
Hampton, Virginia 23665

NASA CONTRACTOR REPORT 172276

LUNEBURG LENS AND OPTICAL
MATRIX ALGEBRA RESEARCH

V. E. WOOD, J. R. BUSCH, C. M. VERBER
AND H. J. CAULFIELD

BATTELLE COLUMBUS LABORATORIES
COLUMBUS, OH 43201

CONTRACT NAS 1-16652

FEBRUARY 10, 1984



National Aeronautics and
Space Administration

Langley Research Center
Hampton, Virginia 23665

N84-18047#

TABLE OF CONTENTS

	<u>Page</u>
I. INTRODUCTION.	1
II. INTEGRATED OPTIC CIRCUITS FOR MATRIX COMPUTATION.	2
1. Introduction	2
2. Elementary Arithmetic Operations Using Planar IOCS	5
Subtraction and Vector Subtraction.	7
Multiplication and Vector Multiplication.	7
3. Matrix-Vector Multiplication	10
Systolic Array Architecture	12
Fully Parallel Architecture	18
4. Matrix-Matrix Multiplication	23
5. Solution of System Control Equations	29
The Multiplication of Large Matrices.	31
Matrix Inversion.	33
III. LUNEBURG LENSES.	37
6. Introduction	37
7. Waveguide and Substrate.	38
8. As ₂ S ₃ Film Deposition.	41
9. Lens Design.	52
10. Mask Design.	53
11. Ray Tracing.	58
12. Lens Fabrication and Testing	68
13. Chemical Analyses.	74
14. Discussion and Conclusions	77
IV. REFERENCES	79
V. APPENDICES	82
Appendix A - The Nonlinearity Problem.	82
Appendix B - Systolic Triple Matrix Product Calculations on Partitioned Matrices.	94
Appendix C - Numerical Accuracy.	101
Appendix D - Publications.	106

LIST OF FIGURES

	<u>Page</u>
Figure 1. Interdigital electrode pattern used to generate an electrooptic grating.	4
Figure 2. Diffraction efficiency versus voltage for electrooptic grating with $\Lambda = 13.3 \mu\text{m}$, $d = 2.8 \text{ mm}$ deposited on a $\text{LiNbO}_3\text{:Ti}$ waveguide.	6
Figure 3. An extended electrooptic structure for performing vector subtraction	8
Figure 4. A herringbone electrooptic structure for performing multiplication.	9
Figure 5. The herringbone structure extended to allow vector multiplication.	11
Figure 6. A suggested optical implementation of a systolic matrix vector multiplier.	13
Figure 7. The engagement architecture for vector-matrix multiplication indicating the data flow and the product accumulation	15
Figure 8. A suggested integrated optical circuit for performing vector matrix multiplication using the engagement architecture.	16
Figure 9. Digital drive circuitry for exercising the engagement processor	17
Figure 10. Schematic of the fully parallel method of performing matrix-vector multiplication.	19
Figure 11. IOC for direct vector matrix multiplication	21
Figure 12. Systolic array architecture for matrix-matrix multiplication showing the flow of data through the computational elements.	24
Figure 13. IOC for matrix multiplication based upon systolic array concept	25
Figure 14. A modified IOC for matrix-matrix multiplication by the engagement algorithm.	27
Figure 15. Using 3 2×2 processors to compute the products required for four of the terms in a 6×6 product.	28
Figure 16. A flowchart for iterative matrix inversion.	36

LIST OF FIGURES (Continued)

	<u>Page</u>
Figure 17. Prism-coupling method for measuring refractive indices of LiNbO_3 plates.	40
Figure 18. Experimental arrangement for making arsenic trisulfide Luneburg lenses by evaporation	42
Figure 19. Experimental arrangement for making arsenic trisulfide Luneburg lenses by rf sputtering	44
Figure 20. Twyman-Green interferogram of arsenic trisulfide Luneburg lens 1 cm in diameter.	47
Figure 21. Apparent refractive index of As_2S_3 film prism as function of time of exposure to 1.1 mW/cm^2 of ultraviolet light, as determined by deflection of 3 different modes supported in prism region	51
Figure 22. Design mode-index profile for f/2.1 Luneburg lens of 10 mm input aperture, designed to focus TM_0 mode of $\text{LiNbO}_3\text{:Ti}$ waveguide.	54
Figure 23. Design lens profile (dashed line) and approximation (solid line) with mask arrangement described in text for example f/2.1 Luneburg lens.	55
Figure 24. Measured (circles) and calculated (x's) focal lengths for Luneburg lenses of different thicknesses made with the same mask arrangement.	60
Figure 25. Ray trace through lens with example design thickness profile shown in Figure 23.	61
Figure 26. Focal-plane diffraction pattern for lens ray-traced in Figure 25. The diffraction pattern for a Luneburg lens is given approximately by a section parallel to a coordinate axis.	63
Figure 27. Ray trace through a lens similar to that in Figure 25, but with reduced film refractive index.	64
Figure 28. Focal plane diffraction pattern for lens ray-traced in Figure 27.	65
Figure 29. Ray trace through a lens with profile, shown in Figure 23, attainable with simple mask arrangement	66
Figure 30. Focal plane diffraction pattern for lens ray-traced in Figure 29.	67
Figure 31. Experimental arrangement for observation of Luneburg lens focal plane characteristics.	69
Figure 32. Diode-array scan of focal plane of as-prepared evaporated lens	71
Figure 33. Diode-array scan of focal plane of evaporated lens exposed to ultraviolet light	72

I. INTRODUCTION

The long-term goal of this work is to develop a class of hybrid integrated-optical processors which will be capable of high-speed matrix computations. It is envisioned that the ultimate system will consist of an array of many integrated optical circuits (IOCs) of several different types which are interconnected in a programmable fashion to allow a variety of computational tasks to be carried out.

The potential advantages of the hybrid integrated-optical processor are high computation speed, low power consumption and mechanical integrity, all of which are advantageous for the aerospace environment. Two of the key technical problems are the architectural strategies for computational IOCs and their interconnection, and the integrated optical lenses which are required for compact IOC packaging. These topics are addressed in separate chapters of this report.

The chapter on Integrated Optic Circuits for Matrix Computation stresses planar, as opposed to channelized, integrated optical circuits (IOCs) as the basis for computational devices. Both fully-parallel and systolic architectures are considered and the tradeoffs between the two device types are discussed. It is then pointed out that the Kalman filter approach is a most important computational method for many NASA problems. This approach to deriving a best-fit estimate for the state vector describing a large system will lead to matrix sizes which are beyond the predicted capacities of planar IOCs. It is shown that this problem can be overcome by matrix partitioning, and several architectures for accomplishing this are described.

The Luneburg lens work has involved development of lens design techniques, design of mask arrangements for producing lenses of desired shape, investigation of optical and chemical properties of arsenic trisulfide films, deposition of lenses both by thermal evaporation and by rf sputtering, optical testing of these lenses, modification of lens properties through ultraviolet irradiation, and comparison of measured lens properties with those expected from ray-trace analyses. Lenses with apertures up to 1 cm and design speeds down to $f/2$ at this aperture were tried. The better evaporated lenses had focal spot sizes, at reduced aperture, no more than twice the limit set by diffraction effects. Initial sputtered lenses promised to be of comparable quality; lenses made after the sputtering target had been in operation for some time, though, tended to absorb light excessively at the design wavelength, 633 nm. This effect appears to be related to a change in the composition of the films. When a thoroughly reliable deposition and treatment process for chalcogenide lens materials is developed, straightforward design and testing improvements should permit fabrication of Luneburg lenses suitable for many beam-forming and signal-processing requirements.

Although this report has two relatively independent major sections, the figure, equation, and reference numbers are consecutive. The subsections and pages are also numbered consecutively throughout; all the appendices are placed at the end.

II. INTEGRATED OPTIC CIRCUITS FOR MATRIX COMPUTATION

1. INTRODUCTION

The goal of this effort was to evaluate integrated optic architectures required to perform matrix algebra functions such as addition, subtraction, multiplication and inversion and to combine these functions to obtain solutions to matrix algebra equations. It was desired that particular attention be paid to optical implementation of systolic array architectures during these evaluations.

In carrying out the program the operations of matrix-vector and matrix-matrix multiplication were emphasized over all others because of their importance in a large number of application areas and because these are operations which consume a large amount of time and hardware when performed electronically. The systolic architectures were stressed, but some attention was paid to looking at the implications of fully parallel methods, especially for the matrix-vector multiplication operation.

From a more systems-oriented viewpoint, this study also touched upon some NASA applications for high-speed matrix processors, identified the Kalman filter as having a large number of important applications, and showed that by using standard matrix decomposition techniques, it is possible to use arrays of optical processors of limited size to carry out very large computations.

In this section we deal both with the hardware and systems aspects of optical matrix multiplication. The hardware discussion begins with a description of the basic integrated optic components, then progresses to integrated optic architectures for matrix multiplication, and ends with methods for assembling a number of basic multipliers to perform operations on large matrices. The remainder of the section is devoted to a discussion of some applications of the matrix-multiplication operation which should be of interest to NASA.

Many of the basic functions which are required to construct integrated-optic computational devices can be implemented either in a planar or a channel waveguide geometry. In the work which has been under way at Battelle for the past few years, we have selected the planar geometry for a number of reasons. Some of these are: ease of fabrication, geometric

versatility, and the elimination of some of the complicating interference effects which arise when single-mode channel waveguides are merged.

Much of the relevant work performed in our laboratories has involved the use of an interdigital electrode pattern, such as shown in Figure 1, which when deposited on a buffer layer on the surface of an electrooptic waveguide can be used to modulate the intensity of, or to change the direction of, a planar guided wave. The buffer layer serves to isolate the electrodes from the waveguide so that the guided wave is affected only by the electrically induced periodic index-of-refraction variation and not by the presence of the metallization pattern.

The tangential component of the electric field in the waveguide is the only field effective in altering the refractive index for the usual arrangement: TE-mode light propagating in the x direction in a Y-cut crystal of LiNbO₃. An expression describing this field has been derived by Engan.⁽¹⁾ The fundamental component is given by

$$E_z = (0.847) \left(\frac{V_0}{g} \right) \cos \frac{\pi z}{2g} , \quad (1)$$

where g is the electrode gap width, and z is the distance from the gap center. In the Bragg regime only this component is effective. In the electrooptic waveguide this field results in an index-of-refraction modulation

$$\Delta n = - \frac{1}{2} n_{\text{eff}}^3 r E. \quad (2)$$

The index of refraction n_{eff} is the effective index of the guided mode, and r is the appropriate electrooptic coefficient. Since the electric field and the index modulation fall exponentially, it is desirable to use a waveguide which confines the light closely to the waveguide surface. On a LiNbO₃ substrate, a Ti-indiffused guide is therefore preferable to an out-diffused guide.

If we ignore the falloff of the field in the y direction, we can treat the periodic index variation as a simple thick Bragg grating, the Bragg angle θ_B being given by

$$\sin \theta_B = \lambda_0 / 2n_{\text{eff}} \Lambda \quad (3)$$

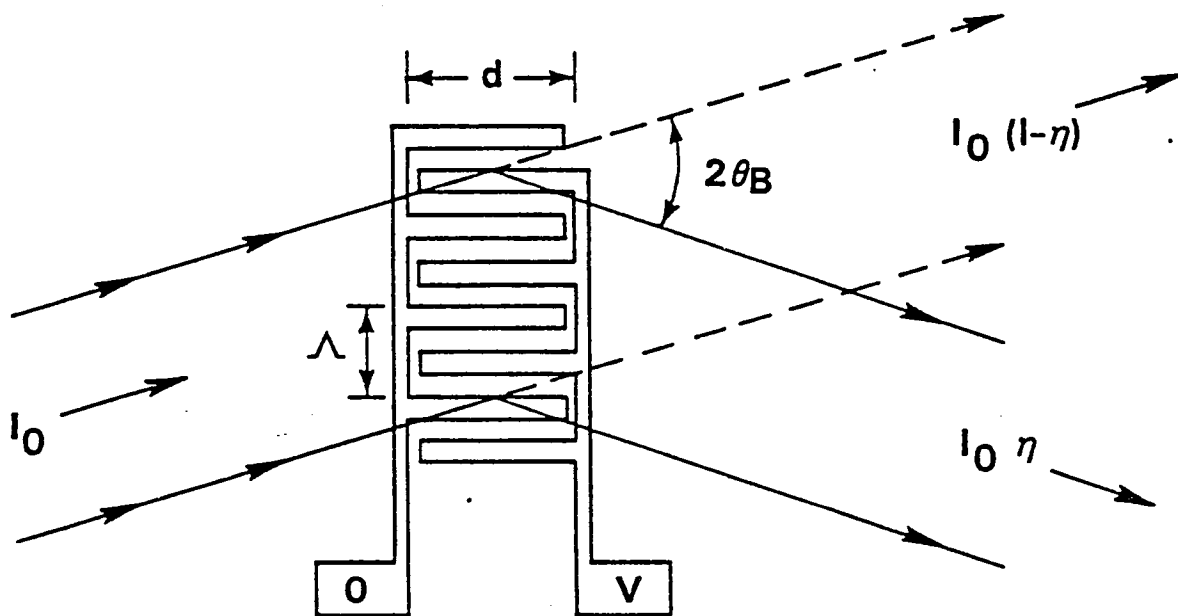


Figure 1. Interdigital electrode pattern used to generate an electrooptic grating.

and the diffraction efficiency by(2)

$$\eta = \sin^2 \frac{\pi \Delta n d}{\lambda_0 \cos \theta_B} \quad (4)$$

where Λ is the wavelength of the electrooptic grating, and λ_0 is the vacuum wavelength of the light.

In carrying out this work we have used electrooptic gratings with wavelength Λ , of both 13.33 μm and 8.41 μm . These have Bragg angles of 0.62° 0.98°, respectively for He-Ne laser light in the LiNbO₃ waveguides. The measured diffraction efficiency for one of these gratings is shown in Figure 2. As can be seen, the maximum efficiency is about 95% and the behavior of the diffraction efficiency as a function of the applied voltage is a good fit to the behavior predicted by Eq. (4). These electrode structures are easily fabricated by standard photolithographic techniques and have a low capacitance allowing high-speed operation.

2. ELEMENTARY ARITHMETIC OPERATIONS USING PLANAR IOCs

We describe here some modifications of the basic interdigital electrode structure which allow a number of elementary computational functions to be performed. It should be noted that all of the computational schemes which we discuss are intrinsically analog in nature and can therefore be expected to have an accuracy of about 1% (6 to 7 bits), as compared to 16 bits or more for digital systems. This apparent disadvantage must be viewed in light of the very high-speed operation, low power dissipation and ease of fabrication which is expected to characterize the IO devices. In addition there have been recent suggestions for architectures which have the potential for increasing the accuracy of optical devices to the 16-bit range and for incorporating floating-point operation. We have not yet attempted to work out all of the details involved in incorporating these improvements into a single IOC, but it is evident that there will be a significant increase in hardware complexity, not an unexpected tradeoff.

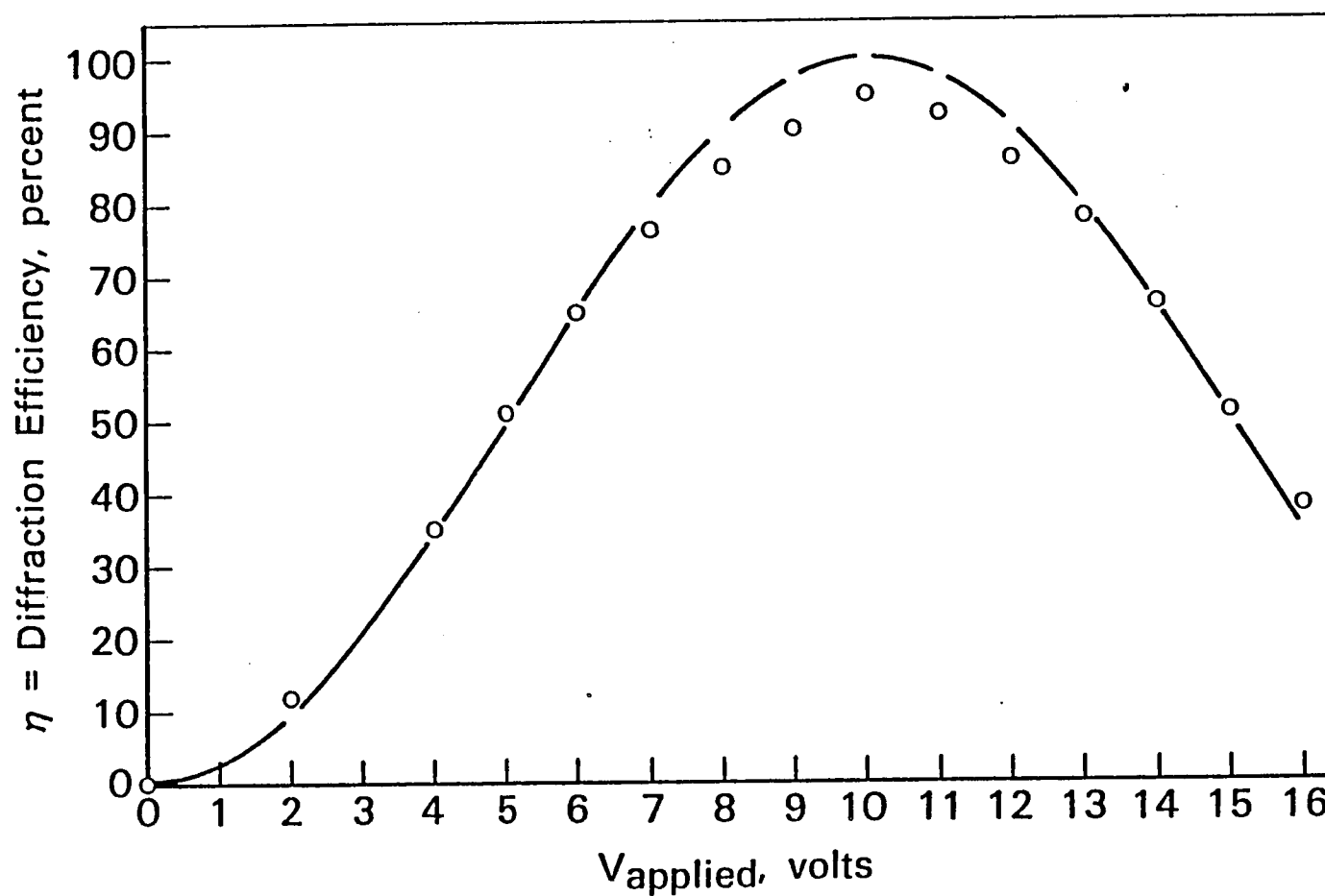


Figure 2. Diffraction efficiency versus voltage for electrooptic grating with $\Lambda = 13.3 \mu\text{m}$, $d = 2.8 \text{ mm}$ deposited on a $\text{LiNbO}_3\text{:Ti}$ waveguide. Solid line shows the calculated diffraction efficiency and the points are observed data.

Subtraction and Vector Subtraction

We can combine Equations 2 and 4 and rewrite them as

$$\eta = \sin^2[a(A-B)] \quad (5)$$

where a contains all of the geometric and material parameters and A and B are the voltages applied to the left and right electrodes, respectively. The intensity of the diffracted beam is now seen to be proportional to the difference of the two voltages. If the electrode structure is extended as shown in Figure 3 and a lens is added to collect the contributions of the individual segments of the structure then the optical energy at the detector is given by

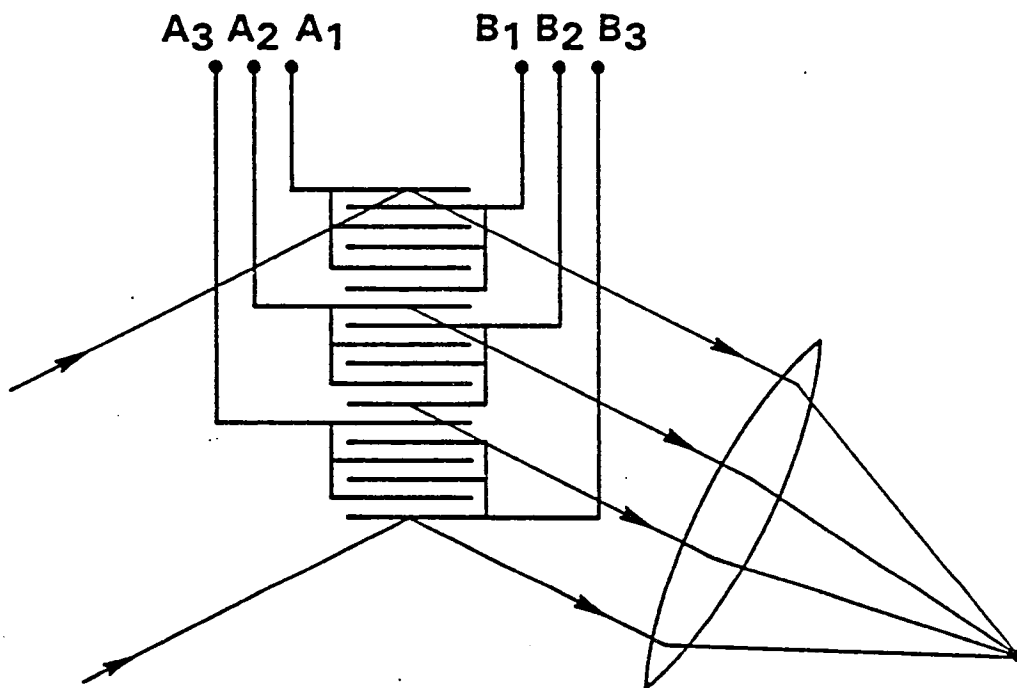
$$E = \sum_{i=1}^N \frac{E_0}{N} [\sin^2 a(A_i - B_i)]$$
$$\approx \frac{E_0}{N} a^2 \sum (A_i - B_i)^2. \quad (6)$$

It is evident that if A_i and B_i are the components of the N -dimensional vectors \vec{A} and \vec{B} , respectively, the structure shown in Figure 3 produces a quantity proportional to the vector difference $(\vec{A} - \vec{B})^2$. Of course, this is true only when all A_i and B_i satisfy the condition

$$a(A_i - B_i) \approx \sin[a(A_i - B_i)] \quad (7)$$

Multiplication and Vector Multiplication

In Figure 4 are shown two electrooptic grating electrodes arranged in a herringbone pattern with a grounded spine. The angles are such that light diffracted by the first grating is incident upon the second grating at its Bragg angle. Twice-diffracted light therefore has an intensity which is proportional to the product of the diffraction efficiencies of the two gratings. In general, this intensity is proportional to the product of two sine functions, a quantity which is proportional to the product AB of the two



$$I = \sum I_i = \sum a^2(A_i - B_i)^2$$

Figure 3. An extended electrooptic structure for performing vector subtraction.

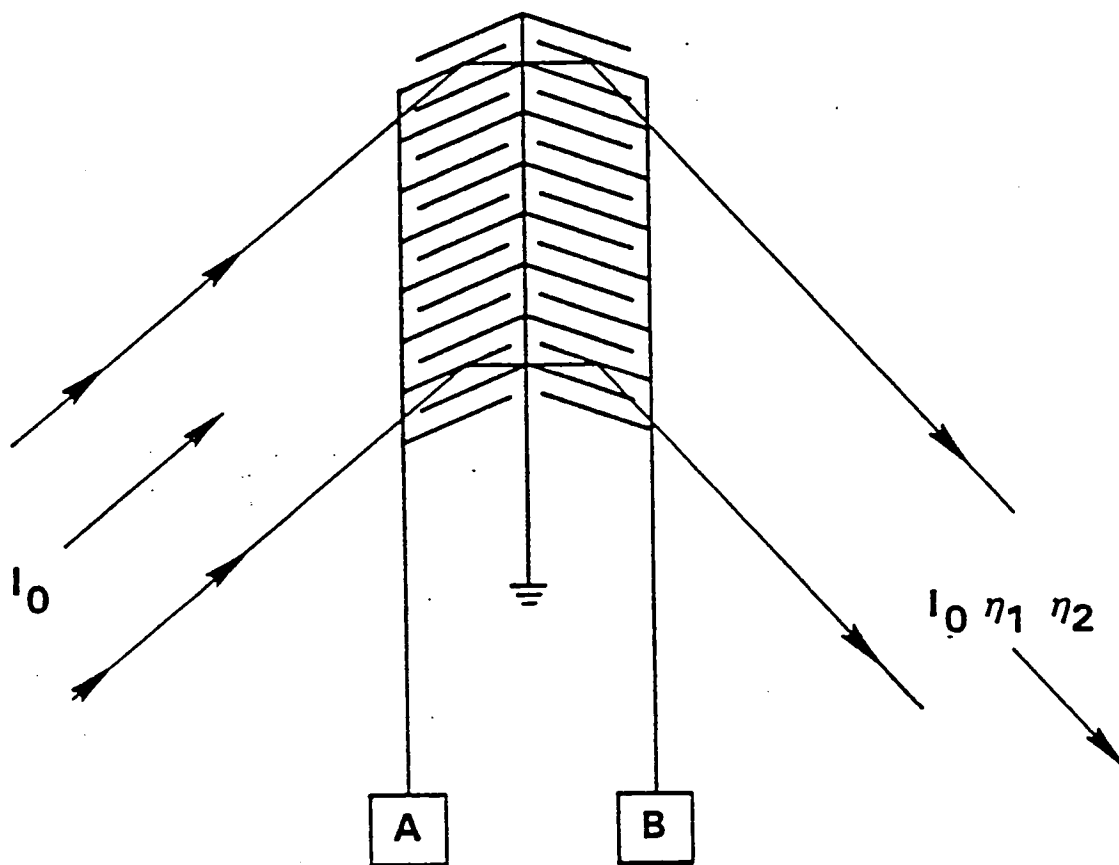


Figure 4. A herringbone electrooptic structure for performing multiplication. The geometry is such that light diffracted by the first grating enters the second grating at its Bragg angle so that it can subsequently be diffracted by the second grating. The output light intensity is therefore proportional to the product of the two diffraction efficiencies.

voltages only in the small signal approximation. Several methods for overcoming this nonlinearity are discussed in Appendix A. In the remainder of this section we shall proceed as if the linearization problem were handled by one or another of these methods.

The extension of the herringbone structure as shown in Figure 5 allows the generation of an optical signal whose power is proportional to the scalar product $\vec{A} \cdot \vec{B}$. It is this herringbone structure or variations of it which form the basis for all of the matrix-multiplication devices we discuss.

3. MATRIX-VECTOR MULTIPLICATION

We describe here two approaches to matrix-vector multiplication, both of which make use of the herringbone electrode arrangement previously described. The first is an adaptation of electronic systolic array architecture and the second is a fully parallel method. The comparison between the two approaches can provide the basis for some interesting tradeoff studies when all of the device parameters are available.

The problem to be addressed is illustrated for a 3×3 matrix in Eq. 8, where the vector components are x_i , $i = 1,2,3$, and the matrix elements are a_{ij} .

$$\begin{aligned} a_{11}x_1 + a_{12}x_2 + a_{13}x_3 &= y_1 \\ a_{12}x_1 + a_{22}x_2 + a_{23}x_3 &= y_2 \\ a_{13}x_1 + a_{23}x_2 + a_{33}x_3 &= y_3 \end{aligned} \tag{8}$$

The expansion of the multiplication

$$\underline{A} \vec{x} = \vec{y}, \tag{9}$$

is written out in detail to emphasize the facts that each component of x is used three (N) times during the calculation, and that the calculation itself is composed simply of the sum of products. Both addition and multiplication can be carried out quite naturally in an IOC, or, for that matter, in a bulk optical arrangement. The basic problem is to design an architecture which, most simply or efficiently, gets each of the x_i and a_{ij} to the proper position at the proper time. Both systolic and fully parallel methods of accomplishing this are discussed.

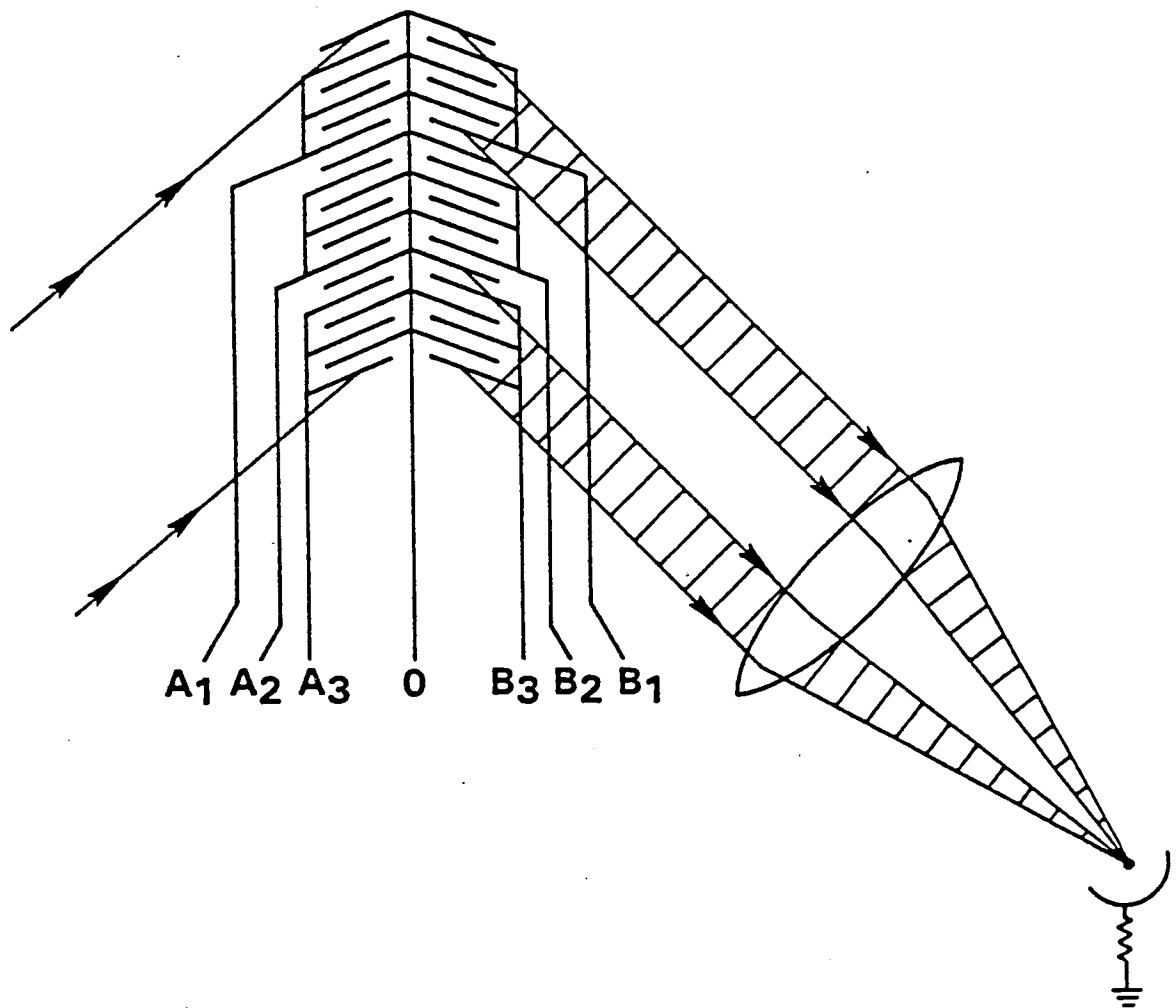


Figure 5. The herringbone structure extended to allow vector multiplication.

Systolic Array Architecture

The approach to computer design known as systolic array architecture was developed by Kung⁽³⁾ and others as a method of approaching the problem of VLSI computer design. The basic guidelines are:

- a. Each datum should be fetched from memory only once to avoid the "von Neumann bottleneck".
- b. Each chip should contain only a small number of different processor subunits, although these subunits may be repeated many times on each chip.
- c. Connections between subunits should be only to nearest neighbors to facilitate the rapid flow of data and to simplify fabrication.

The main disadvantage associated with the use of a systolic architecture in an optical processor is that the progression of data in discrete steps requires electronic timing circuitry which can place a severe constraint on the ultimate speed of the system. Aside from this problem, we would be hard pressed to compile a better set of design guidelines for integrated optical circuits than those listed above. The first guideline is certainly desirable since we do not yet have available an optically addressable memory for IOCs, although some recent work⁽⁴⁾ on surface holograms may be adaptable for this purpose. It is therefore essential that the recourse to memory be minimized since the act of fetching data from a digital store is much slower than the rate at which the IOC is capable of using that data. Second, at this stage in the development of IOC technology, we have only a small number of operational building blocks available to us. The second guideline is therefore compatible with IOC technology, if only by default. The third guideline is, perhaps, not as important for optical as for electronic systems since it is possible to have optical carriers intersect either in planar or in channel⁽⁵⁾ configurations without causing significant crosstalk. Complex interconnection schemes can therefore be implemented without requiring a multilayer structure. However, since the progress of the data through an optical processor is controlled by the speed of light in the device and not by a digital clock, it will be necessary to pay attention to path lengths in high-speed devices to assure that proper synchronism of the data flow is maintained.

The first optical matrix-vector multiplier based upon a systolic-type architecture was suggested by Caulfield, et al⁽⁶⁾ (Figure 6). This is an example of an optical implementation of Kung's systolic architecture as

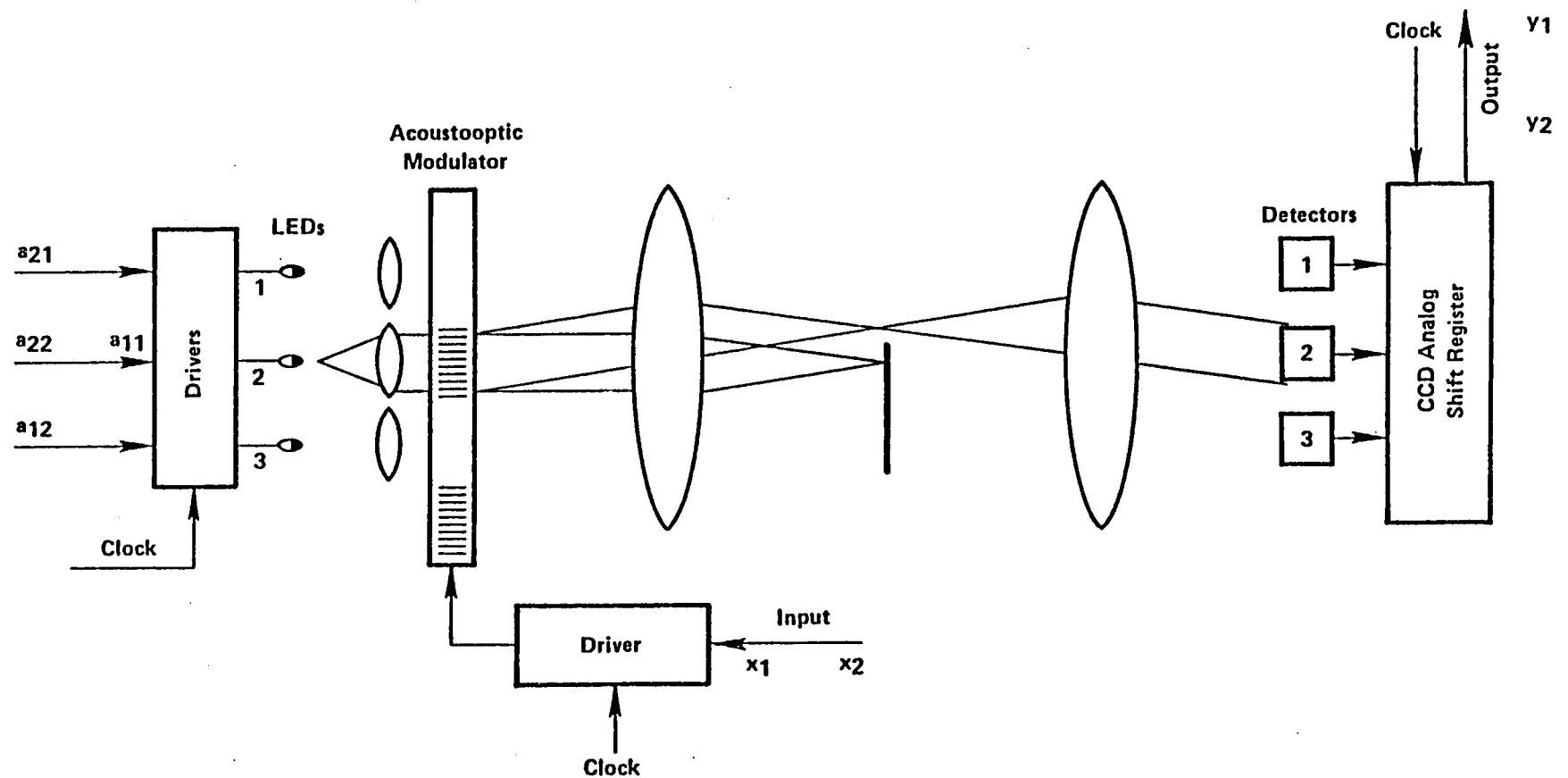


Figure 6. A suggested optical implementation of a systolic matrix vector multiplier (reference 6). Matrix values are introduced as LED intensities, vector values are introduced as surface acoustic wave amplitudes, and the products are summed in the CCD analog shift register which also tracks the position of the output.

modified by Tamura⁽⁷⁾ for optical implementation. The object of this so-called "engagement" architecture is to arrange for the data to flow through a series of cells which accept pairs of inputs and accumulate the sums of the products of the pairs. This data flow is illustrated schematically in Figure 7. In the implementation shown in Figure 6 the light sources are modulated in proportion to the matrix elements and the vector components are carried through the engagement region by a properly modulated acoustic wave. Since the data flow is essentially one-dimensional, this architecture can be implemented in either bulk- or integrated-optic form.

In an alternative scheme⁽⁸⁾ which was devised solely for IOC implementation, the engagement region consists of an extended herringbone electrode structure. The entire IOC, which is currently under construction, is shown schematically in Figure 8. It consists of the herringbone structure, shown in the figure as two integrated optical spatial light modulators (IOSLMs) tilted at an appropriate angle, collimating and imaging lenses along with a beam stop to prevent the undiffracted and singly diffracted light from reaching the detector array, and a suitable butt-coupled laser diode light source. The following figure (Figure 9) shows a schematic of the electronics required to exercise the device. It is assumed that both the matrix and vector values are stored in a digital memory. It is seen that a formidable array of shift registers and D/A converters are required to perform the introduction of electrical data.

There is an obvious tradeoff between the acoustic and electrooptic approaches. In the former, the vector components proceed naturally through the engagement region, carried by the acoustic wave. However, the data-rate is limited by the acoustic velocity and must, in fact, be synchronized with the rate determined by the acoustic velocity and the cell size. If we assume each datum is represented by at least a 100 μm -long SAW, and that the device is built in LNO, then the maximum data-rate is 35 MBit/sec. In the electro-optic multiplier, the data-rate is determined by an external electronic clock or shift register (which is also required to modulate the light sources in the acoustic device). Since the electrode capacitance is less than 20 pf/element, a data-rate of 500 MBit/sec should be possible, assuming a 50 ohm source impedance. The trade off is that to drive the electrooptic device additional external electronics are required. However, the speed advantage over SAW or pure electronic devices may make this a very favorable trade.

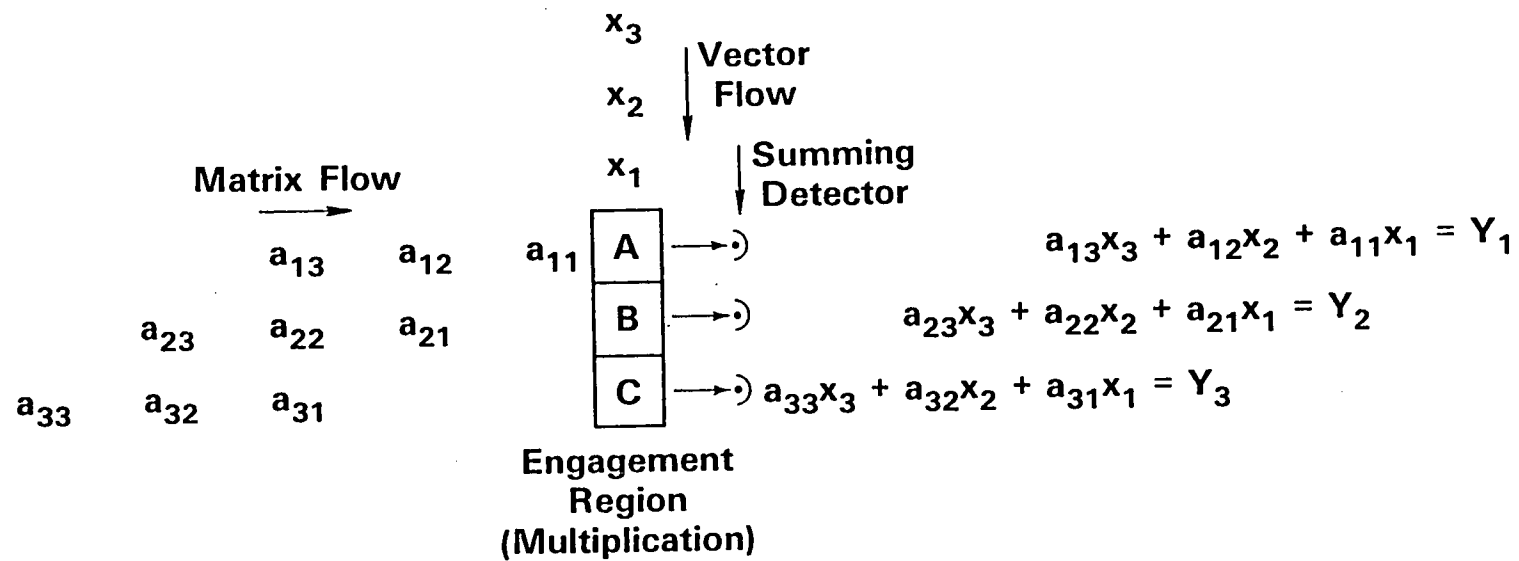


Figure 7. The engagement architecture for vector-matrix multiplication indicating the data flow and the product accumulation.

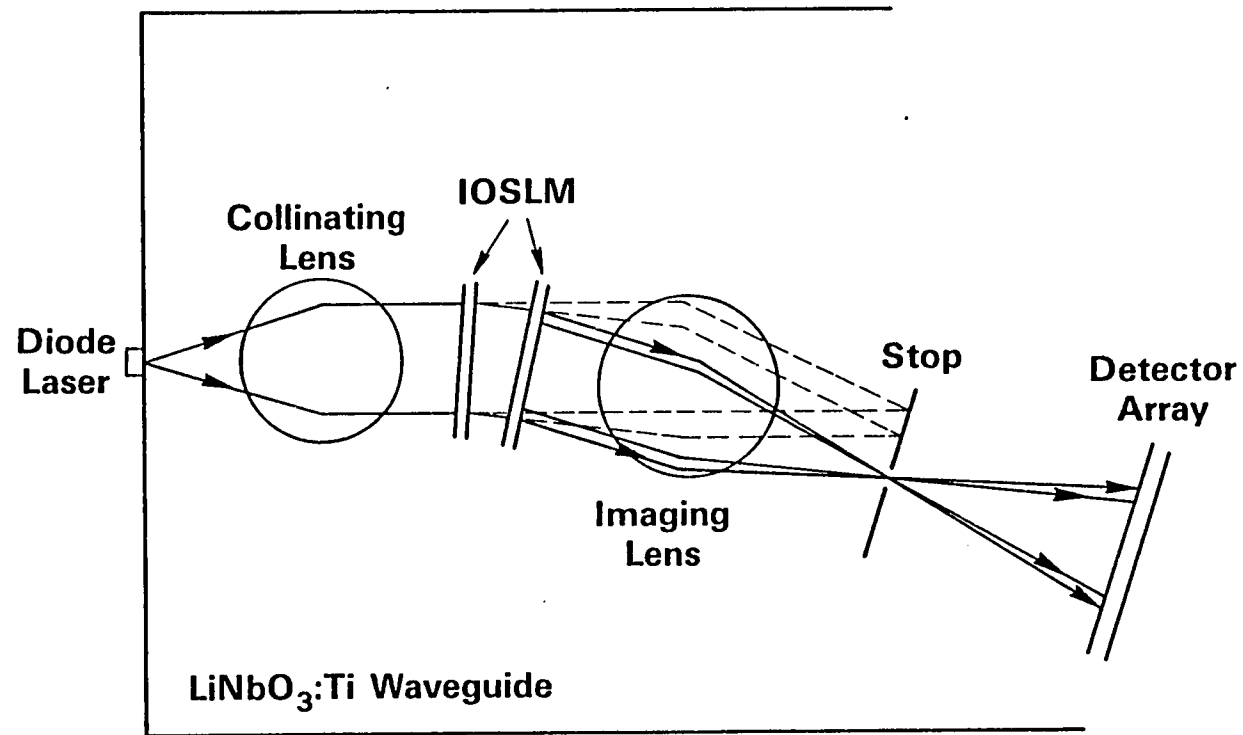


Figure 8. A suggested integrated optical circuit for performing vector matrix multiplication using the engagement architecture. The diode laser continually illuminates the interaction region which consists of two integrated optical spatial light modulators in the herringbone configuration. The lens images the interaction region on the detector array after the undiffracted and singly diffracted light has been removed from the beam.

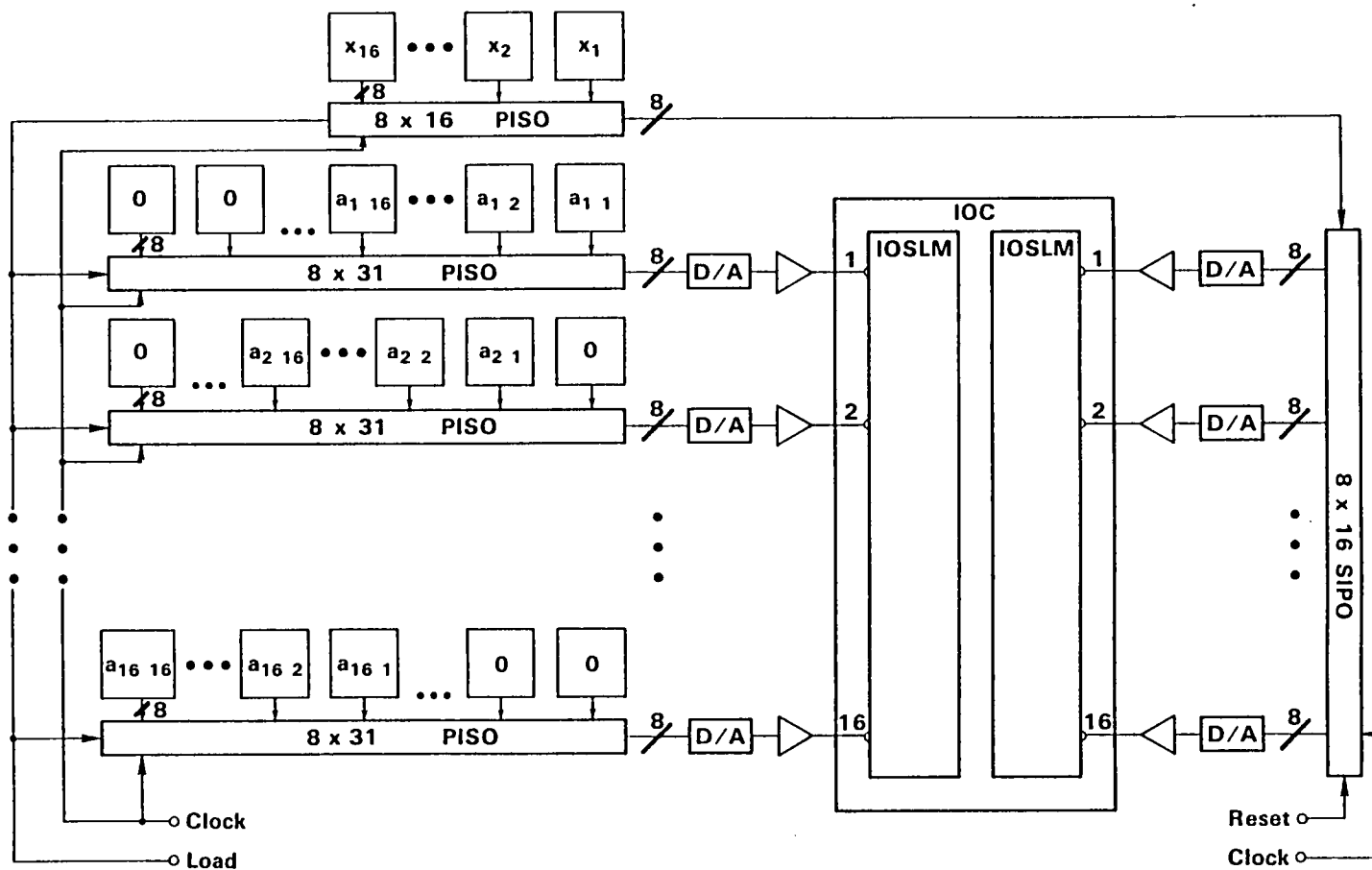


Figure 9. Digital drive circuitry for exercising the engagement processor. The parallel-in serial-out (PISO) shift registers receive the stored data from a digital memory and clock it through a D/A converter into the proper electrodes of the IOSLMs.

Fully Parallel Architecture

One of the traditional advantages of an optical approach to signal or data processing is the potential for utilizing a fully parallel architecture. In the case of matrix-vector multiplication, this means that all data are entered simultaneously and all multiplications and sums are carried out as the data are entered. The first suggestion for a fully parallel optical approach to matrix-vector multiplication was made by Goodman⁽⁹⁾ in 1978.

The Goodman approach provides an excellent basis for discussing some of the advantages and the problems associated with optical numerical processors. The earliest version of the Goodman matrix-vector multiplier is illustrated in Figure 10. Vector components are introduced as LED intensities x_1, x_2, \dots, x_N and the matrix components by a mask. The x_i are distributed over the appropriate a_{ji} mask locations by an anamorphic lens arrangement. The products are directed to the appropriate summing detectors by an orthogonal lens arrangement. The advantage of this configuration and, indeed, the basic rationale for the optical approach is its speed; answers appear as fast as the x_i are varied. The system latency is simply the time taken for light to traverse it, about 0.3 nsec for a 10 cm device. Goodman et al⁽¹⁰⁾ discusses several variations of this device. In one the anamorphic lenses are replaced by multimode slab waveguides and in another by fiber bundles.

All of these devices have the property of performing the matrix-vector multiplication in a fully parallel manner. They also have two obvious disadvantages. First, the device is not programmable and can therefore perform only one function. This "hard-wired" characteristic is common to all the numerical optical processors we will discuss. Second, they can handle only real, non-negative quantities, a point which can be addressed below, and third, there is no high-speed method for changing the matrix mask. This last disadvantage has been overcome in several devices suggested by other authors, but as could be expected, at the expense of additional complexity and, in case of serial input devices, at the expense of a great reduction in speed.

The Goodman architecture handles a two-dimensional data array (the mask) by means of a three-dimensional geometry, and therefore cannot be directly implemented in a planar integrated-optic format. It is however possible to design an IOC which can perform the fully parallel

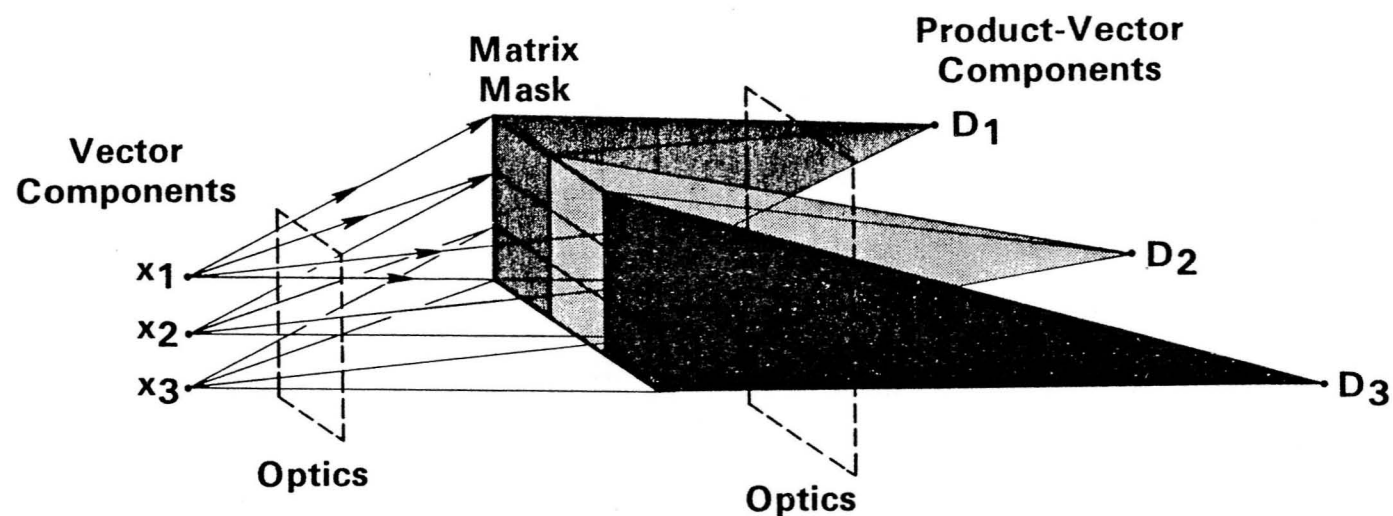


Figure 10. Schematic of the fully parallel method of performing matrix-vector multiplication. Vector components are introduced as optical intensities which are fanned-out horizontally across the rows of the matrix mask. Light from each column is then summed and focused on the detectors whose output is proportional to the components of the product vector.

operation. A schematic depicting such a device is shown in Figure 11. Once again, both matrix elements and vector components are introduced as voltages on electrooptic modulator segments. However, all voltages may be applied in parallel, the vector components being imposed upon a guided plane wave by an N-unit electrooptic IOSLM. These values are then distributed by fixed surface gratings so that they impinge, in parallel, upon the matrix-element modulators. As in the Goodman device, summation is performed with lenses and the device falls into the space-integrating category. Assuming a 3-cm path in LNO, the intrinsic processing time for such a device is 0.2 nsec. Of course, S/N and dynamic range requirements will certainly demand a larger integration time, but 10nsec/mult. should be realizable.

One of the most obvious of the trade-offs between the engagement and fully-parallel approach is speed vs. hardware complexity. The engagement processor requires a modulator N units wide. The direct processor requires a modulator N^2 units wide. The largest IOSLM constructed to date has thirty-two 100 μm -wide units -- a modulator 100 units wide is certainly possible, so a single engagement processor could handle a 100 x 100 matrix, and a direct processor a 10 x 10 matrix. The tradeoffs between the two approaches are summarized in Table 1.

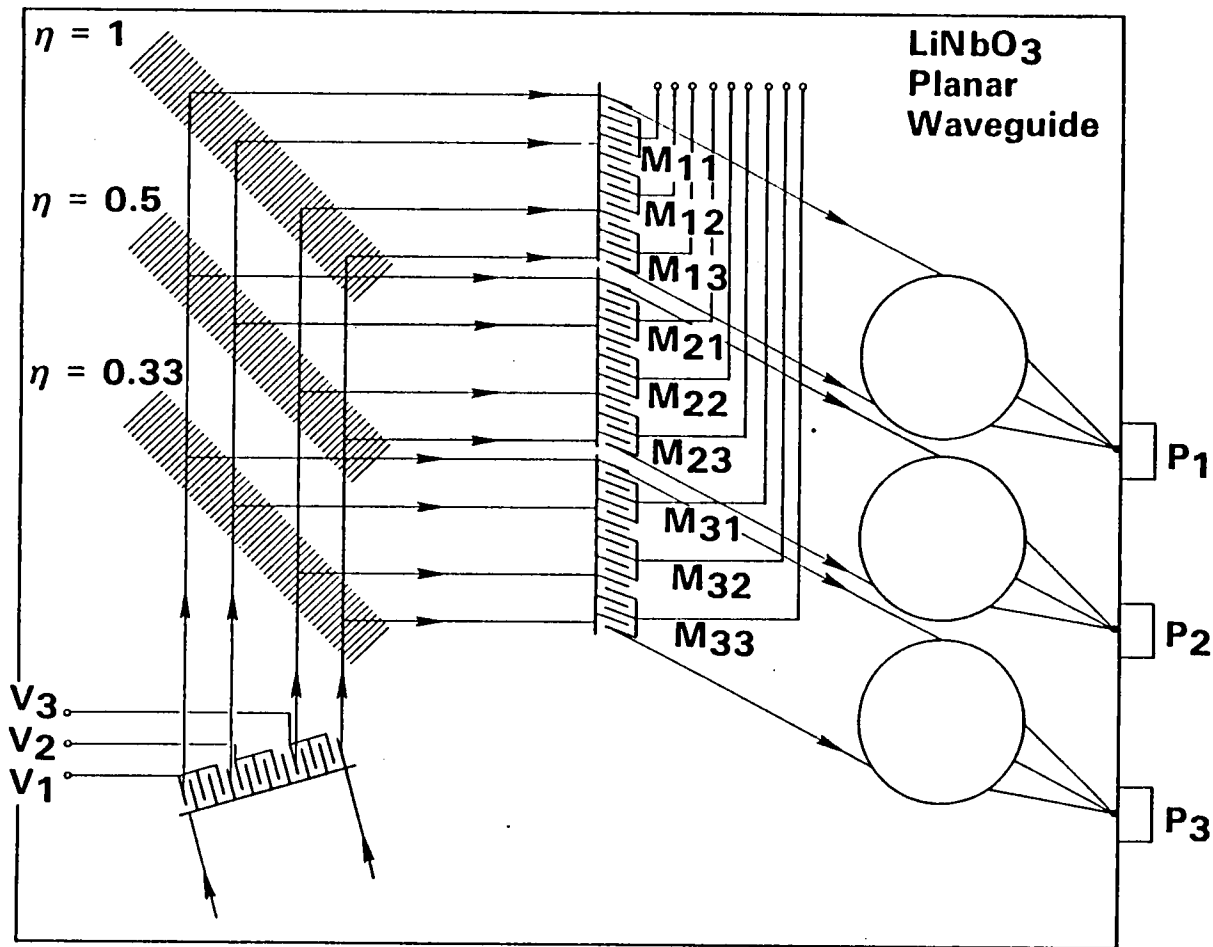


Figure 11. IOC for direct vector matrix multiplication. The IOSLM in the lower left is illuminated by a uniform guided wave. This guided wave is modulated in proportion to the vector components as shown. This information is then distributed via beam splitters to the modulators which carry the matrix information. As in Figure 10, the summation is performed optically and the resultant light is imaged on the appropriate photodetector.

TABLE I. COMPARISON OF DIRECT AND ENGAGEMENT ARCHITECTURES

	Engagement	Direct
Data Flow	Stepped	Continuous
Electronic Interface	Parallel set of sequential inputs	Fully parallel
Natural Device Geometry	Planar	3-D
Speed	Limited by electronic clock and/or shift register	Limited by detector SNR
Electronic Interface	Complex: $N+1$ shift registers, $2N$ D/A converters. All data moves at high speed.	Moderate: Only time-dependent values must change
IOC Size	Maximum IOSLM size: N	Maximum IOSLM size: N^2

4. MATRIX-MATRIX MULTIPLICATION

Matrix-vector multiplication can be described as an N^2 problem, since N^2 multiplications are required to produce the components of the product vector. In the process of obtaining the desired result, each vector component is used N times, and each matrix element is used once. The matrix-matrix multiplication problem is, on the other hand, an N^3 problem, the components of both matrices all being used N times in the computation. More specifically, the problem is to compute

$$\underline{\underline{C}} = \underline{\underline{A}} \cdot \underline{\underline{B}} \quad (10)$$

where the ij element of $\underline{\underline{C}}$ is given by

$$C_{ij} = \sum_{j=1}^N a_{ij} b_{jk} \quad (11)$$

For a 3×3 matrices, for example, c_{13} is

$$c_{13} = a_{11}b_{13} + a_{12}b_{23} + a_{13}b_{33} \quad (12)$$

The systolic array architecture for carrying out this computation is shown in Figure 12.(3) The data are stepped through the engagement region in the sequence shown. Each of the boxes, c_{ij} , computes the produce of each pair of simultaneously incident quantities and accumulates a running sum of the products.

Because of the higher dimensionality of this problem, we have not been able to devise a reasonable design for a fully parallel matrix-matrix multiplier, although such designs are possible in the world of three-dimensional optics. We have, however, arrived at two IOC matrix-matrix multiplier designs which are based upon the engagement algorithm. The first of these is shown in Figure 13. The computational units are composed of a herringbone electrode structure which performs the multiplication, and a detector with sufficiently long time constant to perform the sums.

The intensity of the light diffracted by the herringbone structure is proportional to the product of the two analog voltages applied to the structure. These voltages must be stepped through the device in synchronism as suggested in the figure. This may be accomplished using an analog shift

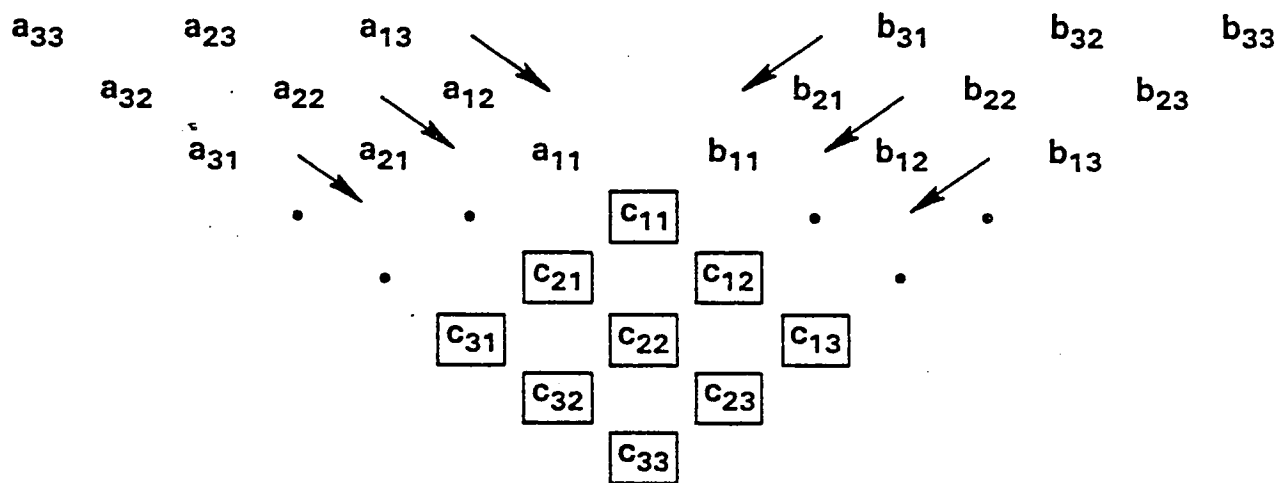


Figure 12. Systolic array architecture for matrix-matrix multiplication showing the flow of data through the computational elements. Each element performs the sum-of-products operation.

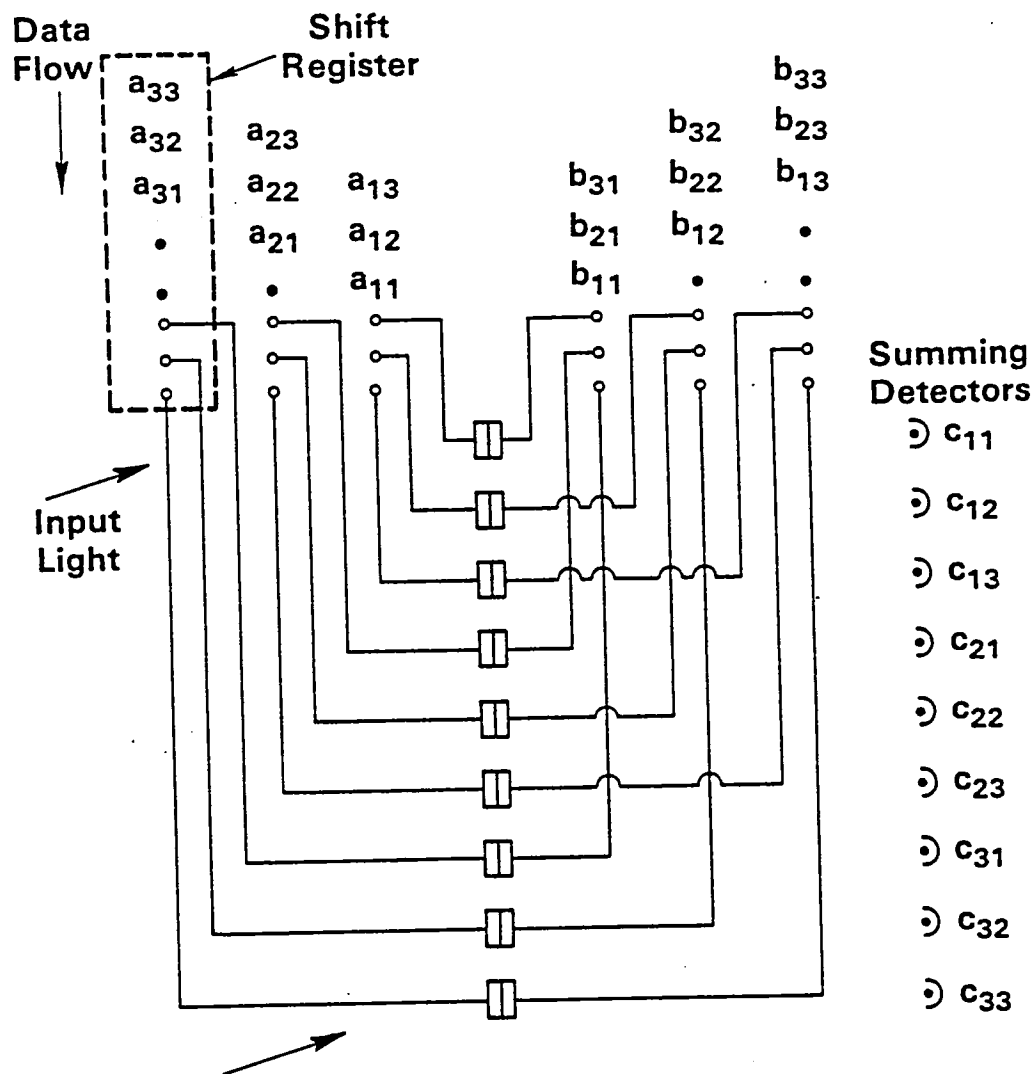


Figure 13. IOC for matrix multiplication based upon systolic array concept.

register or with digital shift registers and, for the multiplication of two $N \times N$ matrices, $2N^2$ D/A converters. At this time, the major problems with the IOC of Figure 13 are the massive amount of high speed electronics required and the fact that, for the configuration shown, a single IOC with N^2 elementary computational units must be employed. The second of these problems is overcome in the device shown in Figure 14.

The modified matrix multiplication IOC sketched in Figure 14 combines some of the features of Figure 13 with some of the features of the matrix-vector multiplier shown in Figure 11. As in the latter device, the herringbone structure has been split into two segments and beam splitters are used to distribute the information encoded in the light beam. The modified matrix multiplication IOC has the following advantages over the device suggested in Figure 13.

- Because the b_{rs} values are distributed optically rather than electronically, the data can, for most cases, be considered to be applied simultaneously to the appropriate a_{mn} matrix element array to advance in a rectangular rather than a skewed array. The result is to reduce the processing time by $N-1$ beats.
- The geometry of Figure 14 suggests that a natural split occurs after each row of A. Therefore, by using parallel B inputs to a number of IOCs, each IOC could calculate one of the row vectors of C, and these calculations could be done simultaneously.

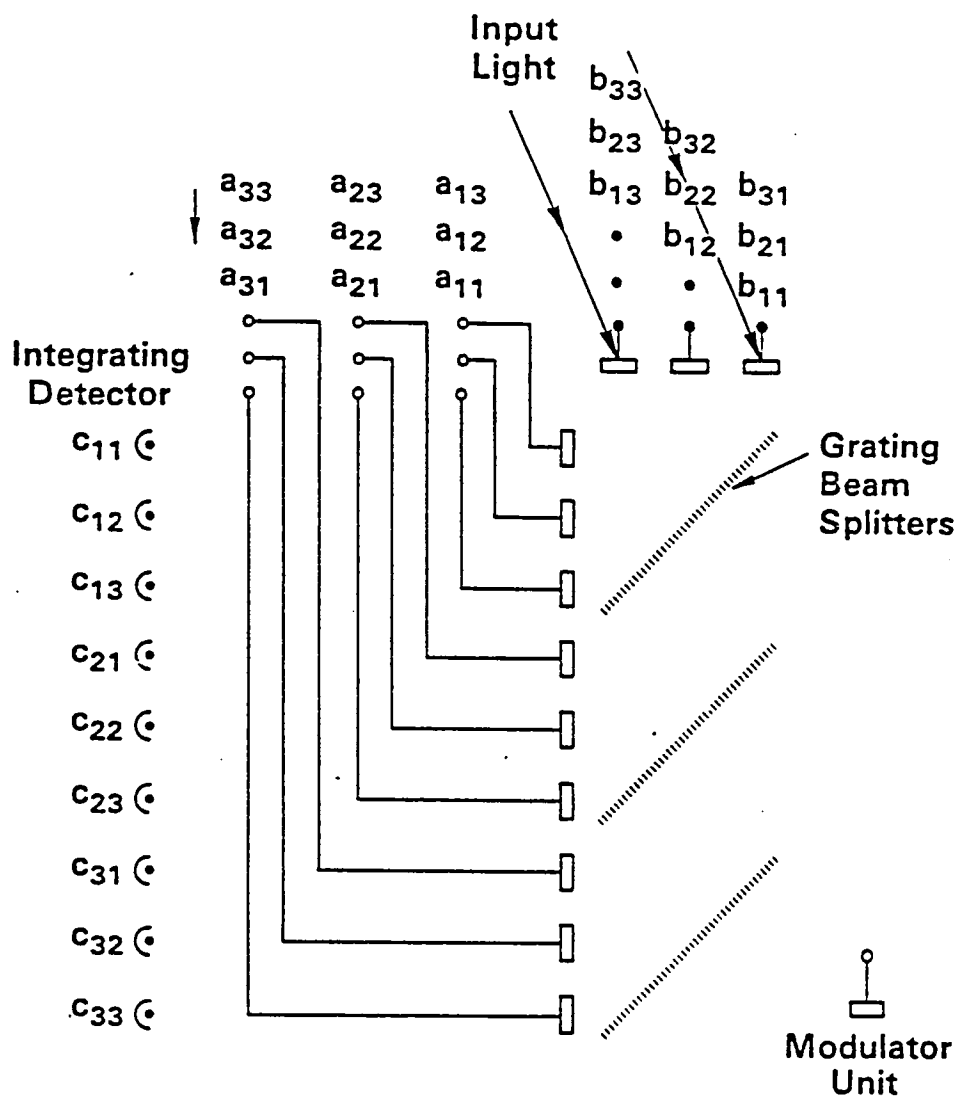


Figure 14. A modified IOC for matrix-matrix multiplication by the engagement algorithm. In this device almost half of the modulator units are replaced by the grating beam splitters which function to distribute the b_{ij} information in a manner similar to that shown in Figure 11.

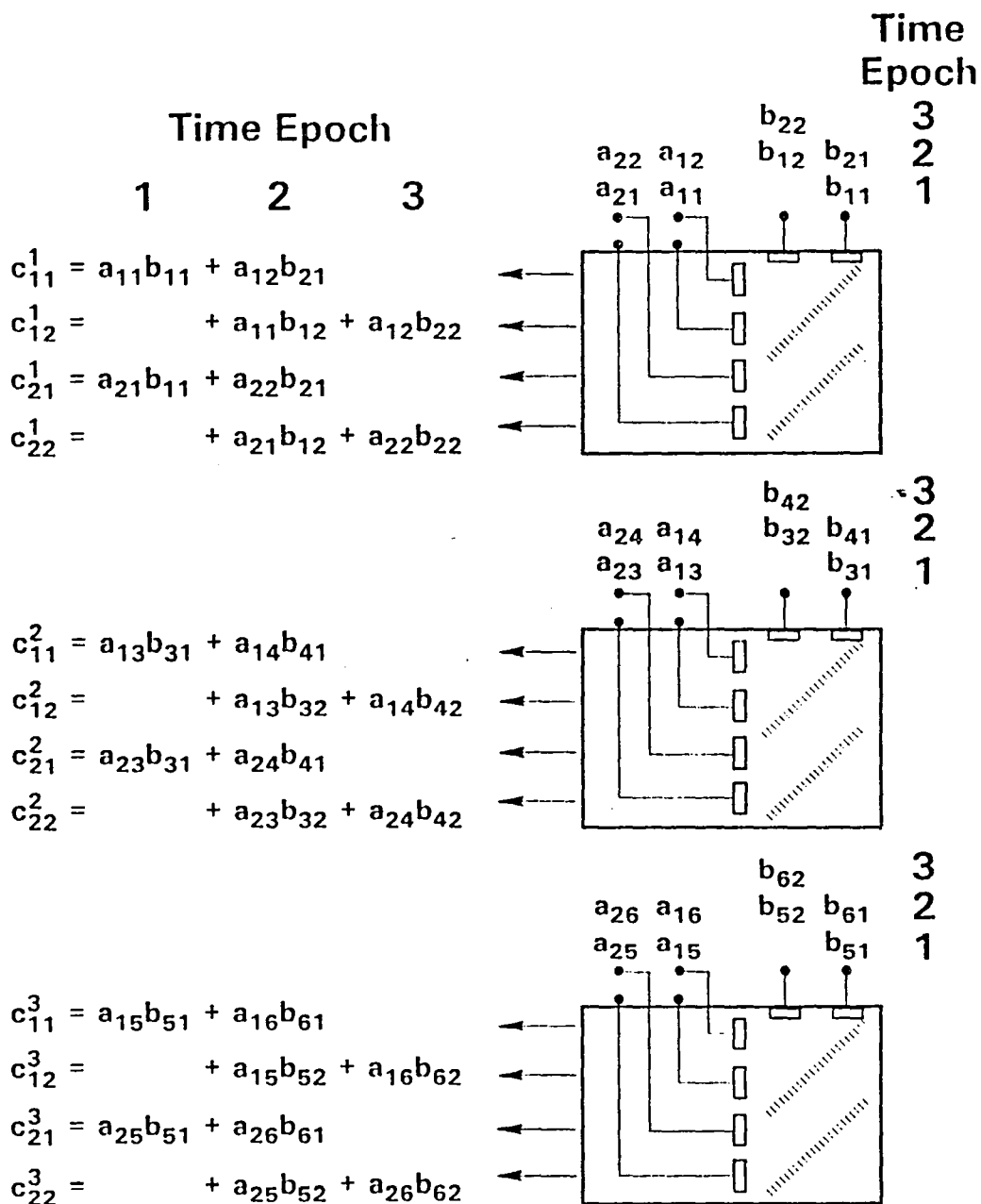


Figure 15. Using 3 2x2 processors to compute the products required for four of the terms in a 6x6 product. To complete the calculation the sums $C_{ij} = \sum_{k=1}^3 C_{ij}$ must be computed.

5. SOLUTION OF SYSTEM CONTROL EQUATIONS

A wide variety of problems of great interest to NASA are readily formulated in terms of large linear algebra problems which need to be solved very rapidly with a small, low-power-consumption computer. Tracking and mechanical control are examples of such problems. The universal tool for all tracking operations and indeed for most control operations is the Kalman filter. The Kalman filter is essentially a means of predicting the next number or, as is most commonly conceived, the next vector occurrence. It accomplishes this by estimating the next occurrence as the previous vector corrected by a factor proportional to the difference between the presently-observed vector and the predicted vector. The proportionality factor is the Kalman factor usually symbolized by the letter K. The Kalman estimated state vector is preferred over any measured value for two reasons. First, we seldom measure the state vector directly and our measurements often do not involve all of the components of the state vector. Second, our process and our measurement are noisy and hence subject to error which can be minimized by appropriate statistical techniques. Thus, the Kalman estimated state vector gives the statistically-best estimate of the true state vector we can obtain at the time.

Kalman filtering is usually regarded as so complicated that it must be accomplished in a digital computer. Thus the event is regarded as being discretized in time. Of course, the time interval must be chosen to be commensurate with the calculational speed of the computers involved in calculating the Kalman filter. For large problems, the Kalman filter can be calculated only if a variety of the system parameters remain constant with time. Actual NASA events of interest are continuous in time, so continuous Kalman filtering is appropriate. We believe it will be possible to set up simple analog optical computers to perform continuous Kalman filtering in real time.

The following brief mathematical description of Kalman filtering will suffice to show the computations which are involved.

We suppose we have a k dimensional state vector \vec{x} satisfying

$$\frac{d\vec{x}}{dt} = A(t)\vec{x} + \vec{n}(t) \quad (13)$$

where $A(t) = k \times k$ matrix which may vary with time, and $\vec{n}(t) = k$ dimensional noise vector which has an expected value of zero but a covariance matrix which may be time dependent. We measure an r -dimensional vector

$$\vec{y}(t) = M(t) \vec{x}(t) \quad (14)$$

where $M(t) = r \times k$ matrix which may be time dependent. Our goal is to find the best estimate $\vec{x}_e(t)$ to $\vec{x}(t)$ given $\vec{y}(t)$.

The Kalman filter makes use of all of the quantities just defined as well as of the continuously updated state vector covariance matrix $P(t)$ and the noise covariance matrix

$$E[\vec{n}(t_1) - \vec{n}(t_2)] = Q(t). \quad (15)$$

The Kalman gain function is

$$K(t) = \{[PA^T(t) + Q(t)]M^T(t) + PM^T(t)\} [M(t)Q(t)M^T(t)]^{-1}. \quad (16)$$

Using these, Fagin⁽¹²⁾ showed two equivalent optimum block diagrams for accomplishing the desired estimation. These look complicated but they need not be because many of the boxes each representing a matrix multiplication may contain a constant matrix. It is clear, however, that optimum estimation requires only matrix

- multiplication,
- transposition, and
- inversion

along with a memory for temporary storage of partial results.

Our consideration of optical architectures for the solution of the entire Kalman filter problem is by no means complete. However, we have begun to attack this problem in a systematic way, beginning with the realization that it is possible that the size of the matrix for a particular problem is too large to be handled by a single integrated optical processor.

Our approach to solving this problem is to:

- (1) design the appropriate integrated optical processors,
- (2) design suitable algorithms for those processors, and
- (3) assemble "small" processors into systems capable of operating on the full-sized matrix.

Steps (1) and (2) have been discussed above. We will now concentrate on ways to overcome hardware constraints on processor size.

The Multiplication of Large Matrices

The approaches we have suggested for constructing IOC's for carrying out matrix multiplication use IOSLMs or herringbone electrode structures which will probably be limited to a maximum of about 100 elements. This means that the engagement and the fully-parallel devices will be limited to matrices of about 100 x 100 and 10 x 10, respectively.

There are several reasons that the size of the IOC's is limited. The most important is that, for proper operation, it is necessary to illuminate the active region with a rather uniform, plane guided wave. It is not feasible to reduce the width of the individual modulator units to much less than 100 micrometers. It is also not practical to attempt to generate a uniform guided wave with a width more than 1 cm. These two figures combine to produce the 100-element limit.

Another limiting factor is the number of connections which can be made to a single IOC. Although this number certainly exceeds 100, the 200 connections which are required to address the 100 x 100 engagement processor is getting close to the upper limit.

The approach we use to overcome hardware constraint on the size of the matrix multiplier is based upon the fact that any matrix can be subdivided or partitioned into a number of smaller submatrices.⁽¹³⁾ When multiplying two conformable matrices which have been partitioned in a compatible manner, the submatrices can be treated just as if they were scalar elements. As a simple example we consider the product $\underline{\underline{A}} \cdot \underline{\underline{B}} = \underline{\underline{C}}$ where $\underline{\underline{A}}$, $\underline{\underline{B}}$, and $\underline{\underline{C}}$ are 6 x 6 matrices and the submatrices are 2 x 2.

$$\begin{bmatrix} A_{11} & A_{12} & A_{13} \\ A_{21} & A_{22} & A_{23} \\ A_{31} & A_{32} & A_{33} \end{bmatrix} \begin{bmatrix} B_{11} & B_{12} & B_{13} \\ B_{21} & B_{22} & B_{23} \\ B_{31} & B_{32} & B_{33} \end{bmatrix} = \begin{bmatrix} C_{11} & C_{12} & C_{13} \\ C_{21} & C_{22} & C_{23} \\ C_{31} & C_{32} & C_{33} \end{bmatrix} \quad (17)$$

where, for example,

$$C_{11} = A_{11}B_{11} + A_{12}B_{21} + A_{13}B_{31} = \begin{bmatrix} c_{11} & c_{12} \\ c_{21} & c_{22} \end{bmatrix} \quad (18)$$

Note that each term in Eq. 18 is a 2 x 2 matrix product and each contains a contribution to C_{11} , C_{12} , C_{21} , and C_{22} , which are four of the desired 36 matrix components. It is obvious that the algorithm which allows us to avoid performing a large matrix multiplication demands that we not only perform a large number of smaller multiplications, but that we devise a system for carrying out the required additions.

In the example discussed above, we have replaced a 6x 6 matrix multiplication with 27 2x2 multiplications and 36 3 - number sums. In a more realistic example we might have chosen to carry out a 128 x 128 multiplication with 512 16 x 16 processors. The final output would then be 128 8-number sums. In general we can perform an NM x NM matrix-matrix multiplication by N^3 MxM multiplications. The memory required is no more than that needed to perform any NM x NM matrix multiplication because the submatrices can be accumulated.

The matrix-multiplication engagement processor could be used as the basic IOC for carrying out the submatrix multiplications. It requires $2N-1$ clock pulses to perform an N-dimensional matrix multiplication. The data flow for C_{11} of the 6 x 6 example is shown in Figure 15. The sums can be carried out optically by arranging the processors so that all of the appropriate optical outputs fall on a common detector, or electrically with individual detectors for each processor and a series of summing circuits. Note that since all of the submultiplications can be carried out in parallel, there is a potentially large reduction in the processing time. Assuming that there is a convenient way of formatting the data into the proper sub-groups, that the data are clocked into the processor at a constant rate for all examples, and that optical summing is used there is a factor of 11/3 reduction in our 6 x 6 example, and a factor of 225/31 reduction in the processing time for the

128 x 128 example. There is an obvious hardware/processing-time tradeoff which makes this a very attractive approach to consider for handling large problems.

Another approach to this problem which used a single IOC but more electronic hardware is discussed in Appendix B. The question of numerical computation is addressed in Appendix C.

Matrix Inversion

Because matrix-matrix multiplications require the same order of magnitude of calculations as matrix inversion the concept of using an iterative matrix-matrix inversion scheme is of no interest for electronic digital computation. Recently, however, several schemes for optical matrix-matrix inversion scheme is of no interest for electronic digital computation. Recently, however, several schemes for optical matrix-matrix multiplication have been devised.^(14, 6, 15) Because these allow very fast computation, it is of interest to apply this technique to various problems in linear algebra. One such problem, eigenvector/eigenvalue solution, is easily attacked by a matrix power method described elsewhere.⁽¹⁶⁾ Here we describe the inversion of the matrix A by iterative matrix-matrix method.

The k^{th} row of the matrix product AB has as its j^{th} column

$$C_{j,k} = \sum_{\ell} a_{j\ell} b_{\ell k} \quad , \quad (19)$$

where the a's and b's are the components of A and B. If now we fix k we find that we do not need all of the elements of B to calculate C_{jk} . Rather we need only $b_{1k}, b_{2k}, \dots, b_{Nk}$, the k^{th} column of B. We want the particular case

$$C_{jk} = \delta_{jk} = \begin{cases} 1 & \text{if } j = k \\ 0 & \text{if } j \neq k \end{cases} \quad (20)$$

Thus we can write

$$C + I = [\delta_{j1} | \delta_{j2} | \dots | \delta_{jN}] \quad (21)$$

and

$$B = A^{-1} = [b_{j1} | b_{j2} | \dots | b_{jN}]. \quad (22)$$

We compute A^{-1} by solving N equations of the form

$$A \vec{b}_k = \vec{c}_k \quad (23)$$

where

$$\vec{b}_k = (b_{1k}, b_{2k}, \dots, b_{Nk})^T \quad (24)$$

and

$$\vec{c}_k = (\delta_{1k}, \delta_{2k}, \dots, \delta_{Nk})^T. \quad (25)$$

Fortunately the literature is replete with iterative solutions to Equation 23. For example, Ralston(17) gives three methods. Of these, one (the Gauss-Seidel method) converges for any positive definite A and converges faster than the other two methods discussed.

We now show how the Gauss-Seidel method can be extended to matrix inversion. Write

$$A = L + U + D, \quad (26)$$

where D is a diagonal matrix and L and U are, respectively, lower and upper triangular matrices. We have

$$AA^{-1} = I$$

or

$$(L + U + D)A^{-1} = I.$$

Therefore

$$(L + D)A^{-1} = -UA^{-1} + I$$

and

$$A^{-1} = -(L + D)^{-1}UA^{-1} + (L + D)^{-1}I. \quad (27)$$

We start with some "approximate" inverse matrix $(A^{-1})_0$ and calculate an improved solution

$$(A^{-1})_1 = -(L + D)^{-1}U(A^{-1})_0 + (L + D)^{-1}I, \text{ etc} \quad (28)$$

Ralston shows that if A is positive definite, this iteration converges independently of our choice of $(A^{-1})_0$. Writing

$$B = -(L + D)^{-1}U \text{ and}$$

$$C = (L + D)^{-1}I = (L + D)^{-1}$$

the iteration is

$$(A^{-1})_{n+1} = B(A^{-1})_n + C. \quad (29)$$

The multiplication by B is easily carried out by optics. The addition of C can be carried out electronically.

Finding B is a far easier task than inverting A, because L+D is essentially lower triangular.

With no precalculation at all we can do Jacobi iteration:

$$(A^{-1})_n = -D^{-1}(L + U)(A^{-1})_{n-1} + D^{-1} \quad (30)$$

This is because inverting D is totally trivial:

$$d_{ij} = d_{ii}\delta_{ij} = (d_{ij}^{-1})^{-1}.$$

This is not guaranteed to converge unless the Euclidean norm of $D^{-1}(L+U)$ is less than one. This is often the case, so the convenience of not having to invert (L+D) may lead to a preference for this method.

An iterative linear equation solver proposed for optical solution to

$$A\vec{x} = \vec{b}, \quad (31)$$

is

$$\vec{x}_n = (I + A)\vec{x}_{n-1} - \vec{b}. \quad (32)$$

This has the same sort of convergence burden of proof ($\|I + A\| < 1$) as the Jacobi method. Reworked, it reads

$$(A^{-1})_n = (I + A)(A^{-1})_{n-1} - I. \quad (33)$$

A general block diagram for the iterative solution of the equation

$$BM_i + C = M_i + 1 \quad (34)$$

is shown in Figure 16.

Example: Matrix Inversion
 $BM_i + C = M_{i+1}$

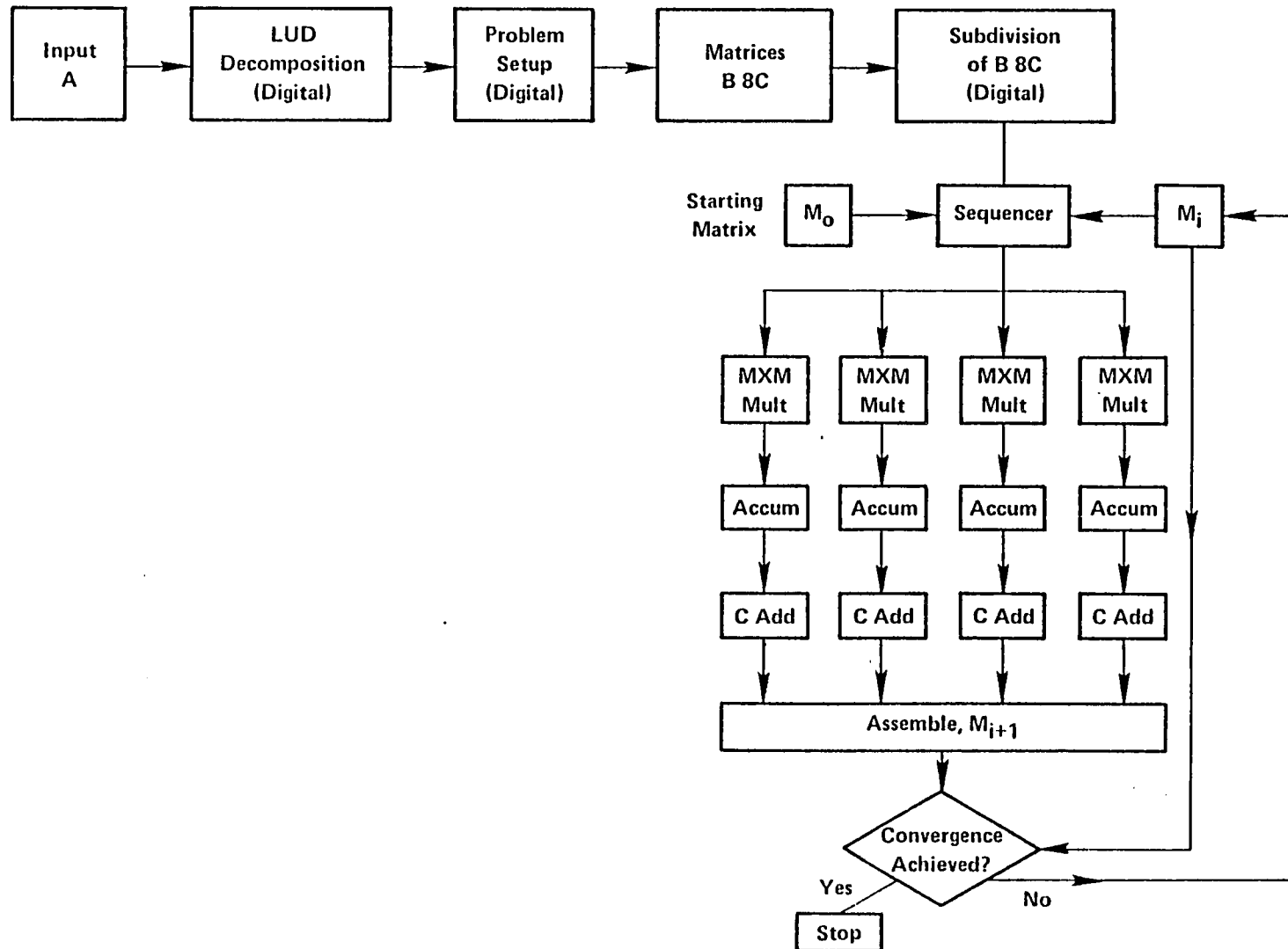


Figure 16. A flowchart for iterative matrix inversion.

III. LUNEBURG LENSES

6. INTRODUCTION

The objective of this portion of the program is the development of procedures for the design, fabrication, and testing of Luneburg lenses for integrated-optical devices. The lenses are produced by deposition of arsenic trisulfide glass layers of prescribed profile onto the surface of optical waveguides made by the diffusion of titanium into Y-cut lithium niobate crystals.

A conventional Luneburg lens for use in planar integrated optics consists of a layer of high-refractive-index material deposited on a portion of an optical waveguide and radially symmetric about an axis through the center of the lens and perpendicular to the plane of the guide. The effective refractive index of the guided mode is changed locally by an amount dependent on the thickness of the overlay at the point in question. The Luneburg lens is an example of a gradient-index lens, in which focusing occurs because of the difference in refractive index between adjacent rays. If the lens profile--thickness as a function of radius--is properly chosen, a perfect geometric focus can be obtained; that is, the lens will be diffraction-limited. The geodesic lens and the diffraction, or grating, lens are other types of waveguide lenses that may be produced with short focal lengths. The relative merits of these types of lenses are discussed in our paper "Evaporated As_2S_3 Luneburg Lenses for $\text{LiNbO}_3\text{:Ti}$ Optical Waveguides," for which a full bibliographic reference may be found in Appendix D to this report.

Just as there are several types of waveguide lenses which should be considered for a given application, there are a number of materials which need to be evaluated if a Luneburg lens is to be used. The lens material should have a refractive index higher than the waveguide surface index, should not cause excessive absorption or scattering of the guided light, and should be easy to deposit on the waveguide surface. For lenses on LiNbO_3 waveguides, arsenic trisulfide glass is one of the few known materials to meet these criteria. Arsenic triselenide and more complex chalcogenide glasses also have high refractive

indices, but they have fundamental absorption edges more toward the infrared and cannot be used in the visible. ZnS and CdS have large energy gaps and high indices of refraction, and they can be deposited on LiNbO₃. These materials form polycrystalline films; obtaining films of good optical quality requires some care. Certain oxides, such as TiO₂, might also be used with LiNbO₃ waveguides. It is difficult to keep the oxygen content of deposited oxide films high enough to obtain a refractive index comparable to those of the crystal, although some sputtered TiO₂ films on LiNbO₃ with refractive index as high as 2.6 have been prepared (R. Holman, personal communication. The optical quality of these films was not further assessed.)

In the remainder of this portion of the report, we will first describe our procedures for fabricating and testing the optical waveguides and the As₂S₃ layers. Then we will describe the procedures for designing Luneburg lenses of prescribed characteristics and for designing masks suitable for making, by evaporation or sputtering of the glass, lenses of the desired profile. Ray-tracing will be seen to play a significant role in assessing the adequacy of these designs. Finally, we describe the fabrication and testing of some selected lenses, and we conclude by summarizing the progress made, the problems encountered, and the questions remaining.

7. WAVEGUIDE AND SUBSTRATE

For all but the most preliminary work, it is necessary for accurate lens design to know the refractive index of the guided mode and the index at the guide surface to the third decimal place. This means, in turn, that the waveguides have to be fabricated by a reproducible process on well-characterized substrates. Commercial lithium niobate crystal plates are somewhat variable in optical properties and diffusion coefficients, complicating the characterization process. In parallel work, we are attempting to correlate such variable properties with one another and with factors such as sample stoichiometry in order to allow production of waveguides of fully predictable behavior.

In the process most frequently used to make the waveguides employed in the present experiments, a film 17.5 nm thick of high-purity titanium is deposited on the LiNbO_3 crystal surface. The titanium is then indiffused at 1000 C for 2.5 h in an atmosphere of slowly flowing oxygen which has been bubbled through water at 90 C. The water vapor compensates for out-diffusion of lithium which occurs during the diffusion anneal. This procedure produces waveguides supporting a single mode of each polarization at wavelength 633 nm. As no residual diffusant remains on the surface, the waveguide is presumed to have a depth profile of approximately Gaussian shape. To describe such a profile, two parameters--the surface index and the diffusion depth--are required, and both cannot be obtained from the propagation constant of the guided mode, but reasonable extrapolations can be made from data on two- and three-mode guides. In some cases, guides supporting more than one mode of a given polarization have been used. Of course, only one mode can be expected to be sharply focused by the lens.

To determine to sufficient accuracy the waveguide surface index, we need to know, in addition to the mode indices and something about the refractive index profile in the guiding layer, the substrate refractive index. We have found that this quantity can be measured quite accurately by a recently described⁽¹⁸⁾ prism coupling method. In our implementation of this method, a symmetrical SrTiO_3 prism is clamped to the sample, as shown in Figure 17, and light is brought to the prism-sample interface through one remaining prism face much as one excites a propagating mode in a waveguide with a prism coupler. The amount of light reflected from the prism-sample interface is recorded as the angle of incidence is varied. When the angle of total internal reflection at the interface is approached, the reflected intensity increases rapidly. In spite of effects of imperfect beam collinearity and varying air gaps between the prism and sample, it is generally easy to determine the angle of total internal reflection to within $1'$ of arc and thence to calculate the sample refractive index to ± 0.0001 or better. The refractive index and angles of the prism are found in the conventional way using a prism spectrometer. The ordinary refractive

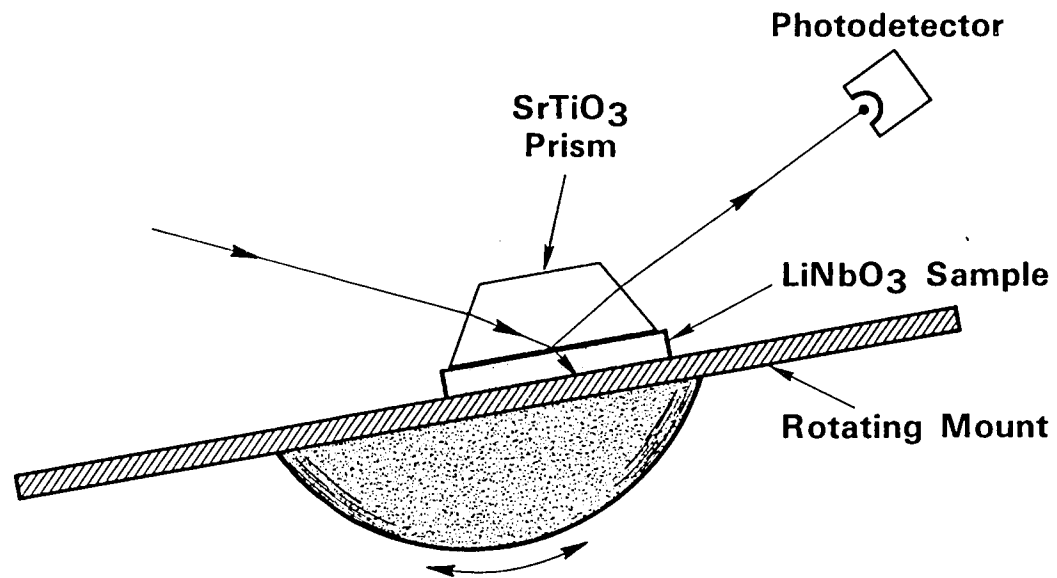


Figure 17. Prism-coupling method for measuring refractive indices of LiNbO_3 plates.

index of lithium niobate varies little from sample to sample, a typical value at 633 nm wavelength being 2.2865. The extraordinary index is more variable, ranging from 2.1996 to 2.2032, presumably as a result of changes in stoichiometry.⁽¹⁹⁾ This method has the advantage that measurements may be carried out either before or after the waveguide layer is formed. When the waveguide is present, it is possible under favorable circumstances to determine the guided-mode indices as well (H. Onodera, personal communication). More often, however, these values are obtained using rutile prisms to couple into and out of the guided modes. Measurements on one waveguide supporting two modes of each polarization yielded the following representative results for the TM polarization:

substrate index	2.2868
0-order mode index	2.2892
surface index	2.300
diffusion depth	2.2 μm

assuming a Gaussian profile and the validity of the WKB approximation⁽²⁰⁾ for evaluating the surface index and the waveguide depth. This waveguide was used in several of our experiments on determining the refractive index of the deposited films and the data given above have been used in some of our more recent lens designs.

8. As₂S₃ FILM DEPOSITION

Arsenic trisulfide film lenses have been fabricated by two physical-vapor-deposition processes, rf-sputtering and thermal evaporation. Uniform-thickness films were also prepared by these methods for measurement of the film optical properties. In this section we describe the film deposition methods and the methods for determining the principal properties of the films prepared.

The experimental arrangement for making As₂S₃ films by thermal evaporation is illustrated schematically in Figure 18. The process is carried out in a conventional bell-jar high-vacuum evaporation system, pumped down to a pressure of 1.0×10^{-5} torr at the start of the evaporation.

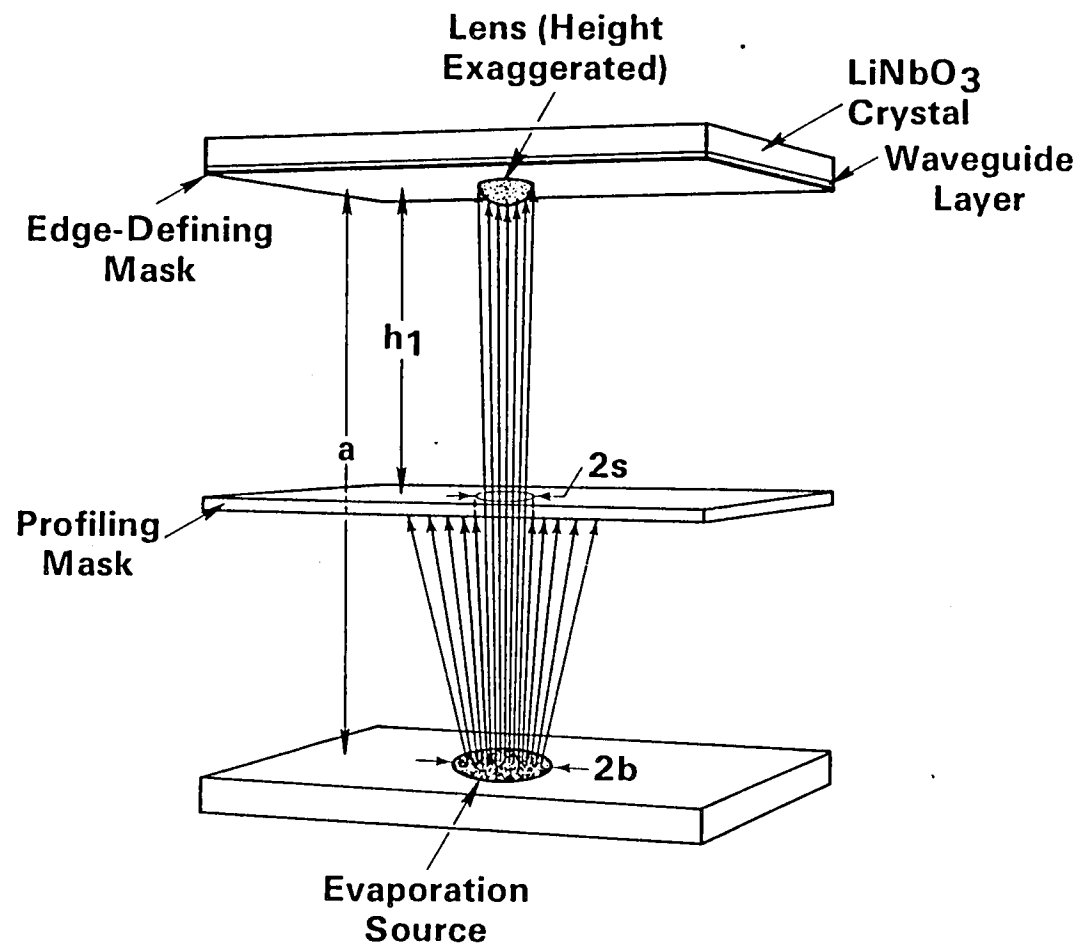


Figure 18. Experimental arrangement for making arsenic trisulfide Luneburg lenses by evaporation. Not shown is a piezoelectric thickness gauge mounted close to the crystal.

The source is 99.99% pure As_2S_3 fused glass which has been hand-ground in a porcelain mortar and pestle to a fine powder, approximately 325 mesh. The powder is evaporated from a quartz crucible, 18 mm in diameter at the top, held in a tungsten basket. Best results are obtained when the crucible is around half full. The evaporation temperature is estimated to be in the 500 to 700 C range and the source-to-substrate distance is typically 100 mm. In most experiments, the film deposition rate was around 20 nm/sec. Lenses fabricated at deposition rates of 2 nm/sec had similar properties to those deposited at the higher rate. The masks, which are used to shape the deposit to the desired thickness profile, are made of thin sheets of aluminum. The crystal substrate was not heated or cooled during the evaporation.

Sputtering of As_2S_3 thin films was first described by Watts and co-workers⁽²¹⁾. Our experiments were carried out using the same vacuum system used for the evaporation work. A special baseplate was constructed allowing easy conversion of the system between the two deposition methods. For deposition of chalcogenide glasses a dedicated system is needed because of the relatively high vapor pressure of the materials.

The experimental arrangement for rf sputtering is indicated in Figure 19. Not shown in the drawing is a movable aluminum mask which may be inserted just above the thick profiling mask and the film thickness gauge in order to permit presputtering of the target. The target is a polished disk of 99.99% pure As_2S_3 glass, 102 mm in diameter and 6 mm thick, obtained from Unique Optical Company, Farmingdale, NY. It was fastened to the target electrode with Epon epoxy resin. Before the target was used, it was presputtered for 12 h to remove contaminants. It is kept under vacuum when not in use. Most of the substrates used are 3 mm thick; so the target-to-substrate distance is 23 mm. The sputtering gas is argon, either standard laboratory grade or high-purity. One attempt at sputtering in high-purity nitrogen yielded a whitish powdery deposit, which was not analyzed. To produce films, the system is pumped down to about 8×10^{-6} torr; then gas is admitted and the films are sputtered at about 35 μm argon pressure. The operating frequency is 13.56 MHz and the sputtering is typically done at 20 W forward power.

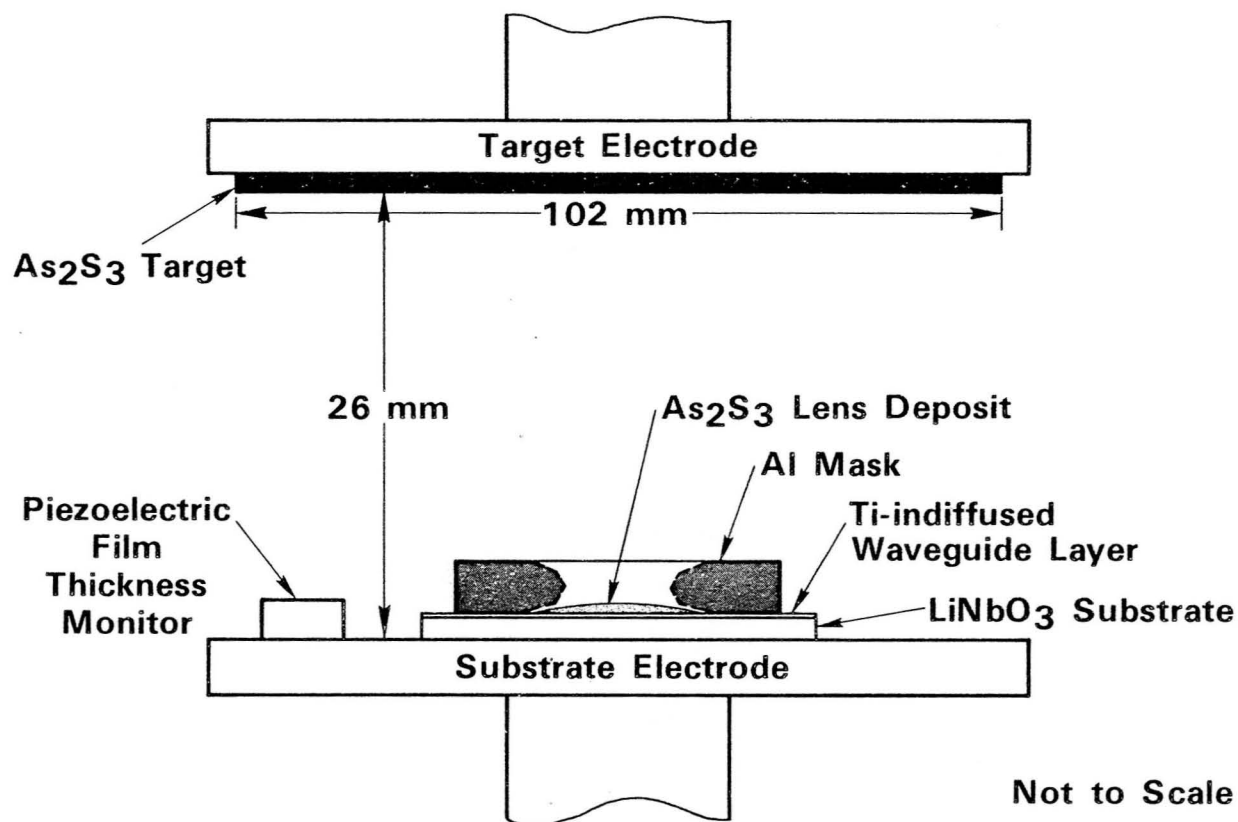


Figure 19. Experimental arrangement for making arsenic trisulfide Luneburg lenses by rf sputtering. Not shown is a movable shutter to allow pre-sputtering of the target.

The film deposition rate is typically 12 nm/min, but can be varied from 10 to 18 nm/min at this power, depending on the standing-wave ratio and the other conditions.

Both methods yield films which adhere well both to glass and to lithium niobate substrates. Under magnification, the initial sputtered films appeared smoother. Evaporated films often show small pockmarks and granules adhering to the surface, which seldom, however, affect the optical properties of lenses or other films in any obvious way. Problems were encountered, on the other hand, with some of the sputtered films after the system had operated a while, as discussed below.

Once films have been prepared under specified conditions, their properties are measured. The minimal set of parameters that must be determined for design and fabrication of lenses is

- (1) thickness, and thickness profile in the case of lenses;
- (2) film refractive index at the design wavelength (the 633 nm line of a He-Ne laser in all the work reported here); and
- (3) change in refractive index upon illumination with short-wavelength light or upon annealing just below the glass transition temperature⁽²²⁻²⁴⁾. This phenomenon may be used to adjust lens properties after fabrication, or it may lead to gradual change in lens properties over time if the lenses are not either protected or fully desensitized by intentional annealing or illumination.

We will describe measurements of each of these parameters in turn.

1. Lens shape and film thickness. The overall thickness of the lens is fixed by measuring the mass of material deposited on a piezoelectric thickness monitor mounted near the crystal, but away from the masks. The mass/thickness ratio is determined by profilometer thickness measurements on test specimens. The profilometer, a Taylor-Hobson Talysurf 4, or more recently a Talysurf 6, is also the principal instrument used to determine the lens profile. The stylus does not damage the arsenic trisulfide glass or the waveguide layer, and it is not difficult to make a traverse through the thickest part of the lens. One difficulty with Talysurf measurements is that the substrate is often found not to be flat; so an extrapolation of substrate surface position beneath the lens is required in order to determine the lens thickness. Deposition of the lens may cause some warping of the substrate. Departures from planarity are not sufficient, though, to have any effect on the properties of the guided waves or on the lenses.

The profilometer work is complemented by interferometry. A Twyman-Green arrangement is used to provide interferograms of the lens shape; an example is shown in Figure 20. Both white-light and monochromatic illumination yield informative fringe patterns. The interferograms are particularly good for detecting shape distortions resulting from misalignment of masks or from substrate imperfections.

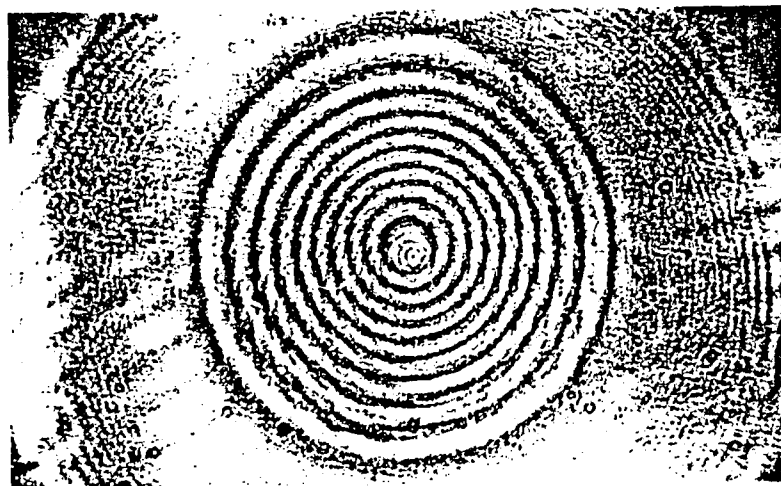


Figure 20. Twyman-Green interferogram of arsenic trisulfide
Luneburg lens 1 cm in diameter.

2. As₂S₃ refractive index. The refractive indices at 633 nm of arsenic trisulfide films deposited according to our procedures have been measured by a prism deflection technique. Prisms of uniform thickness and apex angle 30° are deposited on LiNbO₃ waveguides through triangular masks held close to the guide. The prisms are oriented symmetrically with respect to the z-axis of the crystal and a 633 nm guided beam is coupled into the waveguide so it propagates along the x-axis of the y-cut crystal. After the beam is deflected by the overlay prism, it is end-fired out of the guide through a polished edge and its deflection measured on a screen about a meter away. Because of the steep edges of the prism, some light in the prism region is frequently scattered at the input edge into higher-order modes supported in this region. The light is subsequently scattered back out into the substrate fundamental mode at the output edge; so there are often 2 or 3 deflected beams corresponding to different modes in the prism region. From each observed deflection we calculate a mode index in the prism region, and from each mode index we calculate, using a program similar to that used to determine the lens thickness profile, a value for the refractive index of the overlay material.

The unweighted average of 16 such determinations, measured on 6 evaporated prisms varying between 0.28 and 1.21 μm in thickness, was 2.446 ± 0.006 . Two different substrates were used, and the modes observed were 6 TE₀, 6 TM₀, 3 TE₁ and 1 TM₁. The range of refractive indices found was 2.38 to 2.48; while this is larger than desirable, most of the values clustered well around the mean. The mean for the 7 TM modes was 2.445, while for the 9 TE modes it was 2.447. The value 2.445 was adopted for design work on evaporated lenses not to be subjected to ultraviolet illumination.

A similar experiment was carried out using a sputtered prism $0.93\text{ }\mu\text{m}$ thick. A single TM beam was observed in the output when TM-polarized input was used, and two TE output beams were found with TE input. From the deflection of the TM_0 beam, a film index of 2.61 ± 0.005 was calculated. To obtain similar values for the beams with TE polarization, it was necessary to assume that they corresponded to excitation of the TE_2 and TE_3 modes in the prism region; it was verified that a prism of this thickness would support these two additional modes. The film indices obtained on this assumption were 2.63 and 2.56. A value of 2.58 was adopted for the design calculations on sputtered lenses; this value will also be seen to be appropriate for evaporated lenses which are annealed or exposed to ultraviolet. The absence of deflected beams corresponding to the TE_0 and TE_1 modes in the prism may indicate that these beams were absorbed or very effectively scattered into the higher-order modes or out of the waveguide. The high refractive index of the sputtered films is most easily explained by assuming that they have undergone during their formation a maximum photo-induced refractive-index increase as a result of the large amount of blue and ultraviolet light present in the sputtering glow discharge.

3. Ultraviolet-induced change in refractive index. The dynamic photoinduced index was determined by measuring the change in the deflection of a guided TM_0 beam by an evaporated As_2S_3 prism as the prism was illuminated with an ultraviolet lamp. This prism again had apex angle 30° ; it was $0.60\text{ }\mu\text{m}$ thick. The single-mode waveguide on which it was placed had polished end faces. The input coupling prism and the crystal were all enclosed in a plastic box through which dry argon flowed throughout the experiments. The ultraviolet illumination, strongest at 400 nm, impinged on the prism through the top of the box. The intensity of the 400 nm line at the

sample, with the box cover in place, was 1.10 mW/cm^2 . There was a small change in refraction by the prism between the time it was first made and when it was used in these experiments. This preliminary change in film index was equivalent to about 10 minutes extra exposure to the uv source. For exposure times up to about 3 hours, the refractive index of the As_2S_3 as measured by the deflection of the TM_0 mode may be expressed as

$$n = 2.5820 - 0.1295 \exp (-E/5.739), \quad (35)$$

where E is the total uv exposure (400 nm line) in J/cm^2 . This expression is consistent with a model in which the rate of photoinduced index change is simply proportional to the remaining amount of unaltered material. For longer exposures, the film index increases above the saturation value indicated by Equation (35) to 2.594. This effect is probably related to heating of the sample by the uv lamp. The prism region also supported a TM_1 mode; the dynamics of the index change measured using deflection of this mode were very similar to those with the TM_0 mode, but the calculated initial film index for this mode was about 0.02 higher than for TM_0 . After 6 hours exposure, a TM_2 mode of even higher apparent index showed up. The observed index changes and model curves fitted to an equation of the type of (35) are shown in Figure 21. While heating of the sample seems to be an important influence on the values obtained at long times, the displacement of the curves from one another should not go unremarked. This difference might result from some dependence of film composition, and consequently photosensitivity⁽²³⁾, on evaporation time, but there is also greater uncertainty involved in determining the film index from the properties of the higher-order modes. Refractive index increases similar to those produced by exposure to uv can also be induced by annealing^(24,25). We obtained similar changes in refractive index by annealing films at 190 C for 1 hour in slowly flowing dry argon or nitrogen.

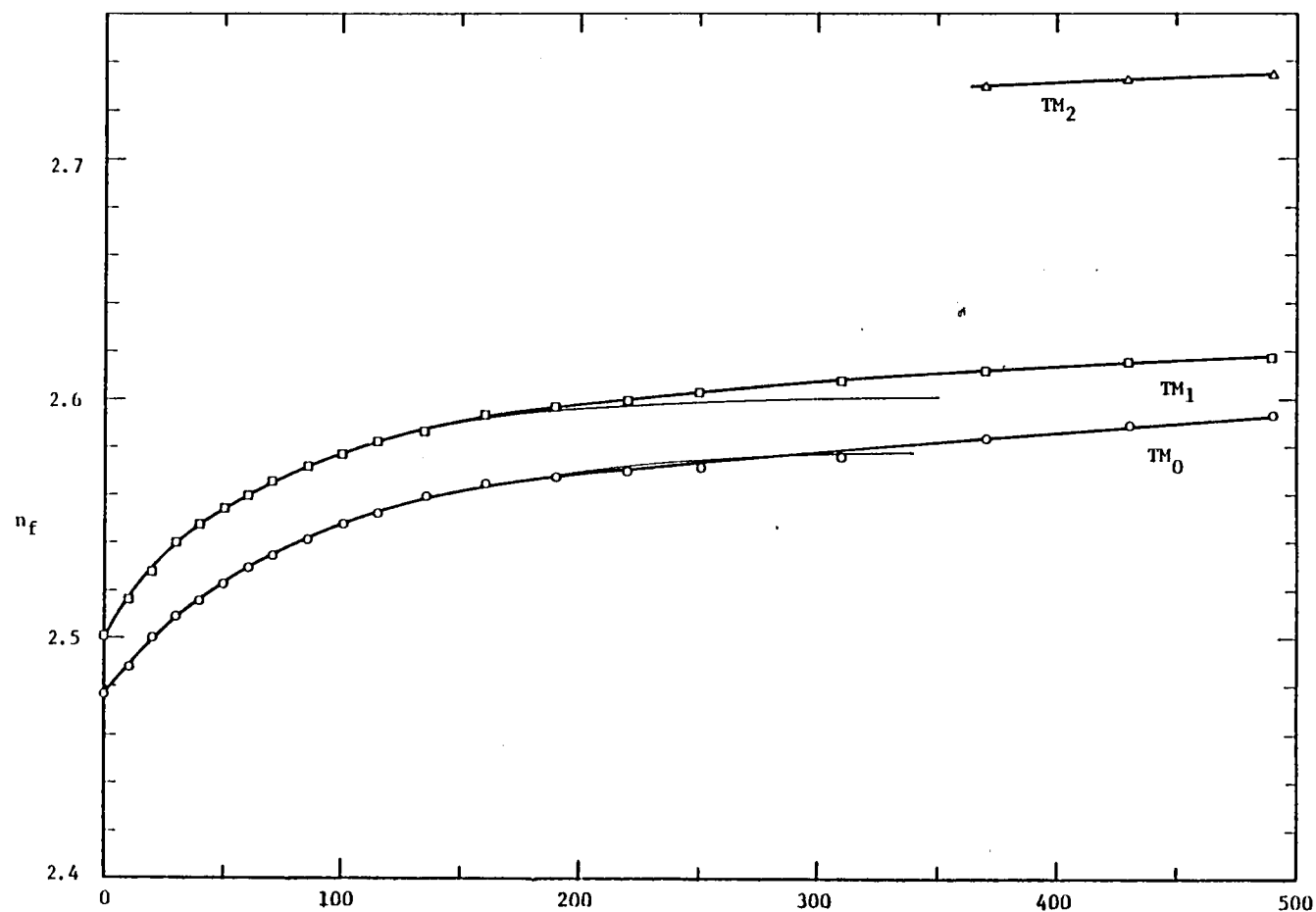


Figure 21. Apparent refractive index of As_2S_3 film prism as function of time of exposure to 1.1 mW/cm^2 of ultraviolet light, as determined by deflection of 3 different modes supported in prism region. Heavy lines connect data points; light lines are fits to data of the form $n_f = a - b \exp(-t/\tau)$.

Sputtered films were exposed to ultraviolet in a similar way for up to 12 hours with no significant change in their refractive properties. Annealing as described above also had no effect. This is consistent with the idea that these films as made have about the maximum refractive index possible for films of their composition.

9. LENS DESIGN

To describe the lens design, mask design, and ray-tracing work, it will be helpful to follow through a single example. We will consider a lens of diameter 12 mm designed to focus a 10 mm wide TM_0 beam at a distance of 21 mm, measured in the waveguide, from the lens center. The guide will be taken to be the one described earlier, with surface ordinary index of 2.300 and TM_0 mode index of 2.2892. The lens deposit, either sputtered or evaporated and annealed, will be taken to have a refractive index of 2.58, and the design wavelength in air is 633 nm. The design speed is $f/2.1$ in terms of the design useful aperture, or $f/1.75$ in terms of the total aperture. In terms of the back focal length often used by lens designers, the corresponding values are $f/1.5$ and $f/1.25$.

To determine the required refractive index profile, we solve the integral equation^(26,27)

$$\ln \frac{N(r)}{N_{\text{ext}}} = \frac{2}{\pi} \int_0^{(t-z)^{1/2}} \frac{\sin^{-1}(u^2 + z)}{(u^2 + 2z)^{1/2}} du. \quad (36)$$

In this equation, $N(r)$ is the mode index at radial distance r in the lens region, while N_{ext} is the mode index outside the lens, 2.2892 in our example. The parameter t is the reciprocal of twice the full-aperture f /number of the lens, or 0.2857, and $z = tR$, where $R = 2r N(r)/A N_{\text{ext}}$. A is the full lens aperture, 12 mm. In the form presented here, the integral is easily evaluated to 5 decimal place accuracy by a single 16-point Gaussian quadrature. The parameter R will be seen to range between zero and unity. To determine the index profile, we select a suitable set of values of R and for each one evaluate the integral; each evaluation yields a value for $N(r)/N_{\text{ext}}$, and

from this we finally determine from the definition of R the value of r to which the calculation applies. The refractive index profile is shown in Figure 22.

To find the lens thickness profile corresponding to this refractive-index profile, we take the waveguide to have a Gaussian profile with a diffusion length of $2.2\text{ }\mu\text{m}$, a surface index of 2.300, and a bulk index of 2.2868. The values other than the surface index are not highly critical to the accuracy of the calculations. Since the lens thickness varies slowly with radius, we model the situation at a given radius as a uniform layer of lens material covering the inhomogeneous waveguide. We made a straightforward extension of the calculation method devised by Southwell⁽²⁸⁾ to this case, assuming that the waveguide layer in the LiNbO_3 could be described within the WKB approximation. In most of the lens region, the major portion of the optical energy is drawn into the lens layer, and the electric field of the optical wave decays throughout the substrate. Under such circumstances, a simplified three-layer waveguide approximation may be used. This analysis applies, strictly speaking, only to TE modes, except of course that index values appropriate to the TM_0 mode in the LiNbO_3 are inserted into the calculation. While this is in most circumstances a fairly good approximation, it should be corrected for more accurate lens design⁽²⁹⁾; as we shall see, the present design happens to be one in which this part of the analysis is inadequate for peripheral rays. The calculated thickness profile, normalized to unity at the lens center, is shown in Figure 23. The design central thickness is $0.39\text{ }\mu\text{m}$.

10. MASK DESIGN

To design a set of shadowing masks which will yield a lens deposit of the desired thickness-vs-radius profile, we need suitable models of i) the molecular detachment process at the evaporation or sputtering source, ii) the transport through the masks to the substrate, and iii) the deposition process at the substrate. Given these, we then require a straightforward but tedious search procedure to determine the positions and apertures of the necessary masks. In devising the models and computational procedures, we have drawn on previous work on mask design for sputtered⁽³⁰⁻³²⁾ and evaporated⁽³³⁾ lenses for glass substrates, although

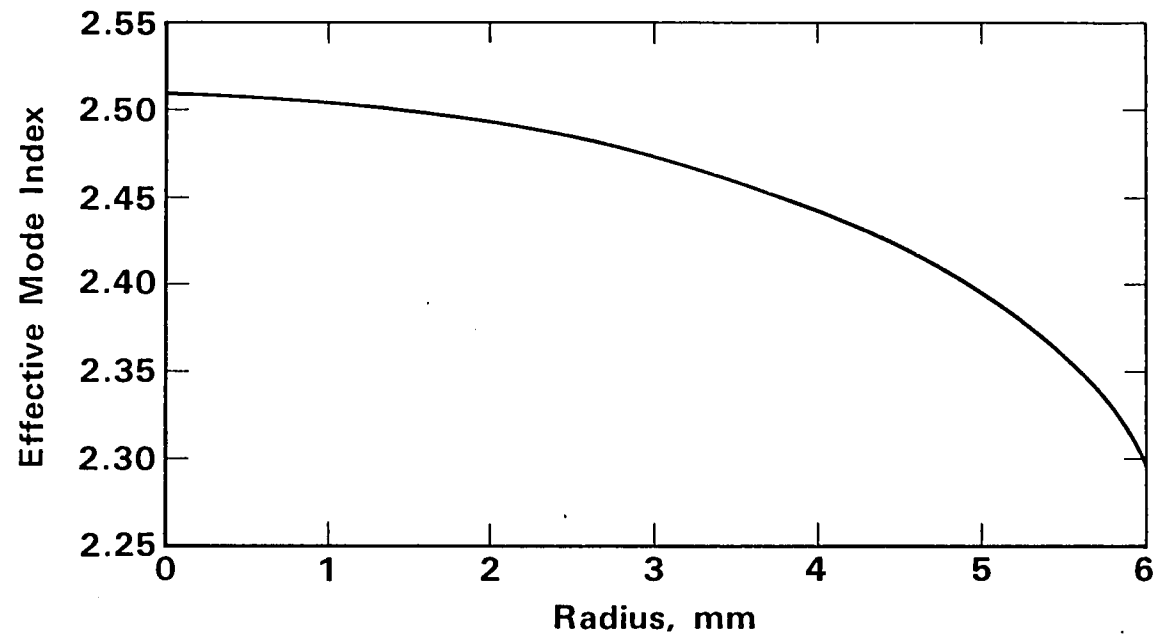


Figure 22. Design mode-index profile for $f/2.1$ Luneburg lens of 10 mm input aperture, designed to focus TM_0 mode of $LiNbO_3:Ti$ waveguide.

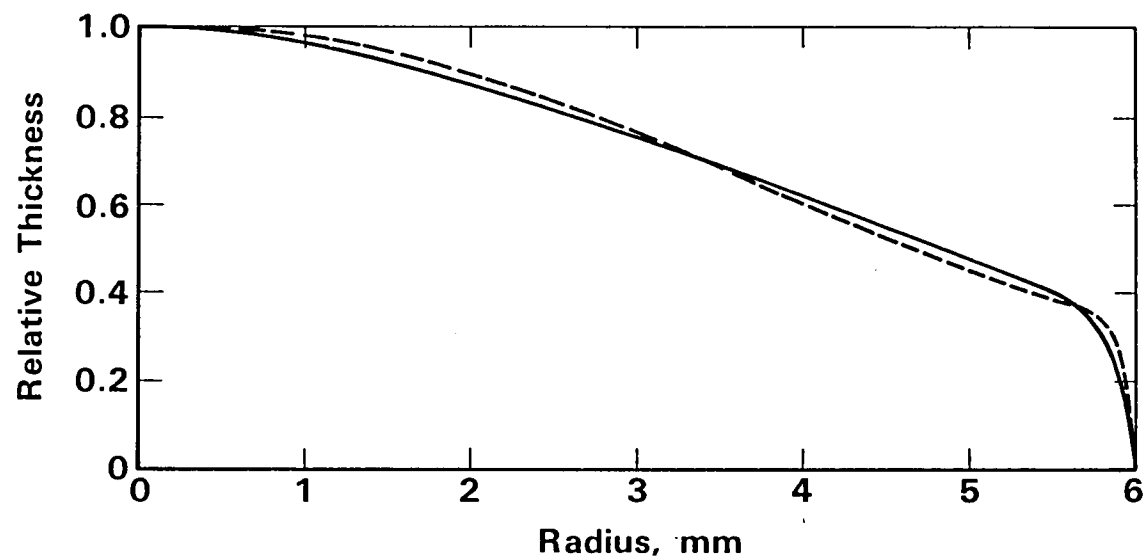


Figure 23. Design lens profile (dashed line) and approximation (solid line) with mask arrangement described in text for example $f/2.1$ Luneburg lens.

with a number of modifications. Since we are dealing with a smaller index difference between the deposited material and the substrate than are those using glass waveguides, it seems we should not need quite as complicated mask arrangements in order to obtain good quality lenses.

The evaporation source is modeled as a uniform distribution, over a circle whose diameter is that of the top of the crucible, of point sources, each of which emits As_2S_3 molecules (or equivalently As_4S_6 molecules⁽³⁴⁾) uniformly into the hemisphere above the source. A Lambertian distribution (weighted by the cosine of the angle from the normal to the source surface) is often⁽³³⁾ assumed instead of a uniform distribution; but since in our system the actual melt surface is well below the assumed source plane, a uniform distribution seems an equally valid assumption. In any event, since the evaporation source is relatively small, only small angles are involved, and the two models are difficult to distinguish.

The sputtering source is similarly modeled as a uniform circular distribution of point sources, now assumed, however, to emit with a Lambertian distribution, as often observed experimentally⁽³⁵⁾, and as usually assumed⁽³¹⁾ in the absence of better information. Yao⁽³¹⁾ assumed a source of infinite extent, but since our sputtering target is relatively small and close to the substrate, we have found it necessary to take its finite size into account.

The particles emitted from the source are assumed to travel in straight lines to the substrate. If a particle hits a mask, it is assumed to be deposited permanently there. The sticking probability at the substrate is taken to be independent of the film thickness and independent of whether the particle condenses on the substrate material or on the film.

We design the mask arrangement to obtain as good as possible an approximation to the relative shape of the deposit, normalized to unity at the center of the lens, and rely on a separate measurement of deposition rate to get the central thickness correctly. The masks for the evaporation work are made of thin sheets of aluminum with holes punched in them. For the sputtering experiments, where space is more limited, we adopted the idea of Zernike⁽³⁶⁾ and Yao and Anderson⁽³²⁾ of making the masks by milling conically tapered segments in aluminum plates.

The relative lens thickness at a point a given radius r from the center may be calculated by integrating the flux arriving at this point from the observable area of the source and dividing by the integrated flux,

similarly calculated, at the lens center. The area of integration in the plane of the source is bounded by arcs of circles which are the projections of the mask segments on this plane and possibly also by the edge of the source. The complexity of determining the boundaries of the integration area for each mask arrangement and each value of r makes evaluating the integrals analytically quite difficult. Consequently we have adopted a numerical procedure, specifically a statistical procedure, the method of equidistributed sequences⁽³⁷⁾. The area of integration is conveniently taken to be a rectangle closely bounding the observable region; unit functions in the integrand are used to reject points within the rectangle but not in the observable region.

An equidistributed sequence of points in the interval $[0,1]$ is defined as an ordered set $\{x_i, i = 1, N\}$ which is determined such that

$$\lim_{N \rightarrow \infty} \frac{1}{N} \sum_{i=1}^N f(x_i) = \int_0^1 f(x) dx \quad (37)$$

for all reasonably well-behaved functions $f(x)$. It can be shown that such a sequence may be generated by taking the decimal parts of successive integral multiples of any irrational number, such as $\sqrt{2}$. Integrals over any finite limits may be evaluated using (37) by appropriate scaling, and multidimensional integrals are easily handled by using an independent sequence for each dimension. Simple numerical tests we have carried out indicate the method of equidistributed sequences is at least five times as fast as a Monte Carlo integration of comparable accuracy. For the present problem, evaluating the integrand at 2000 points proved sufficient to give the integrals to 3 decimal place accuracy with high probability.

To automate the design process somewhat, one mask aperture was allowed to take on a range of values; for each value the calculated lens profile was compared to the design profile at 5 or 10 interior points. A least-squares comparison was used, although a minimax criterion might have been somewhat more useful. The output was examined in detail in all promising cases and further adjustments were made by hand until what appeared to be a satisfactory approximation to the design profile was reached. Experiment and ray-tracing calculations have generally shown that while our designs so far are satisfactory near the center of the lens, they sometimes

fail near the periphery. For the example design we have been discussing, we found after extensive calculation with up to four masks that a simple two-mask arrangement fit the design as well as any. In this arrangement the lower mask has an aperture 12 mm in diameter and is positioned 0.04 mm above the substrate, while the upper mask, with an 8.3 mm aperture, is positioned 4.8 mm above the substrate. We found experimentally that separating the lower mask from the substrate with aluminum foil improved the coupling into the lens. This mask arrangement is easily created by milling an aluminum plate. The calculated profile for this mask arrangement is compared with the design profile in Figure 23. For some other sputtered-lens designs, mask arrangements that taper primarily the other way--that is, opening toward the source--are more suitable, while for evaporated lenses, small apertures 25 to 30 mm below the substrate are required with our experimental arrangement.

11. RAY TRACING

The only way to determine what happens when a Luneburg lens departs from the ideal shape, or varies from the design refractive index, is to trace a sufficient number of rays through the lens to see what happens to the focal spot. We expect, of course, a change in focal length and a decrease in focal spot quality, but these changes have to be evaluated quantitatively in order to determine the tolerances required to meet the specifications of a particular application. Specifically, we can hope to learn from ray tracing

- (1) the adequacy of our lens design procedures
- (2) the adequacy of our mask design procedures
- (3) the degree to which the physical properties--e.g., the film refractive index--of the lenses we have made are sufficiently similar to those assumed in the designs
- (4) the effect of variations in experimental parameters--e.g., the lens central thickness--on the focal spot quality
- (5) some aspects of the overall behavior of Luneburg lenses which may not be intuitively obvious.

Ray tracing thus plays an important role in closing the loop between design and fabrication.

Before discussing some ray-trace work applied to our representative design, we will describe one way in which ray tracing can help improve our understanding of Luneburg lens behavior. We made a series of evaporated lenses with the same mask arrangement, but with different evaporation times, so some lenses had close to the design central thickness while others were considerably thinner. One might naively expect that lenses thinner at the center, with lower mode indices and less steep gradients, would have longer focal lengths than thicker ones, but we found a considerable range over which the thinner lenses had reduced focal lengths. This is illustrated in Figure 24, where experimental points are indicated by circles and the design focal length and thickness are shown at the rightmost "X". The other two X's indicate the results of ray-trace analyses through lenses with the design index profile but reduced thickness. Clearly, the reduced focal lengths are what one should expect under these conditions. Examination of the ray diagrams shows that rays passing through different parts of the lens cross the axis at points which, depending on the lens thickness and the entrance coordinate, may be either in front of or behind the design focal position. Thus, the apparent sharpest focal point depends on the aperture used in a complicated way. The ray-trace also indicates that the lens indicated by the leftmost X in Figure 24 should have a focal spot smaller than the diffraction limit at apertures corresponding to $f/4.8$ or smaller. The sidelobes might not be low--the diffraction pattern was not calculated--but these simple geometrical optics calculations indicate the possibility of obtaining good quality lenses for some purposes with designs that vary markedly from the conventional Luneburg contour.

Now we turn to our design example, which we recall is for a lens to focus a 10 mm wide TM_0 input beam 21 mm from the lens center. First we consider a ray-trace through a lens with the design thickness profile shown in Figure 23. Some representative rays are shown in Figure 25. It is immediately apparent that a good focus, though slightly short of the design focal length, can be obtained at somewhat reduced aperture; but that peripheral rays are not focused well. Both the change in focal length and the long focal length of the peripheral rays are results of not using the correct boundary condition for the TM mode, as discussed earlier. This easily remediable deficiency in the design program has never been corrected since it never led to serious aberrations in earlier designs. Since there is little chance of getting this design to work well at full aperture, we

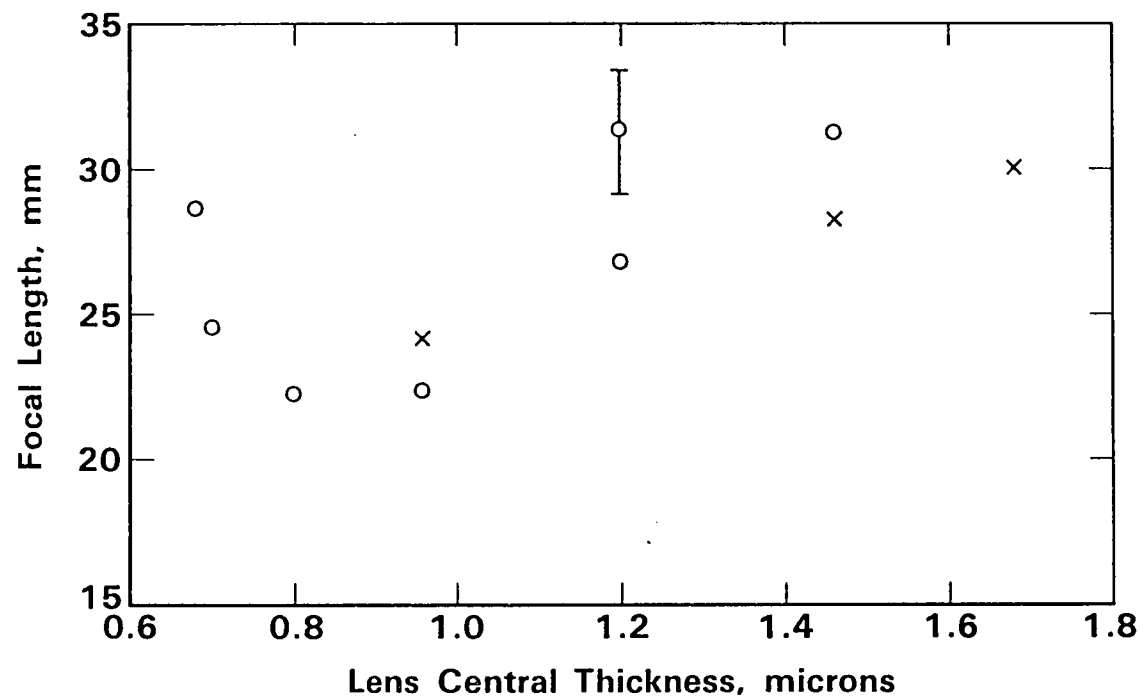


Figure 24. Measured (circles) and calculated (x's) focal lengths for Luneburg lenses of different thicknesses made with the same mask arrangement.

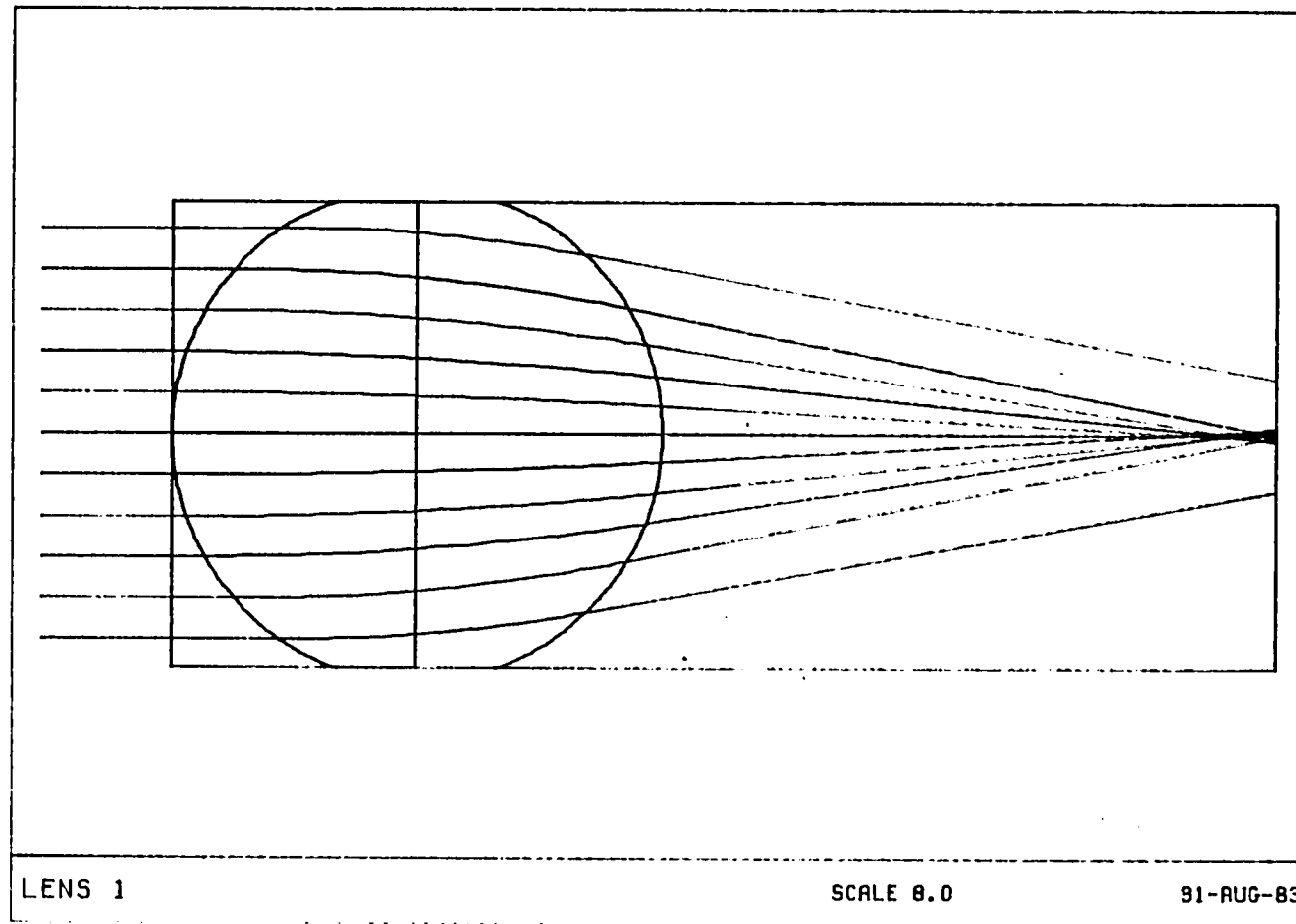


Figure 25. Ray trace through lens with example design thickness profile shown in Figure 23.

will consider its properties at half aperture. The focal length for a 5 mm wide input beam is 19.8 mm and the focal plane diffraction pattern is shown in Figure 26. The graphics have not been changed from those for conventional two-dimensional lenses; a traverse through the center of the plot parallel to either axis is a good approximation to the Luneburg lens focal-plane intensity distribution. The vertical scale is linear. All the diffraction patterns presented in this report should be considered only as qualitative representations, since not enough rays have been traced to obtain a completely accurate quantitative picture. Nonetheless, one can see that at the reduced aperture the lens should focus quite well, with a focal spot size in the range of the diffraction limit.

To investigate the result of a small change in design parameters, let us consider the effect of a reduction in the refractive index of the lens material from 2.58 to 2.573. This amounts to a change of 2.5% in the difference between the film index and the waveguide surface index. A trace of representative rays for this case is shown in Figure 27. The ray plot is quite similar to the previous one, but there are discernible differences. The focal length at 5 mm aperture has increased slightly, to 20.2 mm. The diffraction pattern, Figure 28, at this aperture still has a sharp focal spot, but the sidelobes are increased somewhat. Increasing the lens central thickness from 0.39 to 0.40 μm produced effects of comparable magnitude. The calculated focal length at 5 mm aperture shortened to 19.1 mm and the focus became a little sharper.

In Figure 29, we present a trace of representative rays through a lens with the profile attainable with the mask design described in the previous section. The lens shows a fairly sharp focus at apertures up to 6 mm, but peripheral rays are again only weakly focused. The focal length at 5 mm aperture is reduced to 18.3 mm. The variation of focal length with small changes in lens shape is large enough that it appears that in applications such as collimation where precise focal length control is important, it is highly desirable to have a means of adjusting the focal length after fabrication. The focal-plane diffraction pattern for this lens, Figure 30, shows that the central focal spot remains fairly sharp, but the sidelobes are considerably increased.

All the ray tracing work described here was done by Professor Duncan T. Moore and C. Benjamin Wooley at the University of Rochester Institute of Optics under subcontract to Professor Moore's firm, Gradient Lens Corporation.

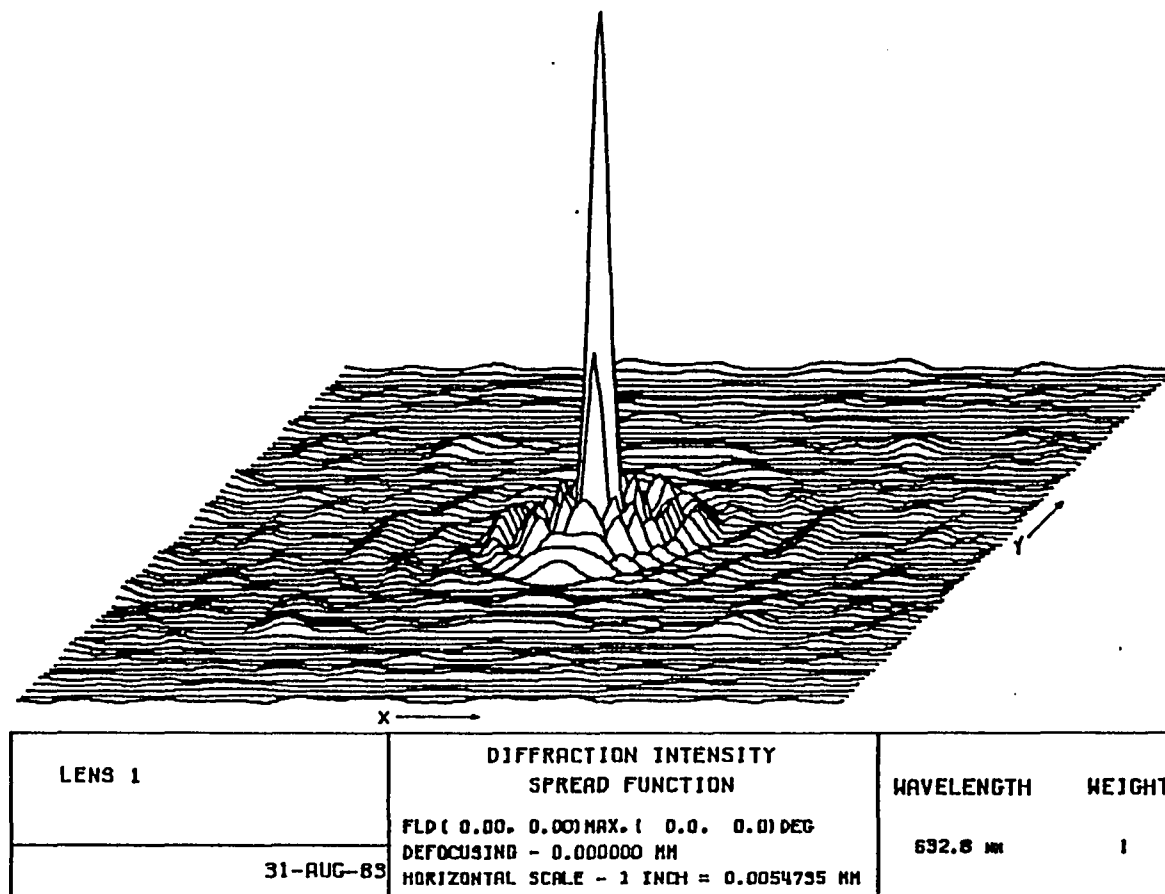


Figure 26. Focal-plane diffraction pattern for lens ray-traced in Figure 25. The diffraction pattern for a Luneburg lens is given approximately by a section parallel to a coordinate axis.

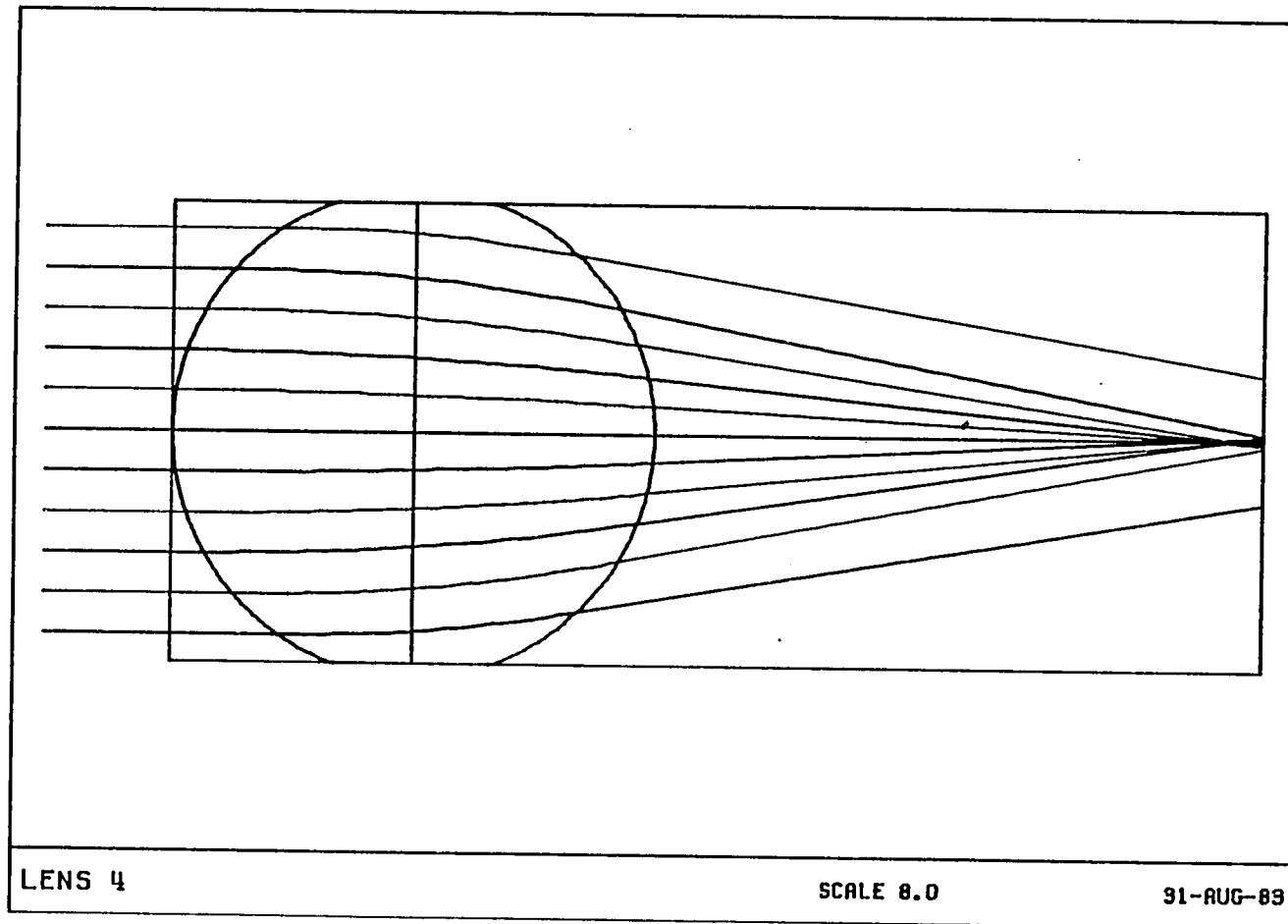


Figure 27. Ray trace through a lens similar to that in Figure 25, but with reduced film refractive index.

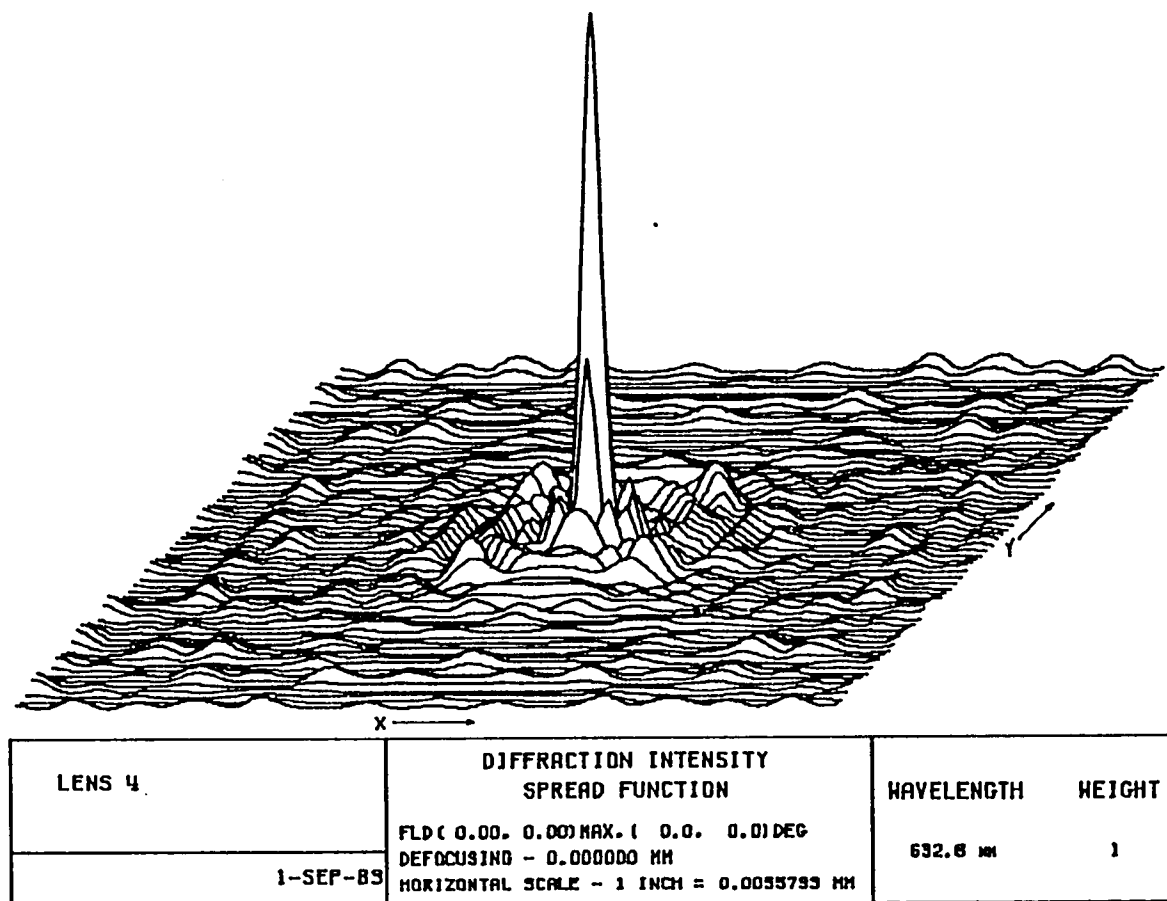


Figure 28. Focal plane diffraction pattern for lens ray-traced in Figure 27.

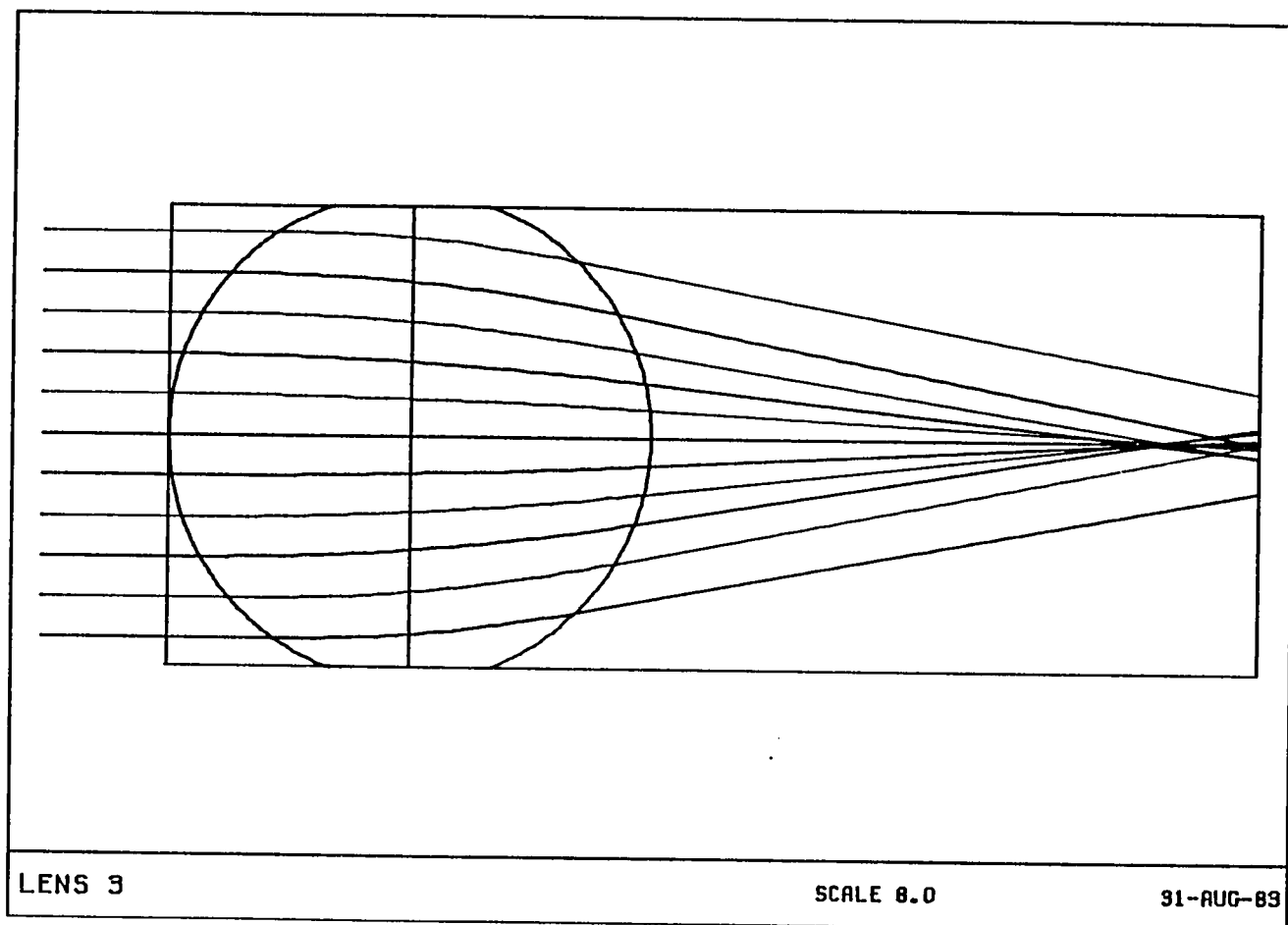
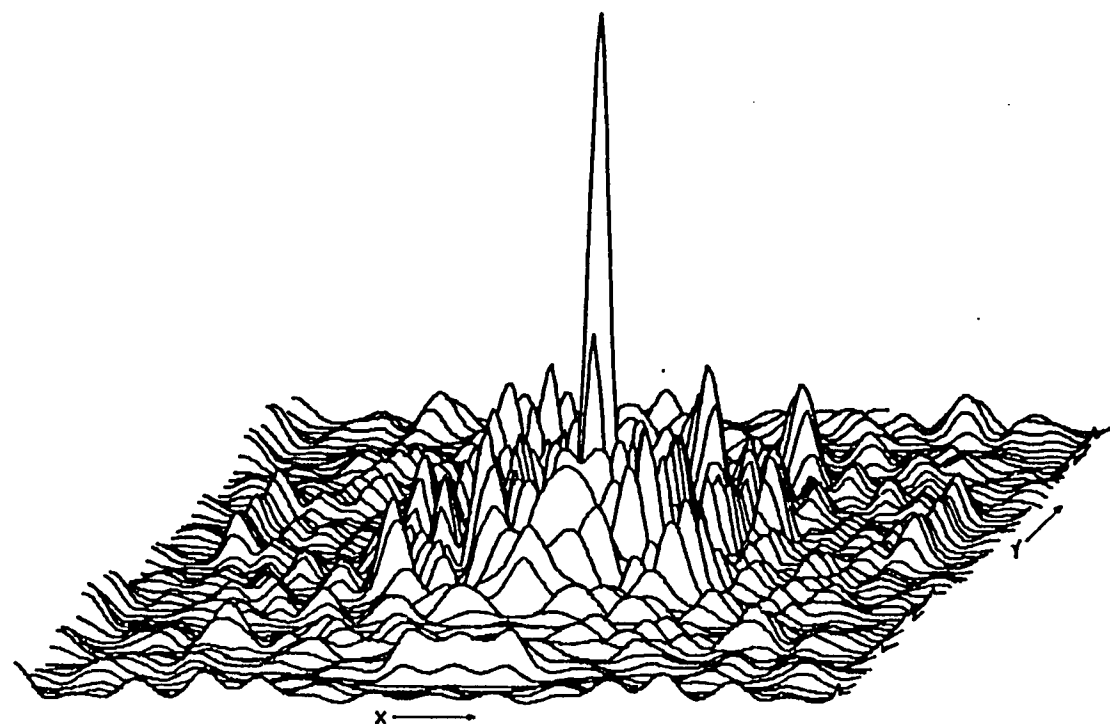


Figure 29. Ray trace through a lens with profile, shown in Figure 23, attainable with simple mask arrangement.



LENS 3	DIFFRACTION INTENSITY SPREAD FUNCTION	WAVELENGTH	HEIGHT
		632.6 NM	1
31-AUG-89	FLD(0.00, 0.00) MAX. (0.0, 0.0) DEG DEFOCUSING - 0.000000 MM HORIZONTAL SCALE - 1 INCH = 0.0050865 MM		

Figure 30. Focal plane diffraction pattern for lens ray-traced in Figure 29.

12. LENS FABRICATION AND TESTING

Numerous lenses have been made and tested. The fabrication procedures have already been described. We frequently departed in one respect or another from the nominal design procedures in order to investigate experimentally effects of variations in material and process parameters such as were investigated theoretically in the previous section.

The principal experimental data obtained on the lenses were the focal length and, in relatively good lenses, the focal spot quality. In most cases the lenses focus outside the waveguide. To determine the focal length, we measure the length of the optical path in each medium--waveguide, output coupling prism if used, and air--from the lens center to the focal point, and convert the total distance to an equivalent distance inside the waveguide. The accuracy of this procedure is not very high; our quoted focal lengths might easily be in error by $\pm 10\%$.

Our primary method for characterizing the optical quality of the Luneburg lenses is the examination of the light distribution in the focal plane. The focal spot is scanned by coupling the beam transmitted through the lens out through a rutile prism and refocusing it with an $f/2$ imaging lens onto an optical multichannel analyzer (OMA). The experimental arrangement is shown in Figure 31. The OMA has 500 $25\text{ }\mu\text{m}$ channels on $25\text{ }\mu\text{m}$ centers. The channels are long enough to collect substantially all the light diffracted or scattered in the direction perpendicular to the waveguide plane. The OMA output can be displayed on an oscilloscope screen or recorded digitally. In some instances, a Reticon diode array has been used instead of the OMA.

OMA scans of the lens focal spots have generally been made at reduced input aperture in order to be sure that all the light transmitted is captured by the relay lens and focused on the OMA detector. The diffraction patterns do not sharpen markedly at larger apertures, but we cannot presently say how much of this effect results from poorer quality of the lens near the periphery and how much from aperture effects in the light-collection system. The focal spot quality does not vary in any marked or predictable way with lens thickness. The spot quality data may be evaluated by noting that for 5 mm aperture and 21 mm focal length, the half-power diffraction-limited spot size for the TM_0 mode at 633 nm is $2.3\text{ }\mu\text{m}$. For an ideal lens, the first sidelobes should be 13.3 dB down in

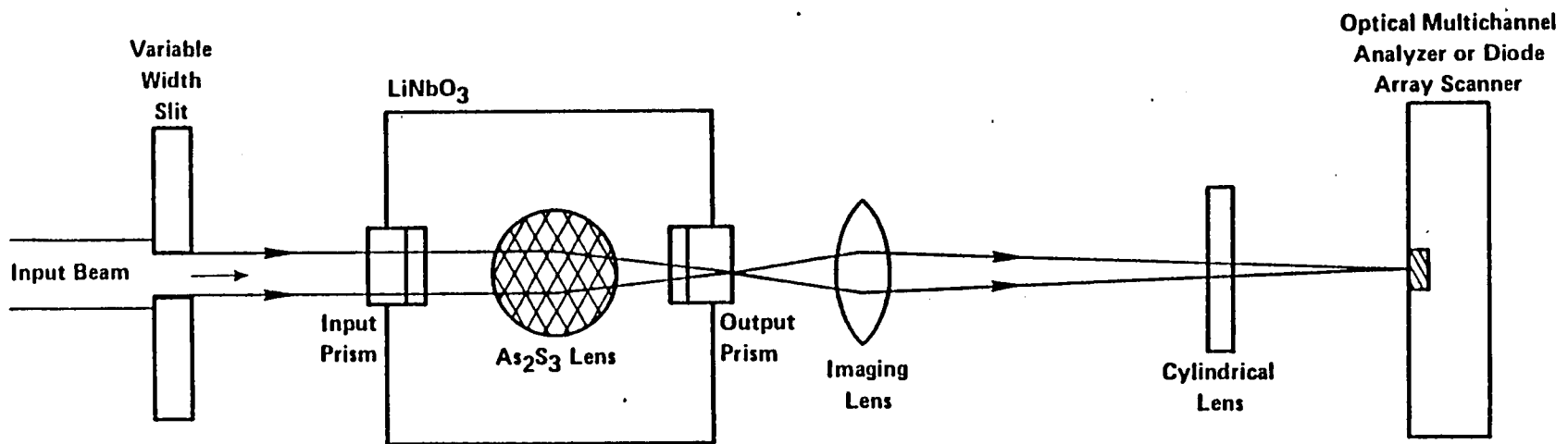


Figure 31. Experimental arrangement for observation of Luneburg lens focal plane characteristics.

intensity from the central peak. These two numbers, focal spot size and first-sidelobe intensity, do not fully characterize the lens quality, of course, even at fixed input aperture. It should also be borne in mind that the input beam is a truncated Gaussian rather than an ideal plane wave.

From among our results on evaporated lenses, we will present representative data on just two, one tested as made and the other exposed to ultraviolet light to increase its refractive index. Additional details on a number of evaporated lenses are provided in our previous year's report⁽³⁸⁾. These lenses were again 12 mm in diameter; they were formed by evaporating arsenic trisulfide through a mask with a 5.0 mm diameter aperture held 28 mm below the waveguide and an 11.9 mm aperture edge-defining mask placed 0.5 mm from the guide. The design is intended to focus a 10 mm wide TM_0 beam at a distance of 30 mm from the center of the as-prepared lens.

A Reticon diode array scan--25 μm detectors on 50 μm centers--for one as-prepared lens is shown in Figure 32. This lens is 0.70 μm thick, compared to a nominal design value of 1.69 μm . It has a measured focal length of 25 mm at 10 mm aperture. In the scan, which was made at 4 mm aperture, the central spot is 2.3 μm wide, compared with a diffraction-limited value of 1.5 μm at this aperture, and the first sidelobes are 11 dB down. This represents one of our better as-prepared lenses. The marked difference in thickness from the design value seems to have little effect on the focal spot quality, although it does affect the focal length. The ray-tracing work, though, indicates that often even when the focal spot is sharp, the phase deviations in the focal plane are of far from standard form. This effect, a form of the phenomenon referred to⁽³⁹⁾ as "spurious resolution", can have serious consequences if the lens is to be used for optical data processing.

The Reticon scan shown in Figure 33 is for a lens which was exposed to ultraviolet light until its refractive index was increased to around 2.58. This lens is 1.2 μm thick and has a focal length of 18 mm. The focal spot is 2.9 μm wide, or 2.7 times the diffraction limit, and the first sidelobes are more than 13 dB down. As with altering the thickness of the as-prepared lenses from the design value, increasing the film refractive index changes the focal length without changing the focal-spot characteristics as markedly as one might expect. The same remarks about phase deviations apply.

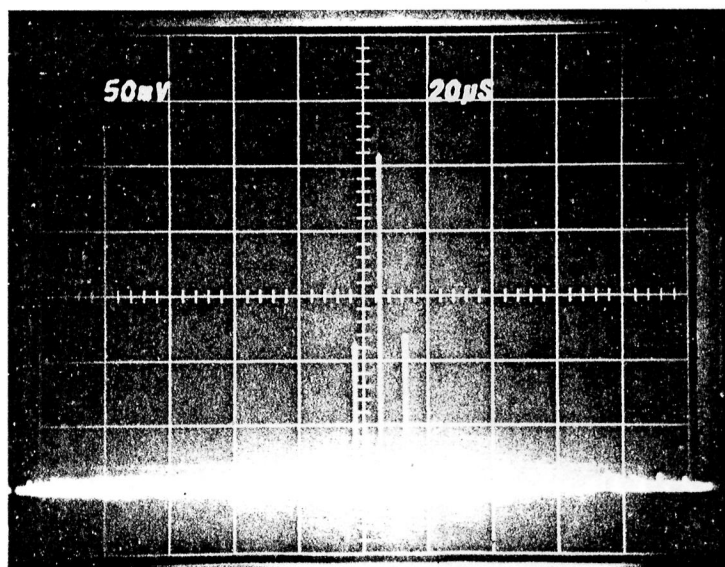


Figure 32. Diode-array scan of focal plane of as-prepared evaporated lens.

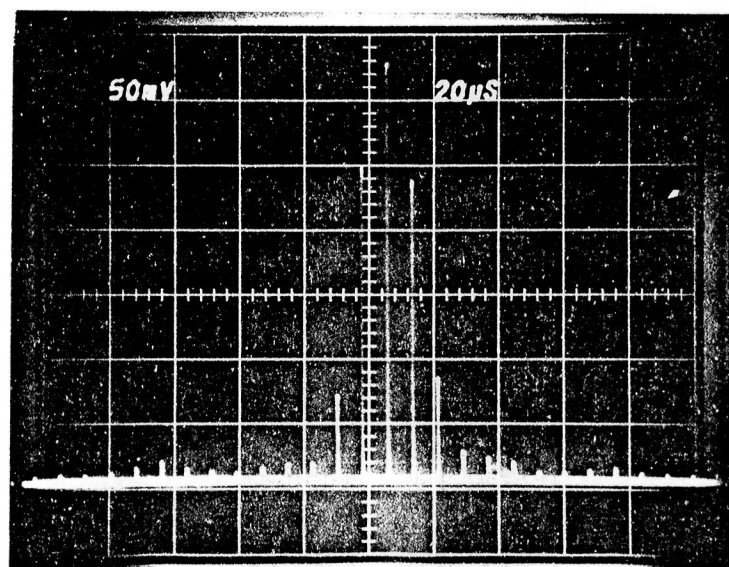


Figure 33. Diode-array scan of focal plane of evaporated lens exposed to ultraviolet light.

Luneburg lenses need not be circular in shape as viewed from above (40). We prepared by evaporation some As_2S_3 lenses of more nearly rectangular shape and measured their characteristics. Our work in this area is described in our paper "Rectangular Luneburg-type Lenses for Integrated Optics", item 3 in Appendix D. This paper and item 1 in that list also contain additional data on focal plane scans.

Only preliminary tests of information handling capacity of the lenses have been made. In one experiment, the lens was deposited on a large substrate and broad-band transducers were arranged to generate surface acoustic waves in the lens input plane. The SAW frequency was swept from 280 to 410 MHz and a digital word generator was used to sample periodic portions of this range. For example, "on" segments 6.2 MHz wide separated by 6.2 MHz "offs" were readily resolved photographically. Rays to the centers of adjacent "on" segments have an angular separation of about 0.5 mrad. The spatial frequencies are separated by about 0.5 μm . The ultimate resolution is clearly higher, but unfortunately this lens was accidentally destroyed before testing could be completed. These results, while encouraging, should not be weighed too heavily in view of the known phase aberrations in many of our lenses.

Initial experiments on sputtered lenses were also encouraging. These experiments were started before designs for the masks were completed, so a variety of masks were made on the basis of rough guesses about useful shapes and tried out. Masks with a single conical taper, similar to those used by Zernike (36), and masks with a double conical taper, like those described by Yao and Anderson (31), were both used, as was a mask with a conical plus a cylindrical section. The mask apertures were made by drilling through 4.8 mm (3/16") thick aluminum sheet. In all these masks, the aperture was 6.75 mm in diameter at its narrowest point. The lenses are approximately 11 mm in diameter and either 0.5 or 0.6 μm thick at the center. While all the lenses focused 633 nm guided light to some extent those made with the single conical masks had relatively diffuse focal spots. One lens made with a double-cone mask and 0.6 μm thick had a focal length of 25 mm inside the waveguide. A 0.6 μm thick lens made with a cylinder-plus-cone mask also had a 25 mm focal length. The lens deposits appeared to be of good quality.

After the sputtering system had been in operation for some time, though, the quality of the lenses deteriorated markedly. The difficulties, which appeared in lenses of all sizes and shapes, may be summarized by

saying that thicker lens deposits tended to absorb or scatter the incident light very strongly, so no output beam could be detected, while thinner deposits did not refract as strongly as expected, focal lengths referred to the waveguide material being 60 mm or more. Varying the sputtering conditions, replacing masks and shutters, using high-purity argon instead of standard laboratory grade, and cleaning and overhauling the system had no effect. Presputtering for 1 to 2 hours seemed to help somewhat as did raising the mask slightly above the waveguide as we have previously described. Microscopic examination of some of these later films showed scattered platelets a few micrometers in diameter adhering to the surface but similar-looking platelets observed on some evaporated films did not affect their properties markedly. This problem is unresolved at this writing, but chemical analyses, to be described shortly, have provided some helpful diagnostic information. Thus while we anticipated sputtering would be a more controllable and reproducible process than evaporation for fabricating the lenses, it has not so far proven to be so.

13. CHEMICAL ANALYSES

In view of the differences between evaporated and sputtered films, and between "early" and "late" sputtered films, it seemed worthwhile to investigate the chemical nature of the films and of the raw materials from which they were made. The primary analytical technique employed was ESCA (electron spectroscopy for chemical analysis), since this method provides information on bonding, and thus enables one to determine what compounds, as well as what elements, are present. The film samples were uniform layers in the 0.4 to 1.0 μm thickness range, deposited on glass slides which could be cut to the approximate size for insertion into the ESCA apparatus. Examination of the films under magnification showed small platelets adhering to some areas of the sputtered films, particularly the more recently prepared films. The evaporated film had fewer such features. Robinson back-scatter electron micrographs of the films also showed numerous surface features, appearing at 500X like little balls, on the sputtered films. It could not be ascertained whether these were the same features observed visually, but it is suspected they are similar because they show similar tendencies to follow polishing marks and other such

imperfections in the underlying glass plate. The electron micrographs did not reveal whether the surface features were of different composition from the substrate, but ESCA experiments with the angle of the incident X-ray beam increased from 45 to 63° showed no significant changes in composition, indicating that these features probably have a composition similar to the bulk. One drawback of ESCA is that it provides information on the composition only of the top 3 nm of the sample, so other techniques are necessary if there is any reason to believe the composition may not be uniform through the sample. Also ESCA looks at the whole sample surface, and is not suited for studying variations from point to point on the surface.

All the samples are very pure. The only contaminants detected were minor amounts of surface organics. In particular, there is no evidence of As_2O_3 or As_4S_4 molecules. ESCA data do not seem to be available for As_2S_5 , the other stoichiometric compound of arsenic and sulfur, but as there are no unidentified peaks, the likelihood of this material being present is small. These other compounds could be detected, if present, at a level of a few percent. Thus all the materials appear to have exclusively As_2S_3 -type bonding at the local level. Integration of the areas under the peaks shows, though, that they are all more or less sulfur-rich, as Table 2 (on the following page) indicates. The relative amounts of the constituents are presented in two ways: as the fractional amount x of As in material $\text{As}_x\text{S}_{1-x}$ and as the amount y of S in materials of formula As_2S_y . Thus for pure As_2S_3 glass, x should equal 0.40 and y should equal 3. The uncertainty in the values of x is around ± 0.03 , while the possible error in y is quite large, ranging from 0.5 to 1.7. There appear to be significant differences between the compositions of the films and those of the corresponding sources, as well as differences in the films themselves. To see whether a change in target composition as the material is used up might play some role in the difference in sputtering results, we made an electron microprobe traverse across a freshly broken face of this sample. A similar traverse was made across a face of glass used as the evaporation source. Both samples showed considerably less sulfur in the interior than at the surface. The content seemed to vary smoothly through the samples. We have not attempted quantitative analysis of this data because previous attempts to perform such calculations for microprobe measurements on evaporated films did not appear to yield reliable results. Qualitatively, we can say that the sputtering source is slightly more sulfur-rich near the surface than the glass raw material

Table 2. Composition of Bulk and Film Samples of Arsenic Trisulfide Glass as Indicated by ESCA.

Sample	$\text{As}_x \text{S}_{1-x}$	$\text{As}_2 \text{S}_y$
	x	y
Glass, evaporated source	.338	3.9
Glass, sputter-etched 10 minutes to remove carbon	.350	3.7
Evaporated film	.280	5.1
Unused piece of a sputtering target	.204	7.8
Sputtered film, early	.226	6.8
Sputtered film, late	.330	4.1

for evaporation, while near the center of the samples tested the evaporation source was more sulfur-rich. We might speculate that the molten evaporation source has a composition close to As_2S_3 , variations in composition in evaporated films then resulting from decomposition during evaporation. Changes in sputtered films, on the other hand, might reflect changes in the composition of the exposed surfaces of the target. Clearly, though, considerable additional work is necessary if these ideas are to be verified or otherwise.

The analytical work described in this section was performed by Julius Ogden, Doyle Kohler and Carl A. Alexander of the Battelle-Columbus Physico-Chemical Systems Section.

14. DISCUSSION AND CONCLUSIONS

In the first part of this program, we were able to show that short-focal-length Luneburg lenses of good quality could be produced by depositing arsenic trisulfide films on LiNbO_3 waveguides. One principal difficulty was with variability of the properties, particularly the refractive index, of evaporated films. This was one reason for trying sputtering as a possible alternative deposition procedure. Sputtered films to date, though, have shown a larger range of properties, and have been more difficult to control, than have evaporated ones. We have suggested, on the basis of limited chemical analyses, that inhomogeneity in the material forming the sputtering target may be responsible. This suggestion is at present very speculative, of course.

Improvements have been made in the remainder of the design and fabrication procedure, so if reliable film deposition procedures are developed, it should require primarily some process refinement to permit production of useful lenses on a regular basis.

Reliability and reproducibility of the lens production process can only be defined, though, with respect to some particular design objective. It is a good general objective to aim, as we have done, at fabrication of large diameter, short focal length, diffraction-limited lenses, but it is more appropriate in a particular case to investigate how the deviations from the nominal design which are likely to occur affect the lens performance in its designed role. It is important to bear in mind that the point sources and plane waves of conventional design are idealizations which are seldom appropriate for contemporary integrated optics devices.

Our present judgment is that the most reliable way of making arsenic trisulfide thin-film lenses is thermal evaporation followed by annealing in an inert atmosphere⁽²⁵⁾. This opinion is based on only a few experiments, though, and considerable additional experimental work including more chemical analysis would be desirable. Surprisingly little analysis of arsenic trisulfide films has been done anywhere.

As far as improvements in the remainder of the design and fabrication process go, the primary requirement is closer integration of the ray-tracing work into the design and fabrication process. Ray tracing has provided valuable information, but it has not always been obtained at the most suitable times, mainly through failure to recognize how helpful it was going to be. Other design improvements are in the nature of refinements. We have mentioned difficulties in some lenses with focus of peripheral rays, passing through the thinnest part of the lens. These problems can be alleviated by designing for still larger lens diameters and using only the central portion of the lens. If space on the substrate becomes a problem, rectangular- or lenticular-outline lenses can be used. Tolerance requirements for these large lenses remain to be investigated, though.

In testing of the lenses, the only improvement that may be needed is in the profilometry of the lens shape. In situations where close tolerances must be maintained, uncertainty concerning curvature of the substrate below the lens makes sufficiently accurate measurement difficult. While there are a number of things that can be done, there is no easy way around this problem.

If a good film deposition process is developed, these other design and process refinements should permit the fabrication of arsenic trisulfide lenses suitable for many beam-forming and signal-processing requirements.

IV. REFERENCES

1. H. Engan, "Excitation of Elastic Surface Waves by Spatial Harmonics of Interdigital Transducers", IEEE Trans. Electron Devices ED-16, 1014 (1969).
2. H. Kogelnik, "Coupled Wave Theory for Thick Hologram Gratings", Bell Syst. Tech. J. 48, 2909 (1969).
3. H. T. Kung, "Why Systolic Architectures?", Computer 15, 37 (1982).
4. T. Suhara, H. Nishihara and J. Koyama, "High-Efficiency Relief-Type Waveguide Hologram", Trans. IECE Japan E61, 167 (1978).
5. T. Kurokawa and S. Oikawa, "Optical Waveguide Intersections Without Light Leak", Appl. Opt. 16, 1033 (1977); H. Nakajima, T. Horimatsu, M. Seino and I. Sawaki, "Crosstalk Characteristics of Ti-LiNbO₃ Intersecting Waveguides and Their Application as TE/TM Mode Splitters", IEEE J. Quantum Electr. QE-18, 771 (1982).
6. H. J. Caulfield, W. T. Rhodes, M. J. Foster and Sam Horvitz, "Optical Implementation of Systolic Array Processing", Opt. Comm. 40, 86 (1981).
7. P. Tamura, Private communication.
8. C. M. Verber and R. P. Kenan, "Integrated Optical Circuits for Numerical Computation", SPIE Technical Symposium East '83, Arlington, VA, SPIE 408-10, April, 1983. Also presented at 10th International Optical Computing Conference (IOCC), MIT, Cambridge, MA, April, 1983.
9. J. W. Goodman, A. R. Dias and I. M. Woody, "Fully-Parallel, High-Speed Incoherent Optical Method for Performing Discrete Fourier Transforms", Opt. Lett. 2, 1 (1978).
10. J. W. Goodman, A. R. Dias, K. M. Johnson and D. Pere, "Parallel Incoherent Optical Matrix-Vector Multipliers", Presented at Workshop on Optical Signal Processing, Lubbock, Texas, pp 116-128 (1980).
11. W. L. Brogan, Modern Control Theory (Quantum Publishers, Inc., Orange CT 1974) p. 28.
12. S. L. Fagin, "Feedback Realization of a Continuous-Time Optimal Filter", IEEE Trans. Aero. and Electron Syst. AES-3, 494 (1967).
13. H. J. Caulfield, C. M. Verber and R. L. Stermer, "Solving Large Matrix Problems with Intermediate Sized Optical Processors", Presented at the Optical Information Processing Conference II, August 30-31, 1983, Hampton, Virginia. (NASA CP to be published).
14. D. Casasent, J. Jackson and C. Neumann, "Frequency-Multiplexed and Pipelined Iterative Optical Systolic Array Processors", Appl. Opt. 22, 115 (1983).

15. R. P. Bocker, H. J. Caulfield and K. Bromley, "Rapid Unbiased Bipolar Incoherent Calculator Cube", Appl. Opt. 22, 804 (1983).
16. J. Gruninger and H. J. Caulfield, "Algorithm Improvements for Optical Eigenfunction Computers", Appl. Opt. 22, 2075 (1983).
17. A. Ralston, A First Course In Numerical Analysis, (McGraw Hill, NY 1965).
18. H. Onodera, I. Awai and J. Ikenoue, "Refractive-index Measurement of Bulk Materials: Prism Coupling Method", Appl. Opt. 22, 1194 (1983).
19. J. G. Berman, A. Ashkin, A. A. Ballman, J. M. Dziedzic, H. J. Levinstein and R. G. Smith, "Curie Temperature, Birefringence, and Phase-matching Variations in LiNbO_3 as a Function of Melt Stoichiometry", Appl. Phys. Lett. 12, 92 (1968).
20. G. B. Hocker and W. K. Burns, "Modes in Diffused Optical Waveguides of Arbitrary Index Profile", IEEE J. Quantum Electron. QE-11, 270 (1975).
21. R. K. Watts, M. de Wit and W. C. Holton, "Nonoxide Chalcogenide Glass Films for Integrated Optics", App. Opt. 13, 2329 (1974).
22. S. A. Keneman, "Hologram Storage in Arsenic Trisulfide Thin Films", App. Phys. Lett. 19, 205 (1971).
23. K. Tanaka, "Optical Properties and Photoinduced Changes in Amorphous As-S Films", Thin Solid Films 66, 271 (1980).
24. S. A. Keneman, J. Bordogna and J. N. Zemel, "Evaporated Films of Arsenic Trisulfide: Dependence of Optical Properties on Light Exposure and Heat Cycling", J. Opt. Soc. Am. 68, 32 (1978).
25. G. Stewart, R. H. Hutchins and P. J. R. Laybourn, "Controlled Growth of Arsenic Trisulphide Films for Coupling Integrated Optical Devices", J. Phys. D 14, 323 (1981).
26. S. P. Morgan, "General Solution of the Luneburg Lens Problem", J. Appl. Phys. 29, 1358 (1958).
27. W. H. Southwell, "Index Profiles for Generalized Luneburg Lenses and Their Use in Planar Optical Waveguides", J. Opt. Soc. Amer. 67, 1010 (1977).
28. W. H. Southwell, "Inhomogeneous Optical Waveguide Lens Analysis", J. Opt. Soc. Amer. 67, 1004 (1977).
29. D. A. Bryan, C. R. Chubb, J. K. Powers, H. E. Tomaschke, W. R. Reed and E. A. Dalke, "Development of the Tantalum Pentoxide Luneburg Lens", Proc. SPIE 321, Integrated Optics II, p. 2 (1982).

30. S. K. Yao, "Theoretical Model of Thin-film Deposition Profile with Shadow Effect", J. App. Phys. 50, 3390 (1979).
31. S. K. Yao and D. B. Anderson, "Shadow Sputtered Diffraction-limited Waveguide Luneburg Lenses", Appl. Phys. Lett. 33, 307 (1978).
32. S. K. Yao, D. B. Anderson, R. R. August, B. R. Youmans, and C. M. Oania, "Guided-wave Optical Thin-film Luneburg Lenses: Fabrication Technique and Properties", App. Opt. 18, 4067 (1979).
33. G. Hatakoshi, H. Inoue, K. Naito, S. Umegaki and S. Tanaka, "Optical Waveguide Lenses", Optica Acta 26, 961 (1979).
34. J. P. de Neufville, S. C. Moss and S. R. Ovshinsky, "Photostructural Transformations in Amorphous As₂Se₃ and As₂S₃ Films", J. Non-Cryst. Solids 13, 191 (1974).
35. L. I. Maissel and R. Glang, eds., Handbook of Thin Film Technology (McGraw-Hill Book Co., New York, 1970), p. 3-24.
36. F. Zernike, "Luneburg Lens for Optical Waveguide Use", Opt. Commun. 12, 379 (1974).
37. P. J. Davis and P. Rabinowitz, Numerical Integration (Blaisdell, Waltham MA, 1967), p. 150.
38. V. E. Wood, J. R. Busch and C. M. Verber, NASA Contractor Report 165972, "Design, Fabrication and Evaluation of Chalcogenide Glass Luneburg Lenses for LiNbO₃ Integrated Optical Devices", (Battelle Columbus Laboratories, 1982).
39. L. Levi, Applied Optics, v. 1 (John Wiley & Sons, New York, 1968), p. 449.
40. W. H. Southwell, "Planar Optical Waveguide Lens Design", Appl. Opt. 21, 1985 (1982).

V. APPENDICES

APPENDIX A

THE NONLINEARITY PROBLEM

APPENDIX A

THE NONLINEARITY PROBLEM

A major problem with most components available for analog optical computation is that they are not linear devices. Thus, if we have a signal voltage V_S , applied to most common optical modulators the output light intensity will typically be

$$I = I_0 \sin^2 a V_S \quad (1A)$$

where I_0 is the incident intensity and a is a constant characteristic of the modulator. In most cases we would, of course, prefer that the output be

$$I = \text{const} \times V. \quad (2A)$$

There are a number of approaches to achieving this end. The most desirable is to develop a linear modulator. We understand that there are some promising developments along these lines, but we are unable to comment further at this time. Other approaches are signal preconditioning, modified detection schemes and operating in a binary mode.

Each of the three approaches to overcoming the intrinsic nonlinearity for the electrooptic grating modulator is discussed in this Appendix. Signal preconditioning is an analog method which is best applied to slowly-varying signals. In the case of the fully-parallel matrix-vector multiplier, in which the vector components are rapidly-changing data and the matrix elements represent a slowly-varying set of system equations, it would be natural to handle the matrix elements with the analog signal preconditioning technique.

The modified detection scheme involves frequency-shifting one of two optical beams whose intensities are to be multiplied. The multiplication takes place on a square-law detector and takes advantage of its properties to extract the desired product. Matrix multiplication architectures using this technique have not yet been devised.

Operation in a binary mode involves using one side of the herringbone electrode structure as an (electrical) digital-to-(optical) analog converter. The optical analog signal is then modulated (multiplied) by the

second half of the herringbone. This approach results in a reduction in the size matrix which a given IOC can handle since an N-bit (E)D/(O)A converter requires N IOSLM elements. However, the ability to accept a direct N-bit parallel input is a significant advantage.

Signal Preconditioning

Assume a modulator M where transmission T varies in a nonlinear way with the applied voltage V, so that, for example

$$T = \sin^2(aV). \quad (3A)$$

To set T to some desired value x, $0 \leq x \leq 1$, we must apply the voltage

$$V(x) = (\sin^{-1}\sqrt{x})/a \quad (4A)$$

This voltage can be generated using the circuit shown in Figure 1A. We use an electrooptic modulator, M to "model" the real modulator. Applying V yields IT. The detected signal, βT , is proportional to T with a readily measurable proportionality constant, β . A comparator between βT and βX drives the circuit through feedback to

$$T - \beta X = 0. \quad (5A)$$

When this condition obtains,

$$V = V(x) \quad (6A)$$

is available for use. The "decay" from the initial V, say $V = \pi/2a$ for which $T = 1$, is exponential with the time constant limited only by comparator speed. A time delay must be built in so that only the steady state V is applied to the modulator we wish to control. It remains to be seen if such an approach is sufficiently rapid to justify its use.

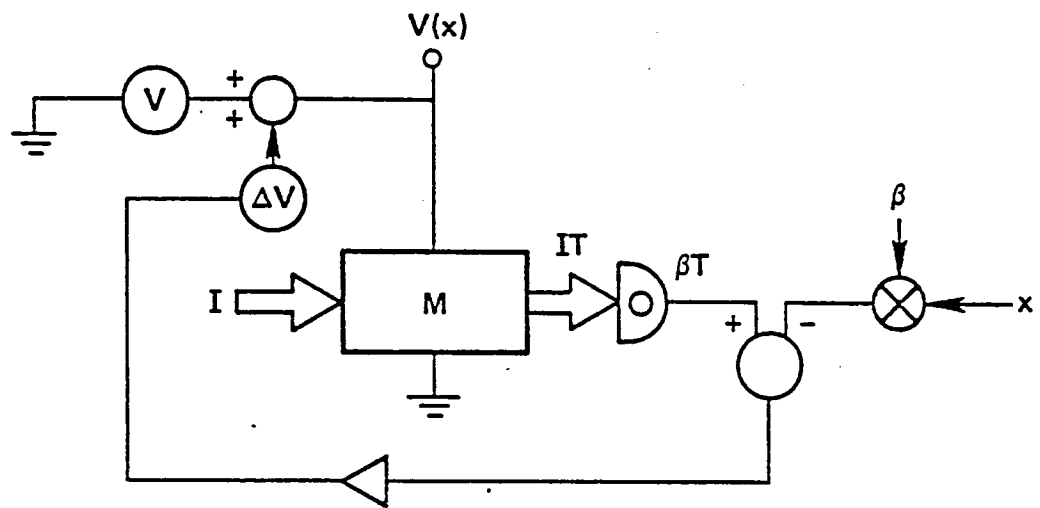


Figure 1A. Circuit for generating $V(x) = (\sin^{-1}\sqrt{x})/a$.

An Optical Method for Linear Analog Multiplication

Assume again that the modulators generate the output given by Eq. (1A). We will show that, by introducing an appropriate modulation signal we can extract an electrical signal proportional to V_1V_2 .

Consider the outputs of two modulators

$$\begin{aligned} I_1 &= I_0 \sin^2 aV_1 \\ I_2 &= I_0 \sin^2 aV_2 \end{aligned} \quad (7A)$$

If $aV_1, aV_2 \ll 1$, then the output intensities and the corresponding amplitudes are

$$\begin{aligned} I_1 &= (aV_1)^2 I_0 ; \quad A_1 = aV_1 A_0 e^{i(w+\delta)t} \\ I_2 &= (aV_2)^2 I_0 ; \quad A_2 = aV_2 A_0 e^{iwt} \end{aligned} \quad (8A)$$

where w is the optical frequency and δ is an r.f. frequency shift imposed on one of the beams.

If the two beams are now combined on a square-law detector, the resulting signal is

$$\begin{aligned} S &= \text{const} \times A_1 e^{i(w+\delta)t} + A_2 e^{iwt}^2 \\ &= A_1^2 + A_2^2 + A_1 A_2 \cos \delta t \\ &= \text{D.C. term} + a^2 V_1 V_2 I_0 \cos \delta t. \end{aligned} \quad (9A)$$

Therefore by detecting the A.C. term we get a signal which is linearly proportional to V_1V_2 .

A method for accomplishing this is shown in Figure 2A. This can be implemented either in bulk or integrated optical form.

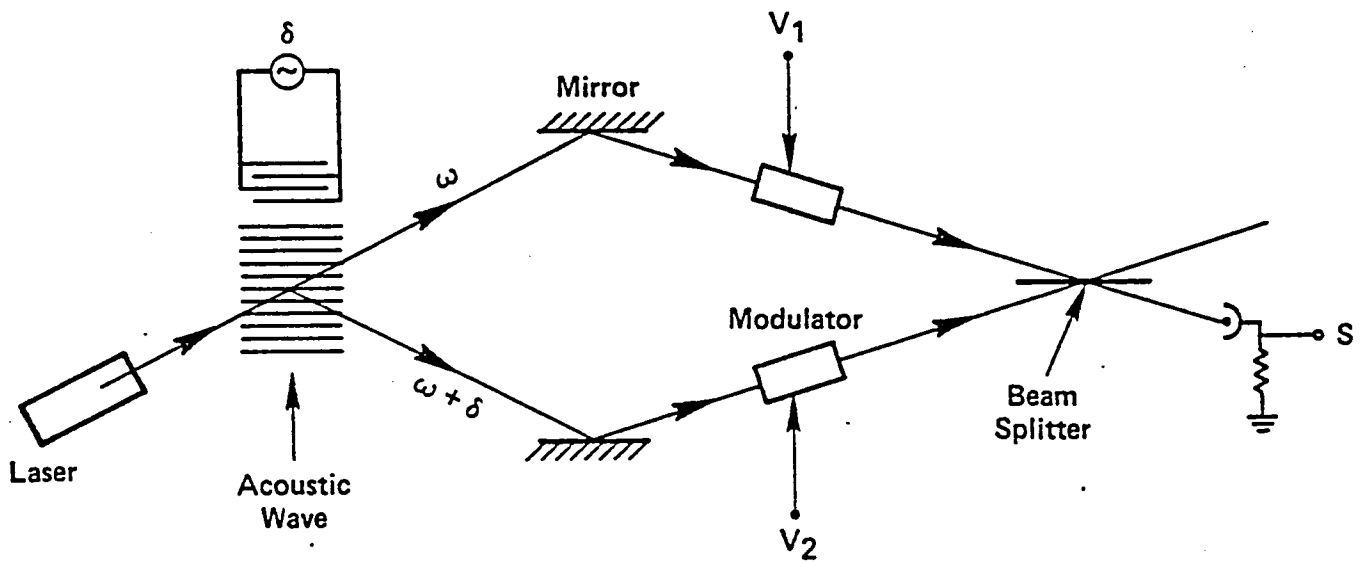


Figure 2A. Schematic of optical device for generating a signal proportional to the product $V_1 V_2$.

D/A Conversion

An optimum method for overcoming the nonlinearity problem when input data are available as parallel binary words is to use an appropriate D/A converter. We present here the first experimental results of such a device, an (electrical)digital-to-(optical) analog converter,* and show how it can be used in an integrated-optic multiplier.

The D/A converter is fabricated upon a planar, single-mode Ti-indiffused LiNbO₃ waveguide. The active element is an electrooptic integrated optic spatial light modulator (IOSLM) which is simply an extended interdigital electrode structure composed of a number of separately addressable segments. The electrode segments are addressed in parallel with the voltages representing the digital word to be converted.

In the configuration tested, it is essential that a digital "zero" be represented by a zero voltage and that all digital "ones" be represented by a voltage, V . As shown in Figure 3A, the voltages representing the digital word are applied to the electrodes through a voltage divider. The dividers are set so that the voltage V , when representing the most significant bit, results in the diffraction of an optical power which we may represent by P_{\max} . The next divider is set so that the diffracted power is $P_{\max}/2$, the next to generate $P_{\max}/4$, and so on. The total optical power diffracted by the structure is therefore the optical analog representation of the electrical digital input. This optical analog signal may then be used as the input to an analog optical device such as a multiplier, or a lens can be used to direct all of the diffracted light to a photodetector in which case the electrical analog signal is generated.

Figure 4A shows the results of a simple proof-of-principle experiment which was set up by uniformly illuminating the IOSLM with a prism-coupled guided plane wave. The diffracted light was collected by an external lens and directed onto a photodetector. The voltage dividers were individually set as described above, and the system was stepped manually through the digital words 000000 to 111111 by the use of toggle switches. The figure shows

* Developed under AFOSR support on Contract Number F49620-79-C-0044.

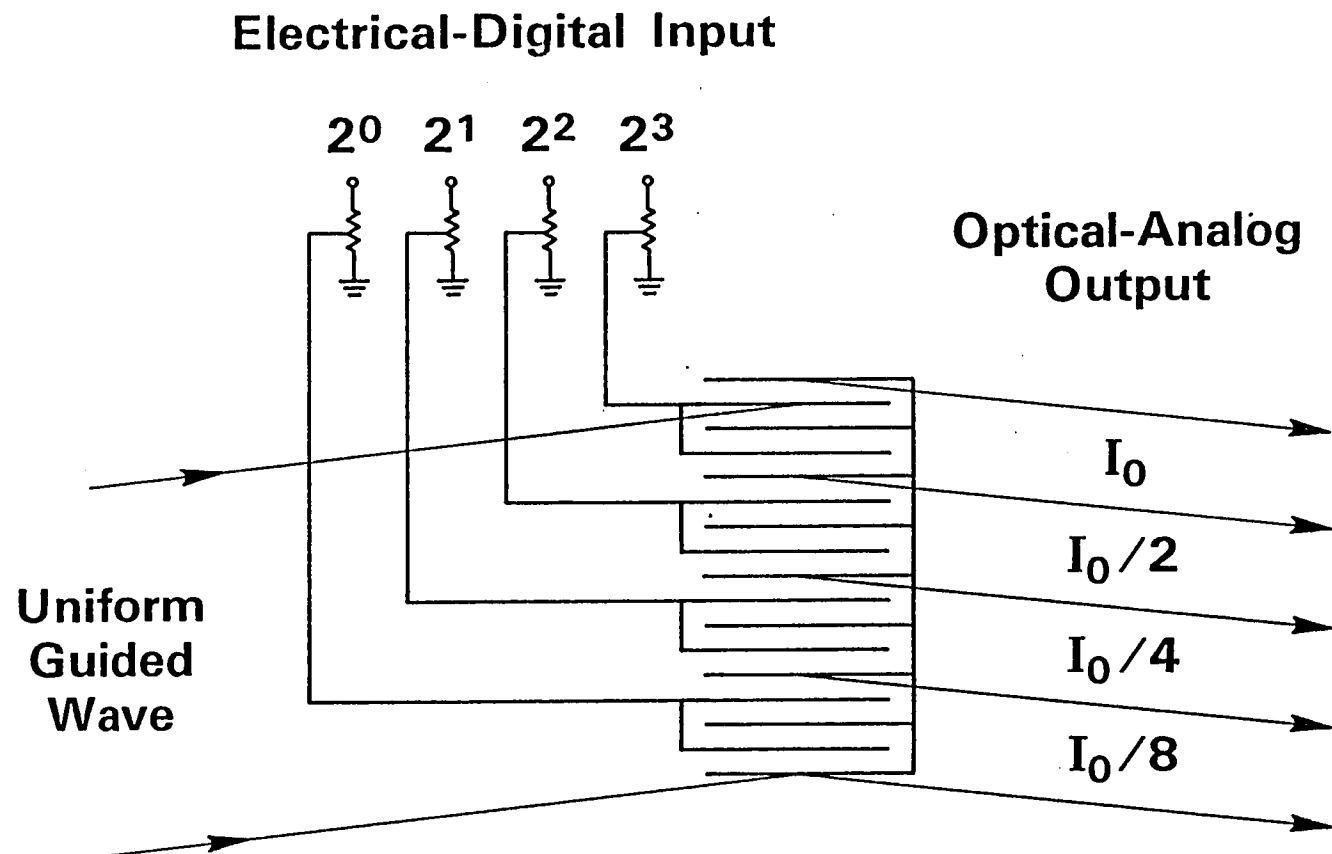


Figure 3A. The use of voltage dividers to bias the elements of an IOSLm so that the entire structure performs D/A conversion.

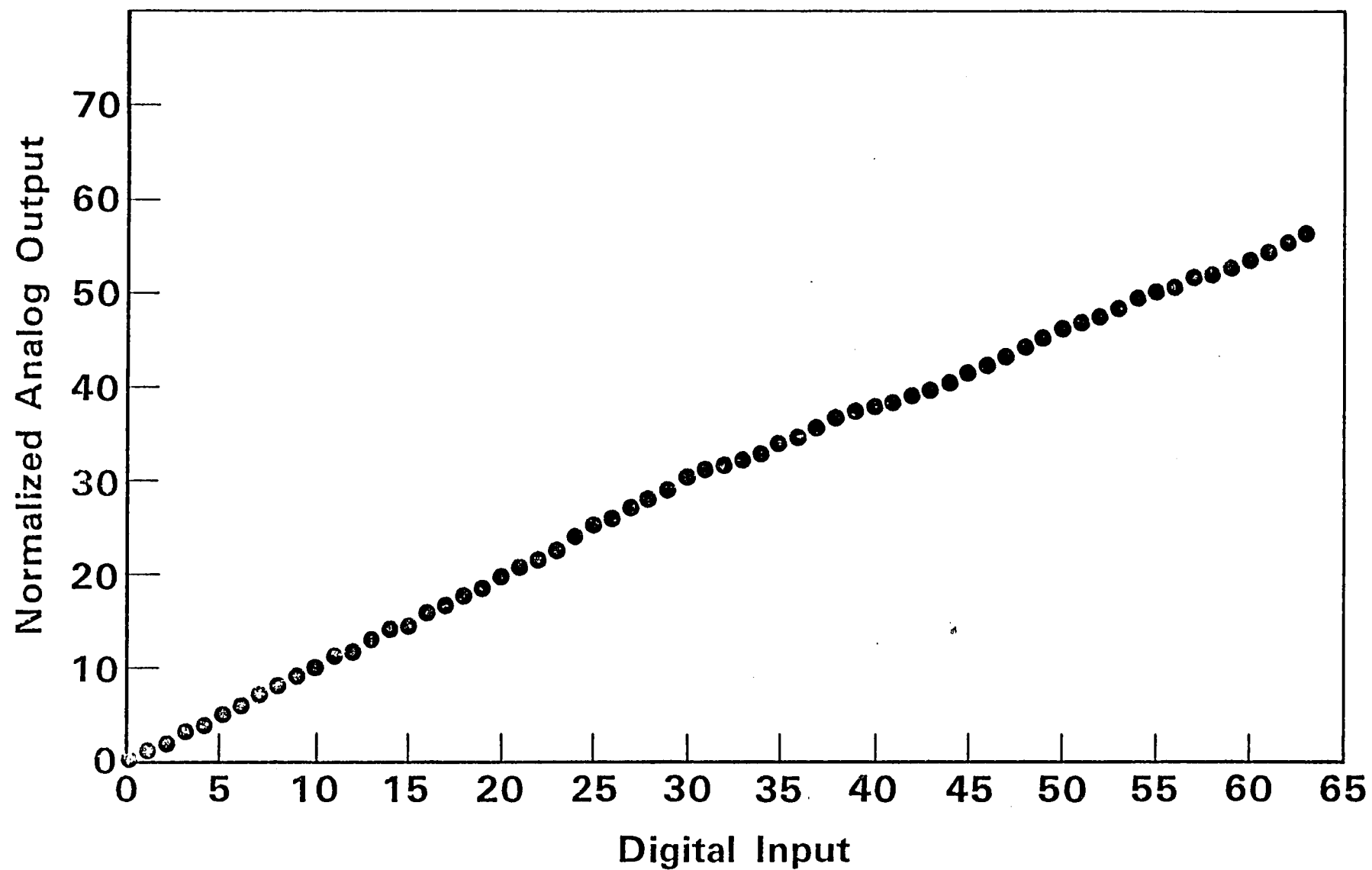


Figure 4A. Preliminary data (D.C.) from first integrated-optic D/A converter.

the analog voltage generated by the photodetector as a function of the digital input word. As can be seen, the system functioned as expected. The kink in the otherwise straight line is thought to be due to a slight missetting in one of the voltage dividers.

The high-speed performance of the integrated optic D/A can be estimated by assuming, for example, that a laser will be used which will result in a diffracted power of 50 microwatts from the most significant bit. In this case the maximum diffracted power, when all six bits are on, will be 98.44 microwatts and the contribution of the least significant bit will be 1.56 microwatts, a value which is -36 dB down from the maximum. It can be shown that, for direct detection of a 100 microwatt signal at a 100 MHz bandwidth, the signal-to-noise (SNR) of an optical detector is 60 dB. Therefore, the LSB can be detected with an excess SNR of 24 dB. This excess can be retained to achieve a minimum error rate, be used to increase the number of bits, increase the operating rate, or decrease the optical power.

Figure 5A indicates how the integrated-optic D/A can be used as part of a herringbone structure to perform part of a vector-matrix multiplication. Each matrix element is represented by a 3-bit word. Each vector element is represented by an analog signal which has been linearized by the analog method discussed above.

An IOC for matrix-vector or matrix-matrix multiplication by the engagement algorithm is shown in Figure 6A. Note that the penalty paid for using an N-bit D/A is an N-fold reduction in the dimension of the matrix which a given processor can handle.

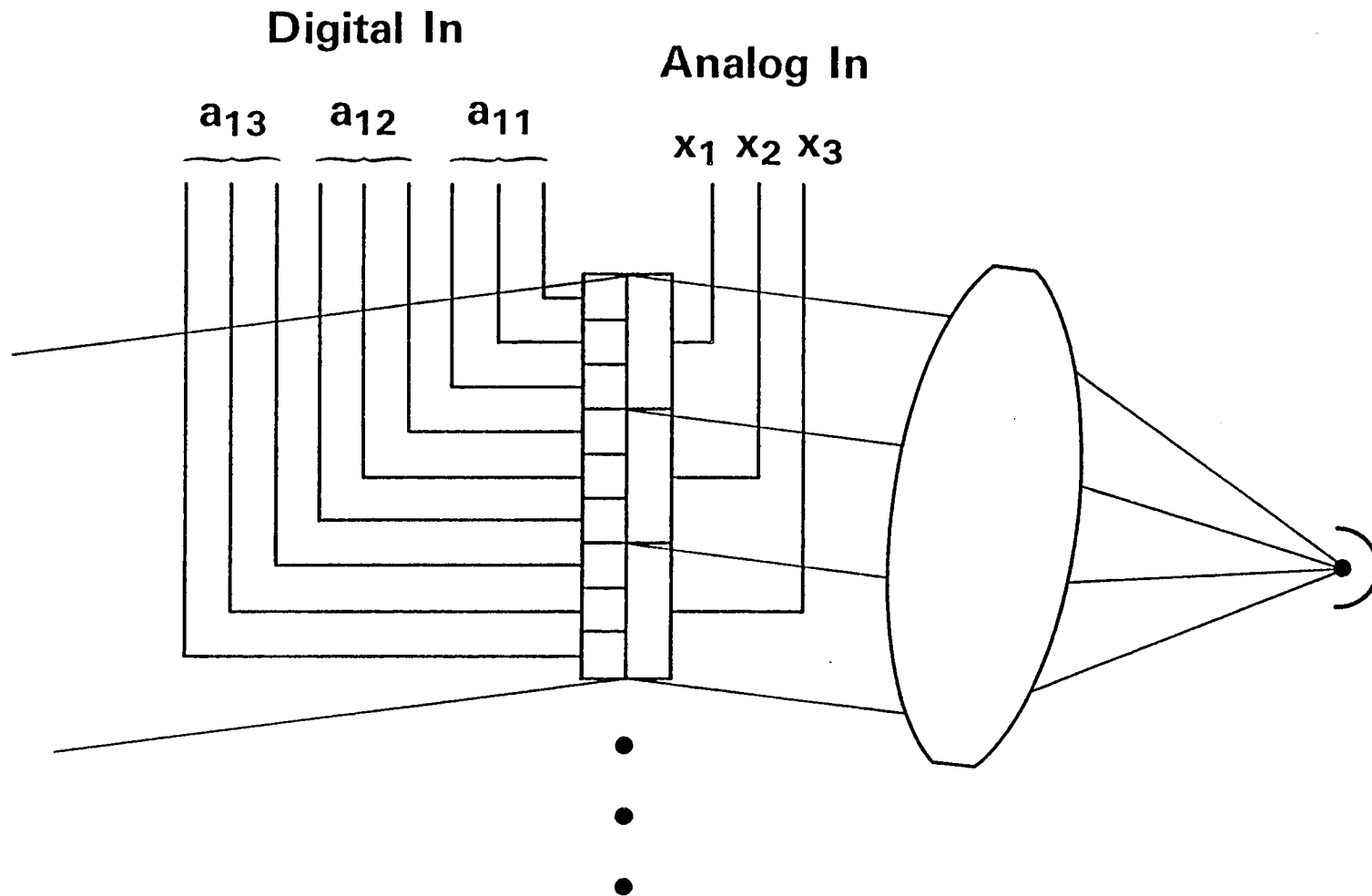


Figure 5A. A herringbone structure used to form the product of two three-vectors, one represented by three 3-bit binary words, the other by 3 analog voltages.

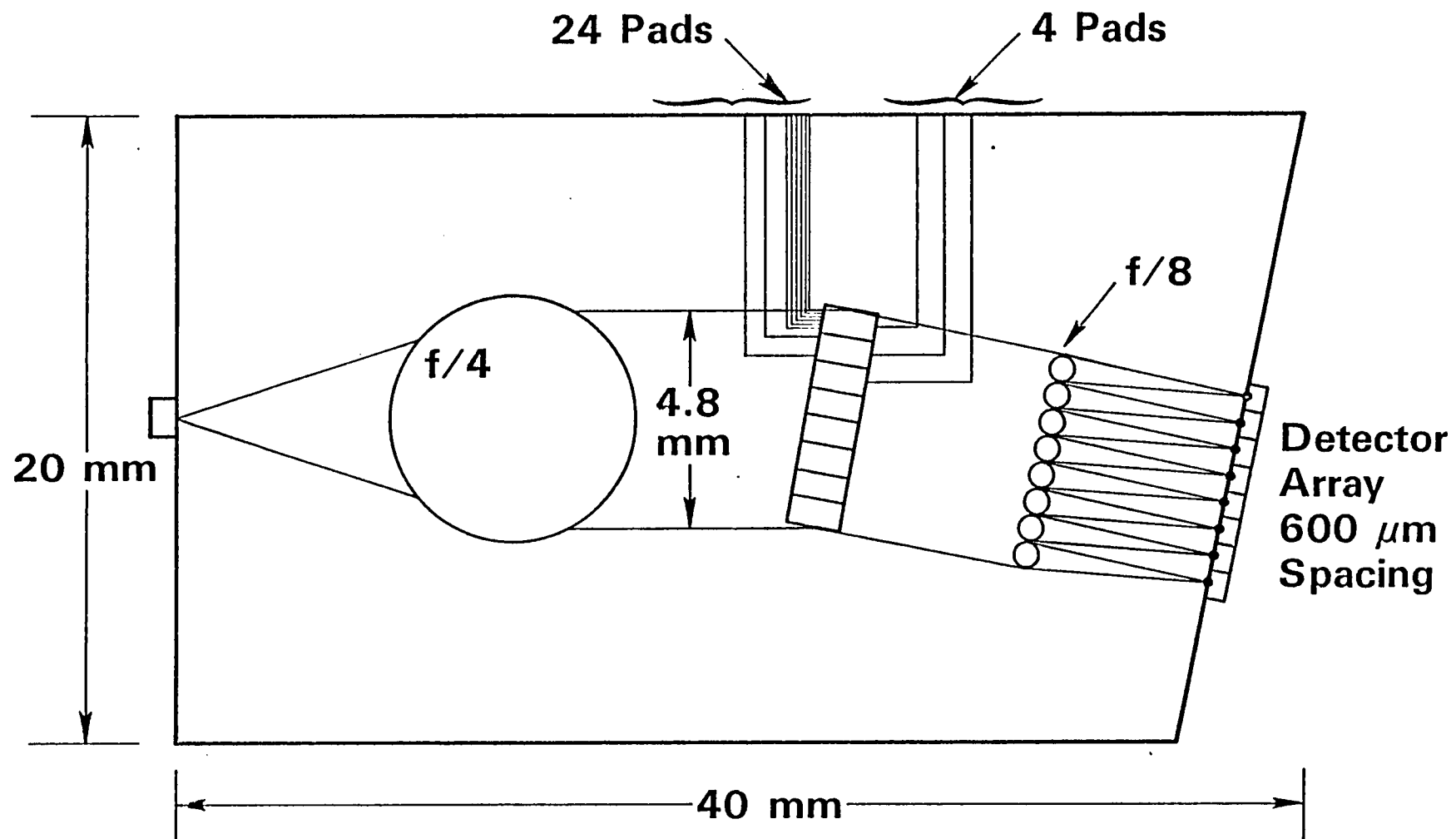
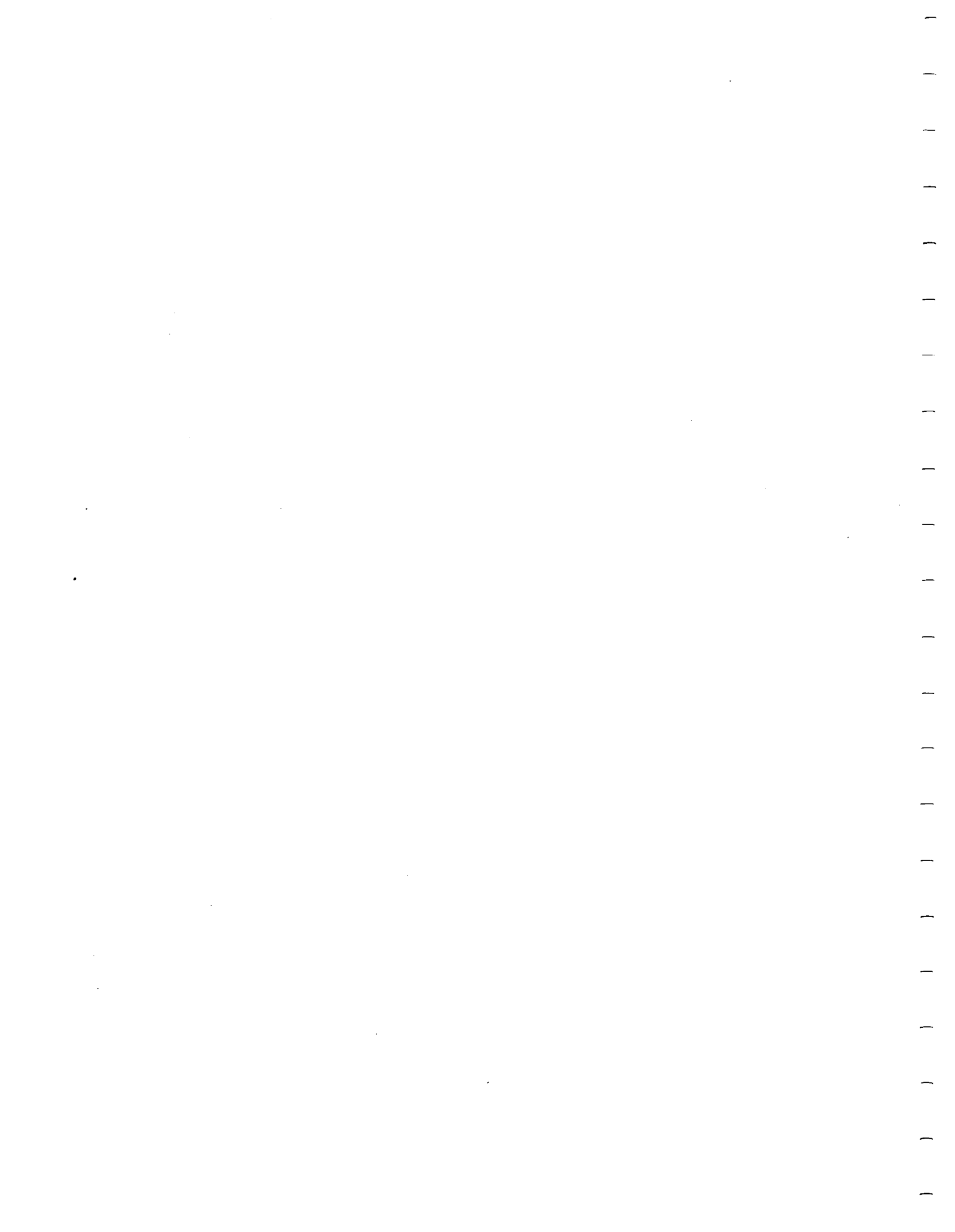


Figure 6A. IOC for vector-vector or engagement matrix-vector multiplication using the hybrid digital-analog herringbone multiplier.



APPENDIX B

SYSTOLIC TRIPLE MATRIX PRODUCT CALCULATIONS
ON PARTITIONED MATRICES

APPENDIX B

SYSTOLIC TRIPLE MATRIX PRODUCT CALCULATIONS

ON PARTITIONED MATRICES

H. J. Caulfield
Innovative Optics, Inc.
P. O. Box 1275
Concord, MA 01742

C. M. Verber
Battelle Columbus Laboratories
505 King Avenue
Columbus, OH 43201

R. L. Stermer
National Aeronautics & Space Administration
MS-470, Langley Research Center
Hampton, VA

In order to handle arbitrary sized matrices with fixed sized optical matrix processors it is necessary to expand or contract the problem to fit the processor. Here we examine this preprocessing, show a quite general method, and apply it to the type of triple matrix product calculation needed for Kalman filtering. Emphasis will be placed on systolic type processors.

The recent explosion of interest in optical matrix processors (refs. 1-6) need not be reviewed here except to note that even with spatial light modulators with one dimensional space-bandwidth products of 1000 or more, we may not be able to handle large matrices. Spatial dimensionality is used to allow representation of real or complex numbers, to achieve high numerical accuracy through binary representation, and to allow floating point calculations. As a result, we might find ourselves limited to working with relatively small matrices, say, 20 x 20. Call this processor dimension D. The problem we discuss here is how to match real problems to such a restricted processor. In all that follows we will illustrate with D=2 processors.

The first step will be to expand the given matrix so that its dimensions are mD x nD. To do this we fill out the given matrix with zeros to the right and below. For D=2 and the given matrices

$$A = \begin{bmatrix} a_{11} & a_{12} & a_{13} \\ a_{21} & a_{22} & a_{23} \\ a_{31} & a_{32} & a_{33} \end{bmatrix}$$

and

$$B = \begin{bmatrix} b_{11} & b_{12} & b_{13} \\ b_{21} & b_{22} & b_{23} \\ b_{31} & b_{32} & b_{33} \end{bmatrix},$$

we expand to

$$A_E = \begin{bmatrix} a_{11} & a_{12} & a_{13} & 0 \\ a_{21} & a_{22} & a_{23} & 0 \\ a_{31} & a_{32} & a_{33} & 0 \\ 0 & 0 & 0 & 0 \end{bmatrix} = \left[\begin{array}{c|c} A & 0 \\ \hline 0 & 0 \end{array} \right]$$

and

$$B_E = \begin{bmatrix} b_{11} & b_{12} & b_{13} & 0 \\ b_{21} & b_{22} & b_{23} & 0 \\ b_{31} & b_{32} & b_{33} & 0 \\ 0 & 0 & 0 & 0 \end{bmatrix} = \left[\begin{array}{c|c} B & 0 \\ \hline 0 & 0 \end{array} \right] .$$

It is easy to show

$$A_E B_E = \left[\begin{array}{c|c} AB & 0 \\ \hline 0 & 0 \end{array} \right] .$$

We now partition A_E and B_E into $D \times D$ submatrices. That is

$$A_E = \left[\begin{array}{c|c} A_{11} & A_{12} \\ \hline A_{21} & A_{22} \end{array} \right]$$

and

$$B_E = \left[\begin{array}{c|c} B_{11} & B_{12} \\ \hline B_{21} & B_{22} \end{array} \right] .$$

It is well known (ref. 7) that

$$A_E B_E = \begin{bmatrix} A_{11}B_{11} + A_{12}B_{21} & A_{11}B_{12} + A_{12}B_{22} \\ A_{21}B_{11} + A_{22}B_{21} & A_{21}B_{12} + A_{22}B_{22} \end{bmatrix} .$$

Let us see how we can best order these calculations. Figure 1 shows an optical matrix processor and its supporting electronics. Clearly we need never do more than a $D \times D$ matrix at any time. One memory must store A_E and B_E . The partitioning electronics then selects out of the memory the needed submatrices.

Let A_E and B_E be of dimension $nD \times nD$. If we can afford n^2 parallel $D \times D$ processors, we can use some memory-efficient approach such as the engagement approach shown in figure 2. In many cases this will be impractical. The other extreme case is that of only one $D \times D$ processor. In that case we order A_E and B_E submatrices in such a way as to calculate one submatrix at a time of the product matrix so all integration occurs on the D^2 detectors. In our example, we calculate $A_{11}B_{11}$ first and then add to it on the same detectors $A_{12}B_{21}$.

One large and important type of matrix problem is the Kalman filter: a general and powerful estimation technique widely used in many areas such as automatic control (ref. 8). The Kalman filtering process is recurring, interactive, ordered sequence of matrix inversions, additions or subtractions, and multiplications. The most difficult tasks are several triple matrix products of the form ABC . Let us now explore efficient ways of doing $A_E B_E C_E$ products.

In the case in which we can afford n^2 parallel processors, we finish calculating the 1,1 component of $A_E B_E$ just as we need it to multiply the 1,1 component of C_E in the 1,1 multiplier, etc. Thus, except for time needed for electronic conversions, reformatting, and feedback (see figure 1), the calculation of $A_E B_E C_E$ takes only $3N-1$ single $D \times D$ multiplier clock times to evaluate rather than $2(2N-1)$ if $A_E B_E$ were calculated fully before we begin to calculate $A_E B_E C_E$.

To accomplish $A_E B_E C_E$ calculation with all integration and memory taking place only at detectors we need at least $n+1$ $D \times D$ multipliers. The method is easy to understand. First we calculate the 1,1 element of $A_E B_E$ on a single $D \times D$ computer. Then we broadcast it to the n computers which, in parallel, multiply it by the (1,1), (1,2), ..., (1, N) elements of C_E . Then we calculate the 1,2 element of $A_E B_E$, multiply it in parallel with the (2,1), (2,2), ..., (2, N) elements of C_E , accumulate the sums on the detectors, etc. Because the calculations are likely to be systolic or engagement types, we can (as before) keep all parts of the system busy at all times. That is, the 1,1 component of the 1,2 component of $A_E B_E$ will be available only one clock time after the D, D component of the 1,1 component of $A_E B_E$. Of course the n parallel processors are ready for each element from the single processor as it is calculated. To calculate all n^2 components of $A_E B_E$ takes $n^2 + n-1$ clock times. Only n clock times later the whole matrix $A_E B_E C_E$ is calculated, so a total of $n^2 + 2n-1$ clock cycles is needed.

These considerations show that an expanding-partitioning-interleaving approach provides an efficient way to use $D \times D$ matrix multipliers to handle arbitrary sized matrices. The illustration of the triple matrix products so critical to Kalman filtering show in some detail how the calculations can be done while using only the $D \times D$ detector arrays for scratch pad operations (storage of intermediate results).

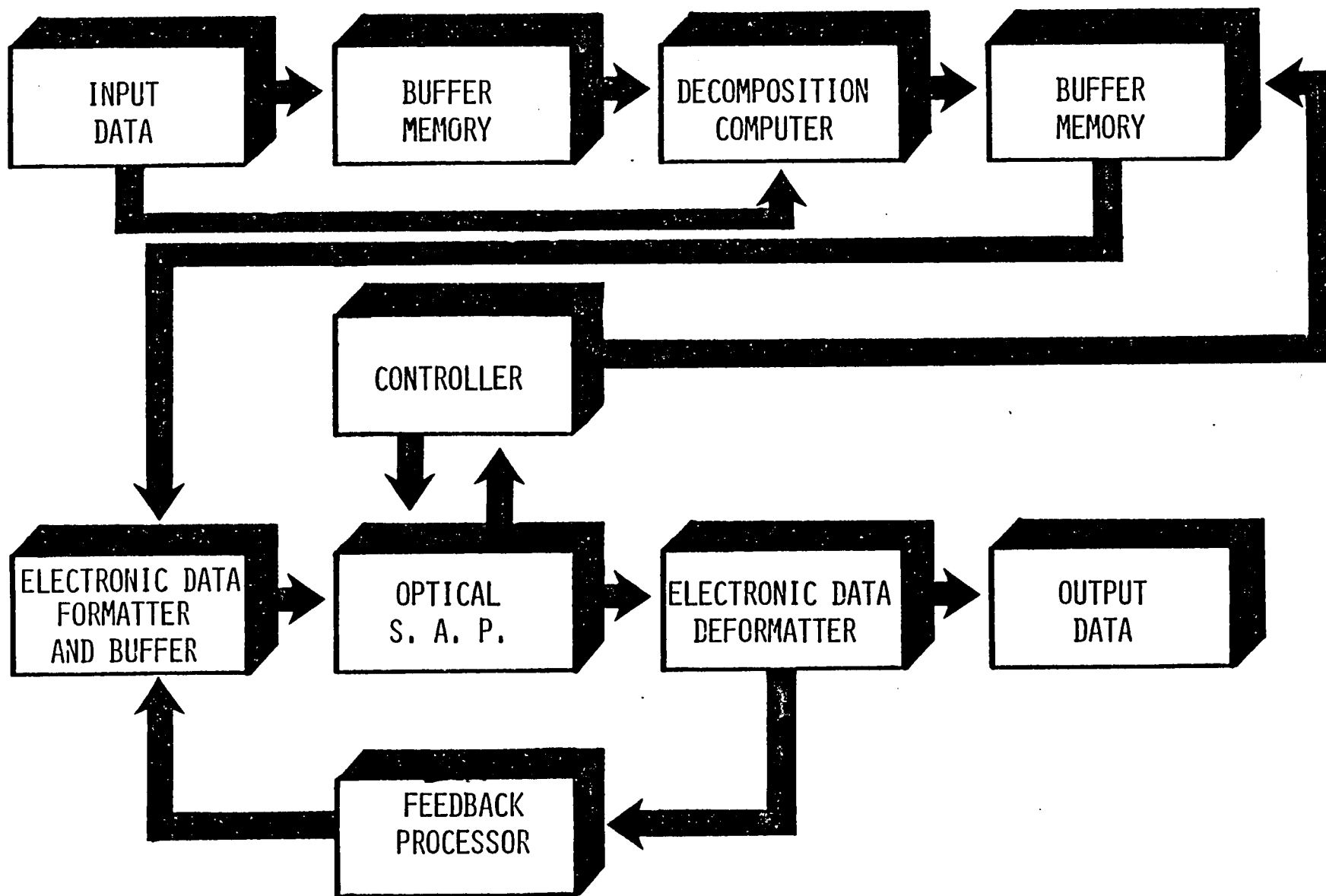
REFERENCES

1. Goodman, J. W.; Dias, A. R.; and Woody, L. M.: Opt. Lett. 2, 1 (1978).
2. Caulfield, H. J.; Dvorn, D.; Goodman, J. W.; and Rhodes, W. T.: Appl. Opt. 20, 2263 (1981).
3. Casasent, D; Appl. Opt. 21, 1859 (1982).
4. Casasent D.; Jackson, J.; and Neuman, C.: Appl. Opt. 22, 115 (1983).
5. Bocker, R. P.; Caulfield, H. J.; and Bromley, K.: Appl. Opt. 21, 2089 (1982).

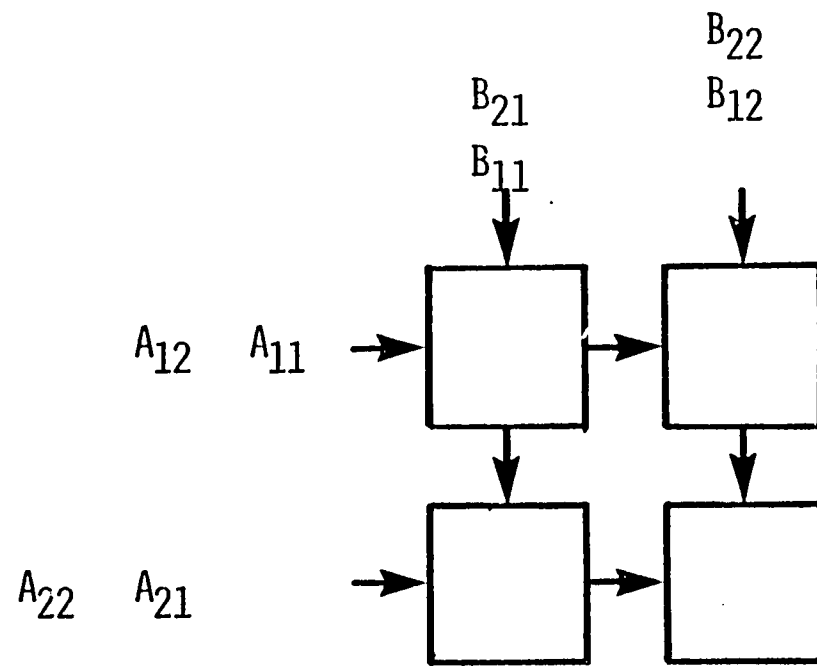
6. Athale, R. A. and Collins, W. C.: Appl. Opt. 21, 2089 (1982).
7. Most elementary matrix books discuss this, e.g., Lancaster, P.: Theory Of Matrices (Academic Press, NY, 1969) p. 16 ff.
8. Kalman, R. E. and Bucy, R. S.: J. Basic Eng. ASME Trans. 83D, 95 (1961).

Figure Captions

- Figure 1. An optical computer will contain more electronics than optics. This figure indicates perfectly some of the functions the electronics must service.
- Figure 2. Submatrices can be ordered in the same way as individual components for engagement processing (a). The notation above for the particular case illustrated in the text can be further broken down in terms of individual matrix components (b).



OVERALL SYSTEM



(A)

$$\begin{array}{c}
 A_{12} \quad A_{11} = \begin{array}{|c|c|c|} \hline 0 & A_{13} & A_{12} & A_{11} \\ \hline 0 & A_{23} & A_{22} & A_{21} \\ \hline A_{12} & A_{11} & & 0 \end{array}
 \end{array}$$

(B)

APPENDIX C

NUMERICAL ACCURACY

APPENDIX C

NUMERICAL ACCURACY

While optics will offer advantages over electronics in speed, size, power consumption, and problem size, it is known to suffer badly in accuracy comparisons. Two approaches are possible (so far as we know) to improve this situation. Both involve trading off some known advantage to gain back some accuracy.

The first approach is to do "bit slicing". That is, each number will be represented by many optical signals rather than just one. If we use 16 binary signals per number we can represent 16 bit numbers. Two independent researchers have come up with proprietary solutions to multiplying such numbers using optics with no better than 4 bit accuracy (good optical systems have 6 or 7 bit accuracy). We can not disclose those schemes now, but we will be able to before the contract is over. This scheme buys accuracy by lowered speed (if the bit slices occur sequentially) or increased complexity (if the bit slices occur in parallel). These prices are unfortunate but appear to be affordable because of the extremely large inherent speed and complexity advantages of optics over electronics when no bit slicing is used. The price is also comforting in the sense that we would be worried if nature appeared to give us something for nothing. Thus we must figure out the minimum required accuracy and design for that to achieve maximum speed or minimum complexity.

The second approach is to formulate the problem in such a way we can achieve a decreased need for accuracy if we make more calculations. We perform what we will call "approximation" and "reformulation" in sequence

many times. Suppose we want to find the x_0 satisfying $f(x_0) = 0$ and close to $x = 3$. We evaluate $f(3)$ and $f'(3)$. We then find Δx_1 such that

$$f(3) + f'(3) \Delta x_1 = 0.$$

We do not need to do this very accurately. This allows the first approximation

$$x_0^{(1)} \approx 3 + \Delta x_1.$$

We now reformulate by going back to the mathematically exact expression for $f(x)$ to find $f(x_0^{(1)})$ and $f'(x_0^{(1)})$. We can then approximate again.

Arbitrary accuracy in the final x_0 is possible if the approximation accuracy is good enough to get closer each time. This approach (the example is called the Newton-Raphson method) "starts over" with each cycle but starts closer to the correct answer each time. In a control problem we can

- use optics to calculate the control vector \vec{u} ,
- use the approximate \vec{u} to "correct" the system,
- measure and infer the resulting state vector \vec{x} , and
- use optics to calculate the control vector to correct the system given the new state vector.

From these discussions it becomes clear that a complex analysis must be undertaken to optimize the algorithm-hardware combination for any particular task. What NASA will require is the full set of algorithm and hardware variations along with the rules for making the tradeoff.

A DIFFERENT POLYNOMIAL EVALUATOR

If the purpose of the polynomial evaluator is to represent an ideal plant in an active control system (rather than solving a polynomial), it may be easier and numerically better to use a method other than Horner's rule.

In general the best fit to a function $f(x)$ using polynomials of given order is of the form

$$\tilde{f}_{m,n}(x) = \frac{a_m x^m + a_{m-1} x^{m-1} + \dots + a_0}{b_n x^n + b_{n-1} x^{n-1} + \dots + b_0}$$

A general approach to finding the a 's and b 's is Padé approximation⁽¹⁾.

Usually $m = n \pm 1$. In this case we will simply want to evaluate $f(x) \approx \tilde{f}_{mn}(x)$

given x very rapidly. We have no interest in finding its roots.

Likewise we may wish to integrate a differential equation of the form

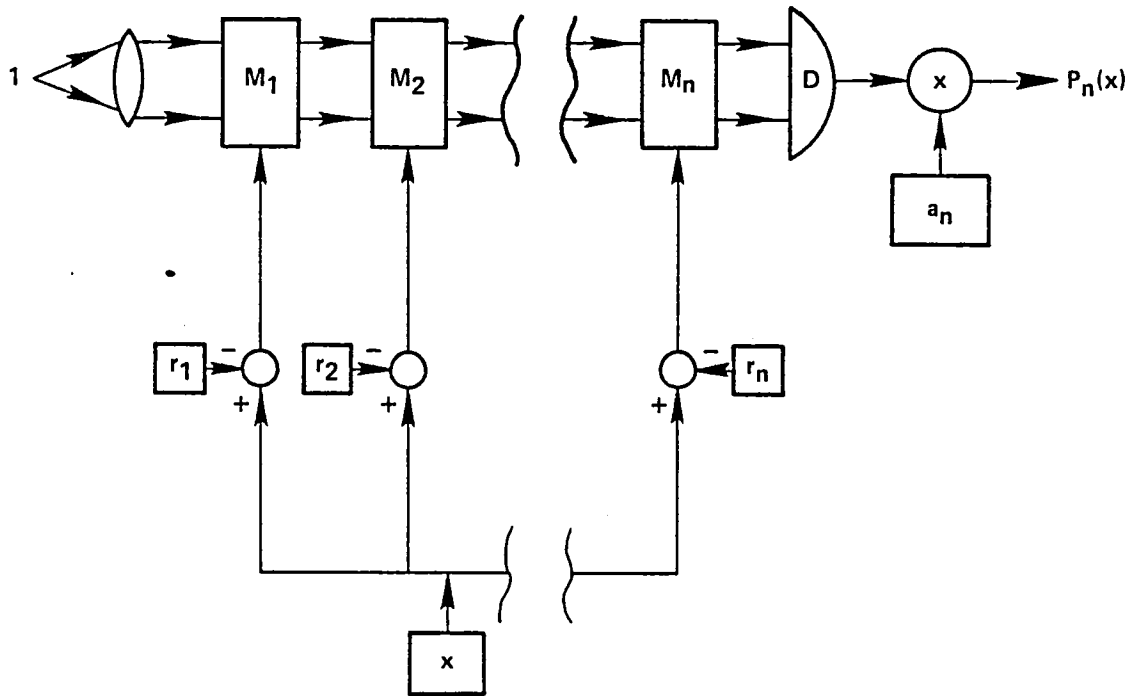
$$dy/dx = f(x,y) \approx \tilde{f}_{mn}(x,y).$$

Here we can use a high order Runge-Kutta method⁽¹⁾ which requires evaluating $f(x,y)$ at a variety of specific arguments.

In these cases a product form of the polynomial provides better numerical stability⁽²⁾. Let us write

$$P_n(x) = a_n \prod_{i=1}^n (x-r_n),$$

where the r_n 's are the roots of $P_n(x)$ which can be preevaluated. The optical product evaluator is very simple. Conceptually, it looks like this.



A series of modulators M_1, \dots, M_n is driven by signals $(x-r_1), \dots, (x-r_n)$ and the product is detected at D . Time delays between x inputs to the stages will be unnecessary for any NASA applications.

REFERENCES

1. For example, see A. Ralston, A First Course In Numerical Analysis, (McGraw-Hill, New York, 1965).
2. J. F. Hart, Computer Approximations (John Wiley, New York, 1968).

APPENDIX D

PUBLICATIONS

APPENDIX D

PUBLICATIONS

1. James R. Busch, Van E. Wood, Richard P. Kenan, and Carl M. Verber, "Evaporated As_2S_3 Luneburg Lenses for $\text{LiNbO}_3\text{:Ti}$ Optical Waveguides," Optical Information Processing for Aerospace Applications, NASA Conference Publication 2207 (NASA Scientific and Technical Information Branch, 1981), pp. 251-261.
2. Carl M. Verber, James R. Busch, and Van E. Wood, "As $_2$ S $_3$ Luneburg Lenses on LiNbO $_3$ Waveguides," J. Opt. Soc. Amer. 71, 1559 (1981) (abstract).
3. James R. Busch, Van E. Wood, Duncan T. Moore, C. Benjamin Wooley, and W. H. Southwell, "Rectangular Luneburg-type Lenses for Integrated Optics", Opt. Lett. 8 (4), 226-228 (1983).
4. C. M. Verber, and R. P. Kenan, "Integrated Optical Approaches to Matrix Multiplication", Presented at the Optical Information Processing Conference II, August 30-31, 1983, Hampton, Virginia, (NASA CP to be published.)
5. H. J. Caulfield, C. M. Verber and R. L. Stermer, "Solving Large Matrix Problems With Intermediate Sized Optical Processors", Presented at the Optical Information Processing Conference II, August 30-31, 1983, Hampton, Virginia, (NASA CP to be published.)
6. Carl M. Verber, "Integrated Optical Architectures and Implementations", Presented at SPIE LA'84 Meeting, January 1984, Los Angeles, CA.

1. Report No. NASA-CR-172276		2. Government Accession No.		3. Recipient's Catalog No.	
4. Title and Subtitle Luneburg Lens and Optical Matrix Algebra Research				5. Report Date February 10, 1984	
				6. Performing Organization Code	
7. Author(s) V. E. Wood, J. R. Busch, C. M. Verber and H. J. Caulfield*				8. Performing Organization Report No.	
9. Performing Organization Name and Address Battelle Columbus Laboratories 505 King Avenue Columbus, Ohio 43201 *Innovative Optics Inc.				10. Work Unit No.	
				11. Contract or Grant No. NAS1-16652	
12. Sponsoring Agency Name and Address National Aeronautics and Space Administration Washington, DC 20546				13. Type of Report and Period Covered Contractor Report Final - 9/1982 - 9/1983	
				14. Sponsoring Agency Code	
15. Supplementary Notes Langley technical monitor: Robert L. Stermer Final Report					
16. Abstract We report the results of two independent research efforts which cover different aspects of integrated optics technology. The first study, which deals with Integrated Optic Circuits for Matrix Computation, stresses planar, as opposed to channelized, integrated optical circuits (IOCs) as the basis for computational devices. Both fully-parallel and systolic architectures are considered and the tradeoffs between the two device types are discussed. It is pointed out that the Kalman filter approach is a most important computational method for many NASA problems. This approach to deriving a best-fit estimate for the state vector describing a large system will lead to matrix sizes which are beyond the predicted capacities of planar IOCs. It is shown that this problem can be overcome by matrix partitioning, and several architectures for accomplishing this are described. The Luneburg lens work has involved development of lens design techniques, design of mask arrangements for producing lenses of desired shape, investigation of optical and chemical properties of arsenic trisulfide films, deposition of lenses both by thermal evaporation and by rf sputtering, optical testing of these lenses, modification of lens properties through ultraviolet irradiation, and comparison of measured lens properties with those expected from ray-trace analyses. Lenses with apertures up to 1 cm and design speeds down to f/2 at this aperture were tried. The better evaporated lenses had focal spot sizes, at reduced aperture, no more than twice the limit set by diffraction effects. Initial sputtered lenses promised to be of comparable quality; lenses made after the sputtering target had been in operation for some time, though, tended to absorb light excessively at the design wavelength, 633 nm. This effect appears to be related to a change in the composition of the films, but the reason for this change is not yet fully understood.					
17. Key Words (Suggested by Author(s)) Integrated optics Luneburg lens lithium niobate arsenic trisulfide electrooptic modulator matrix multiplication systolic array processor			18. Distribution Statement Unclassified - Unlimited Subject Category 74		
19. Security Classif. (of this report) Unclassified		20. Security Classif. (of this page) Unclassified		21. No. of Pages 107	
				22. Price	

NASA Contractor Report 172276
Distribution List
NAS1-16652

NASA Langley Research Center
Attn: Research Information Office
Mail Stop 151A
Hampton, VA 23665 (2 copies)

NASA Langley Research Center
Attn: Technology Utilization Office
Mail Stop 139A
Hampton, VA 23665

NASA Ames Research Center
Moffett Field, CA 94035
Attn: Library, Mail Stop 202-3

Dryden Flight Research Facility
P. O. Box 273
Edwards, CA 93523

NASA Goddard Space Flight Center
Greenbelt, MD 20771
Attn: Library

NASA Lyndon B. Johnson Space Center
2101 Webster Seabrook Road
Houston, TX 77058
Attn: JM6/Library

NASA Marshall Space Flight Center
Marshall Space Flight Center, AL 35812
Attn: Library, Mail Stop AS24L

Jet Propulsion Laboratory
4800 Oak Grove Drive
Pasadena, CA 91103
Attn: 111-113/Library

NASA Lewis Research Center
21000 Brookpark Road
Cleveland, OH 44135
Attn: Library, Mail Stop 60-3

NASA John F. Kennedy Space Center
Kennedy Space Center, FL 32899
Attn: Library, NWSI-D

National Aeronautics and
Space Administration
Attn: RT
Washington, DC 20546

Chen S. Tsai
University of California,
Irvine
Dept. of Elec. Engr.
Irvine, CA 92717

Anthony VanderLugt
Harris Corp.
P.O. Box 37
Melbourne, FL 32902

Gilbert H. Walker
NASA Langley Research Center
M.S. 160
Hampton, VA 23665

Cardinal Warde
MIT
Room 13-3134
Cambridge, MA 02139

Martin F. Wehling
UKSAF
AFATL/DLMI
Eglin AFB, FL 32542

George P. West
Th Holotronics Corp.
424 N. Main Street
Findlay, OH 45840

Francis T. S. Yu
Penn State University
Electrical Engineering Dept.
University Park, PA 16802

John M. Zavada
U.S. Army Research Office
P.O. Box 12211
Research Triangle Park, NC 27713

Gregory Adamovsky
John Carroll University
Physics Department
Cleveland, OH 44118

Byong H. Ahn
USA NV & EOL
Night Vision & Electro-Optics Lab.
Laser Div., Bldg. 357
Ft. Belvoir, VA 22060

Edmund Altonji
ITT Corporation
390 Washington Avenue
Nutley, NJ 07110

David Armitage
Lockheed Research Lab.
3251 Hanover Street
Dept. 52-54, Bldg. 202
Palo Alto, CA 24306

R. A. Athale
NRL
Code 6530
Washington, DC 20375

Robert Baumbick
NASA Lewis Research Center
MS 100-1
21000 Brookpark Road
Cleveland, OH 44135

Harry Benz
NASA Langley Research Center
MS 473
Hampton, VA 23665

Norman J. Berg
Harry Diamond Labs.
2800 Powder Mill Road
Adelphi, MD 20783

Tom Bicknell
JPL
4800 Oak Grove Dr.
Pasadena, CA 91103

Jean Breedlove
The Aerospace Corp.
P.O. Box 92957, M4-934
Los Angeles, CA 90009

Alfred J. Burford
USA/FSTC
220 7th St. N.E.
Charlottesville, VA 22901

Lt. Col. Robert W. Carter, Jr.
AFOSR
AFOSR/NE
Bolling AFB, DC 20332

Steven Cartwright
Univ. of Dayton Research Inst.
300 College Park
Dayton, OH 45469

H. J. Caulfield
Innovative Optics, Inc.
P.O. Box 1275
Concord, MA 01342

Gordon Chin
NASA Goddard Space Flight Cent.
Code 693.0
Greenbelt, MD 20771

Robert C. Clausen
Honeywell
Corporate Technology Center
10701 Lyndale Ave., So.
Bloomington, MN 55337

Stuart A. Collins, Jr.
Ohio State University
ElectroScience Lab.
1320 Kinnear Rd.
Columbus, OH 43212

Uzi Efron
Hughes
3011 Malibu Canyon Rd.
Malibu, CA 90265

Sverre T. Eng
Jet Propulsion Lab.
4800 Oak Grove Dr.
M.S. 198-226
Pasadena, CA 91109

Harry Erwin
NASA Johnson Space Center
308 Oak
Friendswood, TX 77546

Joseph W. Fikes
International Laser Systems
3404 N. Orange Blossom Trail
Orlando, FL 32804

Arthur Fisher
NRL
Code 6537, NRL
Washington, DC 20375

David Flannery
USAF - Avionics Lab.
AFWAL/AADO-2
Wright Patterson AFB, OH 45433

Charles Garvin
Harry Diamond Labs.
2800 Powder Mill Road
Adelphi, MD 20783

John Goebel
NASA Ames Research Center
MS 244-7
Moffett Field, CA 94035

Darrel Hopper
FTD/TQTA
Wright Patterson AFB, OH 45433

Lynn Hutcheson
Honeywell
10701 Lyndale Ave., S.
Bloomington, MN 55343

Scott Israel
Lockheed Electronics
1501 U.S. Highway 22
Plainfield, NJ 07061

Alan R. Johnston
Jet Propulsion Lab.
4800 Oak Grove Drive
Mail Stop 198/231
Pasadena, CA 91109

David R. Johnson
NASA Langley Research Center
MS 235
Hampton, VA 23665

Steve Katzberg
NASA Langley Research Center
MS 473
Hampton, VA 23665

Ronald L. Kirk
The Holotronics Corp.
424 North Main Street
Findlay, OH 45840

Sing H. Lee
University of California at
San Diego
Elect. Engr. & Computer Sci. Dept.
La Jolla, CA 92093

John A. Neff
DARPA/DSO
1400 Wilson Blvd.
Arlington, VA 22209

Charles P. Neuman
Dept. of Electrical & Computer
Engineering
Carnegie-Mellon University
Pittsburgh, PA 15213

Melvin Pedinoff
Hughes Research Labs.
3011 Malibu Canyon Rd.
Malibu, CA 90265

John M. Pellegrino
Harry Diamond Labs.
2800 Powder Mill Road
Adelphi, MD 20783

Benjamin J. Pernick
Grumman Aerospace
M.S. A-08/35
Bethpage, NY 11714

Michael C. Reichenback
Lockheed Elec. Co.
1501 U.S. Highway 22
Plainfield, NJ 07061

Thomas C. Robbins
Dept. of Defense
9800 Savage Rd.
Attn: R533
Ft. Meade, MD 20755

Jeffrey B. Sampsell
Texas Instruments
13500 N. Central Exp.
M/S 105
Dallas, TX 75265

Richard Samms
Information & Control
Systems, Inc.
28 Research Drive
Hampton, VA 23666

Jag J. Singh
NASA Langley Research Center
MS 235
Hampton, VA 23665

Eugene Skurnick
ITT - Avionics
390 Washington Ave.
Nutley, NJ 07110

Martin Sokoloski
NASA Headquarters
RTC-6
Washington, DC 20546

Robert L. Stermer (20 copies)
NASA Langley Research Center
MS 470
Hampton, VA 23665

Poohsan N. Tamura
Honeywell CTC
10701 Lyndale Ave., South
Bloomington, MN 55420

Thomas H. Thornton
Jet Propulsion Labs.
M.S. 198-226
4800 Oak Grove Drive
Pasadena, CA 91109

NASA Scientific and Technical
Information Facility
6571 Elkridge Landing Road
Linthicum Heights, MD 21090
(original + 13)



3 1176 00518 4503

DO NOT REMOVE SLIP FROM MATERIAL

Delete your name from this slip when returning material to the library.

NAME	DATE	MS
TOM BOOTE LAFB	DEC 17 1957	LAFB